8-2008

Development of a Real-time Ultra-wideband See Through Wall Imaging Radar System

Yunqiang Yang
University of Tennessee - Knoxville

To the Graduate Council:

I am submitting herewith a dissertation written by Yunqiang Yang entitled "Development of a Real-time Ultra-wideband See Through Wall Imaging Radar System." I have examined the final electronic copy of this dissertation for form and content and recommend that it be accepted in partial fulfillment of the requirements for the degree of Doctor of Philosophy, with a major in Electrical Engineering.

Aly E. Fathy, Major Professor

We have read this dissertation and recommend its acceptance:

Marshall O. Pace, Paul B. Crilly, Mohamed R. Mafouz, Thomas T. Meek, Samir El-Ghazaly

Accepted for the Council:
Dixie L. Thompson

Vice Provost and Dean of the Graduate School

(Original signatures are on file with official student records.)

To the Graduate Council:

I am submitting herewith a dissertation written by Yunqiang Yang entitled "Development of a Real-time Ultra-wideband See Through Wall Imaging Radar System." I have examined the final electronic copy of this dissertation for form and content and recommend that it be accepted in partial fulfillment of the requirements for the degree of Doctor of Philosophy, with a major in Electrical Engineering

Aly E. Fathy, Major Professor

We have read this dissertation
and recommend its acceptance:

Marshall O. Pace

Paul B. Crilly

Mohamed R. Mafouz

Thomas T. Meek

Samir El-Ghazaly

Accepted for the Council:

Carolyn R. Hodges
Vice Provost and Dean of the Graduate School

(Original signatures are on file with official student records.)

Development of a Real-time Ultra-wideband See Through Wall Imaging Radar System

A Dissertation Presented for
The Doctor of Philosophy
Degree
The University of Tennessee, Knoxville

Yunqiang Yang
August 2008

ACKNOWLEDGEMENTS

Many persons have supported and encouraged me throughout these years. I feel these persons should be acknowledged first and foremost because without them, I would not be writing this dissertation and I would not be where I stand.

Thanks to my parents for their constant love and support, and for their always standing by me. Their living faith has provided me with a strong foundation to build my own life.

I owe much to Dr. Aly Fathy, my advisor. I thank him for all his spirited guidance, encouragement, and his unique capability to enthuse students. He is an excellent scientist as well as a life mentor. I have learned a tremendous amount from him, which has well prepared me for the future. No wards can possibly express my deepest gratitude to him.

I would like to thank Dr. J. Reece Roth, who actually brought me into this university and this department as a M.S. student and his research assistant. A scientist and educator with great personality, he helped to shape my view of the world in many positive ways.

I appreciate Dr. Marshall O. Pace, Dr. Samir El-Ghazaly, Dr. Mohamed Mafouz, Dr. Thomas T. Meek, and Dr. Paul B. Crilly for serving on my committee and reviewing my work. Thanks to all the EECS department staff for helping me whenever I needed it.

The sophisticated work would not be done without the support of the team. I need to thank Jianye Wang (visiting scholar) and Shaoyu Liu (Ph.D. student) for their tremendous contribution on FPGA digital design. I need to thank Cemin Zhang and Song Lin (Ph.D. students) for their contribution on microwave circuit design. Many thanks go to other team members, a long list of names not shown here, for sharing their expertise with me and helping me carry out various projects through years.

The completion of my work would not be possible without solid financial support. I would like to thank Dr. Mongi A. Abidi (the Department of EECS), and Dr. Mohamed Mafouz (the Department of Mechanical, Aerospace and Biomedical Engineering) for funding my work. I also need to thank Dr. Yoon Kang (Oak Ridge National laboratory) for his sponsorship.

Last, not the least, I must thank my many friends, here at UTK and elsewhere, for the many good times together with them and for helping me keep perspective during my stressful times.

ABSTRACT

Ultra-Wideband (UWB) See-Through-Wall (STW) technology has emerged as a must-have enabling technology by both the military and commercial sectors. As a pioneer in this area, we have led the research in addressing many of the fundamental STW questions. This dissertation is to investigate and resolve a few hurdles in advancing this technology, and produce a realizable high performance STW platform system, which will aid the STW community to find the ultimate answer through experimental and theoretical work. The architectures of a realizable STW imaging system are thoroughly examined and studied. We present both a conceptual system based on RF instruments and a standalone real-time system based on custom design, which utilize reconfigurable design architecture and allows scaling down/up to a desired UWB operating frequency with little difficulty. The systems will serve as a high performance platform for STW study and other related UWB applications. Along the way to a complete STW system, we have developed a simplified transmission line model for wall characteristic prediction; we have developed a scalable synthetic aperture array including both the RF part and the switch control/synchronization part; we have proposed a cost-effective and efficient UWB data acquisition method for real-time STW application based on equivalent-time sampling method. The measurement results reported here include static image formation and tracking moveable targets behind the wall. Even though digital signal processing to generate radar images is not the focus of this research, simple methods for image formation have been implemented and results are very encouraging.

TABLE OF CONTENTS

Chapter Page

LIST OF TABLES

Table Page

LIST OF FIGURES

Figure Page

Chapter 1 . INTRODUCTION AND MOTIVATION

1.1 Background

The term Ultra-Wideband (UWB) has been introduced by the Defense Advanced Research Projects Agency (DARPA) in a radar study undertaken in 1990. UWB technology was also referred by: impulse, carrier-free, and baseband technology. UWB serves as a convenient means to discriminate between conventional narrow band systems and those utilizing short pulse with a large fractional bandwidth. Common definition of narrowband is $(f_H - f_L)/ f_c < 1\%$, and FCC definition of UWB is $(f_H - f_L)/ f_c > 25\%$ or Total Bandwidth >500MHz, (see Figure 1.1). The basic concept of UWB involves the radiation, reception and processing of very wide bandwidth radio emissions. UWB technology can be traced back to the study of electromagnetic propagation in the time domain in 1960s. Dr. Gerald F. Ross first demonstrated the feasibility of utilizing UWB waveforms for radar and communications applications in the late 1960's and early 1970's. The detailed overview of the history of UWB and its early development can be found in [1]-[5].

Previously much of the UWB work was performed under classified U.S. Government programs and focused on military applications. However, the development of UWB technology has been greatly accelerated since the release of a FCC Notice of Inquiry in 1998 and a subsequent Report and Order in February 2002 [6][7], which permits the unlicensed UWB operation of imaging, vehicular radar and communications systems [8][9]. Table 1 summarizes the FCC emission limits for various UWB systems.

The UWB technology has its unique properties due to its short pulse duration and wide bandwidth. For radar applications, the UWB pulses can provide very fine range resolution and precise positioning capabilities. The low spectral density of UWB signal results in the low probability of detection and minimal RF health hazard. For communications, UWB offers increased immunity to multipath effects as it can be processed in the time-domain. Further advantages of UWB technology include the relatively low system complexity and low cost. UWB systems can be made with minimal RF or microwave components. UWB systems are also highly frequency-adaptive and can be positioned anywhere within the RF spectrum, to avoid interference to existing services and fully utilize the available spectrum.

As one of the major applications of UWB, summarized in Table 1, See-Through-Wall (STW) Imaging is invaluable to many organizations including the military, law enforcement and rescue/search departments [10]. There are different approaches that can be utilized for STW surveillance, including: Ultrasound, Thermal (IR) imaging, Magnetic detection, Millimeter wave, X-ray, and Radar (including UWB radar). Each of these approaches has its strength. Ultrasound is able to "see" through metal sheets, Magnetic can detect metal objects, and Radar provides good resolution relative to other approaches. Most approaches have also their own weakness, for example, millimeter wave and IR have inadequate wall penetration capabilities, Ultrasound only offers coarse resolution,

meanwhile traditional radars suffer from multi-path issues, and X-ray system is expensive and non-portable. Table 2 summarizes the performance of various approaches. In general, UWB radar is superior over other technologies and for its inherent fine resolution in time, good penetration into many common materials, and all-weather operational capability.

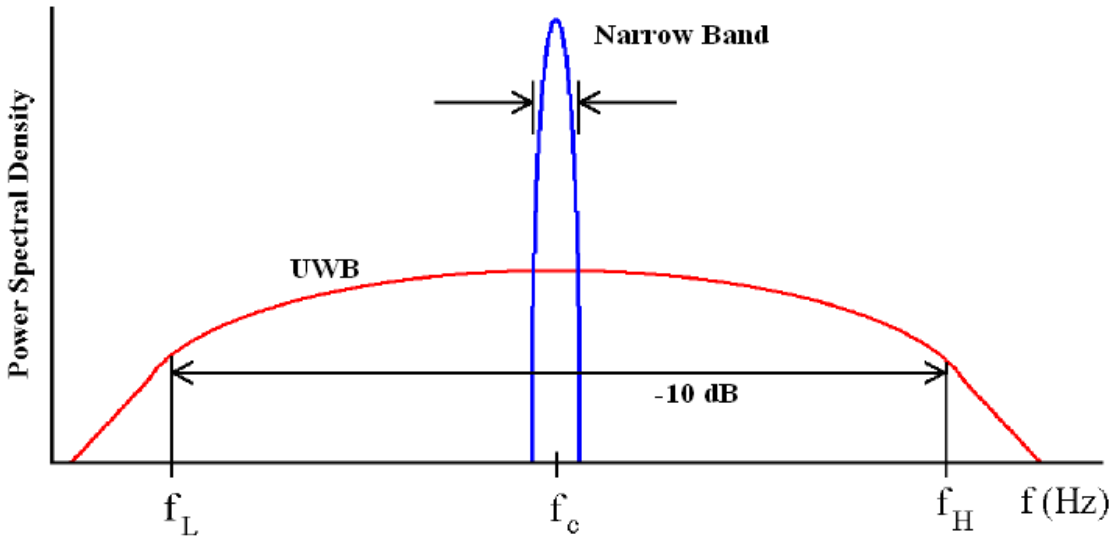

Figure 1.1: UWB and Narrow Band Spectrum.

Table 1: FCC Emission Limits (dBm/MHz).

UWB System	**GPR, and Wall Imaging**	**Through-wall Imaging, and Surveillance**	**GPR, and Medical Imaging**	**Vehicular Radar**
Assigned Frequency Band	< 960 MHz	1.99– 10.6 GHz	3.1–10.6 GHz	>24.075 GHz
≤ 960 MHz	The radiated emissions at or below 960 MHz shall not exceed the emission levels in Section 15.209 of the FCC Part 15 UWB rules.			
960- 1 610 MHz	-65.3 dBm	-53.3 dBm	-65.3 dBm	-75.3 dBm
1 610- 1 990 MHz	-53.3	-51.3	-53.3	-61.3
1 990-3 100 MHz	-51.3	-41.3	-51.3	-61.3
3.1-10.6 GHz	-51.3	-41.3	-41.3	-61.3
10.6- 22.0 GHz	-51.3	-51.3	-51.3	-61.3
22.0- 29.0 GHz	-51.3	-51.3	-51.3	-41.3
29.0- 31.0 GHz	-51.3	-51.3	-51.3	-51.3
Above 31.0 GHz	-51.3	-51.3	-51.3	-61.3

Table 2: UWB See-Through-Wall and other technologies.

Comparison	**Conventional Radar**	**Ultrasound**	**Thermal (IR)**	**X-ray**	**UWB Radar**
Resolution	Marginal	Good	Good	Good	Good
Day/Night, All Weather	Yes	Yes	No	No	Yes
Wall Penetration	Good	Marginal	Poor	Good	Good
Capability to Identify	Yes	Yes	No	No	Yes
Range (m)	10	0.1	1	1	100

1.2 2007 STW State-of-the-Art

The UWB See-Through-Wall systems were usually developed in close collaboration with the government agencies. Due to the complexities associated with the development of UWB STW systems, commercial products of such technology are still limited up to now. There are quite a few companies and research laboratories that have addressed or produced such radars which may represent the start-of-art development. These systems are (1) RadarVision from Time Domain Corporation; (2) ImpSAR from Eureka Aerospace; (3) Xaver 800 from Camero Inc; (4) Radar Scope from L3 CyTerra Corporation. These systems have been demonstrated in varying levels of success in imaging through building walls from an exterior position and detecting motion in the other side. Their utilized bandwidth extends from 500 MHz to 3.5 GHz, and the detection ranges are from 3 m to 100 m. These systems provide 1-D range profile, 2-D image, or 3-D map, as claimed. A summary of these systems will be given here for completeness. A comparison between these systems is given in Table 3.

RadarVision from Time Domain Corporation, the earliest standalone UWT STW system is RadarVision, which was announced to public in 2003 and developed by Time Domain Corporation based in Huntsville, Alabama. The RadarVision is designed to detect people through walls. The radar sends out UWB pulses, in 10MHz rate, to penetrate most common building materials including brick, reinforced concrete, concrete block, sheetrock, wood and wool composites, plaster, tile, and fiberglass. It has 2-D color display of any detected motion that gives the operator a real-time depiction of the direction and the distance to the target. One of the main problems with RadarVision is its low resolution, and Blob-like results would not identify the shape of targets and would limit its ability to be an effective tool in the field.

ImpSAR from Eureka Aerospace, Eureka Aerospace, a research and development firm based in Pasadena, California, is also developing an UWB STW system. Eureka Aerospace's Synthetic Aperture Radar (ImpSAR) system is capable of imaging targets such as man, weapons, file cabinets, tables etc on the other side of the wall, and at large standoff distances. The ImpSAR radiates short pulses, approximately 100 ps, using an impulse-radiating antenna. A 5 cm resolution in both range and cross-range directions is claimed for the ImpSAR. The system shows identified objects situated behind the walls with sufficient resolution such that a person can be observed including his different body parts.

Xaver 800 from Camero Inc., The Xaver™ 800 is developed by an Israeli based company, Camero Inc.. This system can observe one or more people in a room and continuously monitor their activities. The Xaver 800 was developed to better deal with cluttered environments and to comply with requirements for improved resolution and intuitive imaging. Rapid interpretation of complex scenarios is possible as a result of their extensive development of proprietary 3D image reconstruction algorithms and signal processing techniques. Xaver 800 has been advertised to be able to provide a 3D image around personal.

Radar Scope, This portable UWB through-wall motion detector is developed by L3 CyTerra Corporation, under the sponsor of Defense Advanced Research Projects Agency (DARPA). It is a lightweight portable device, which can sense the presence of human inside walls and 50 ft beyond. This device dose not provide 2D/3D image. It detects the human through motion of body and heartbeat.

Other Government and Academic Efforts, Defense R&D Canada, the research agency of the Canadian Department of National Defense, has extensively investigated UWB through-the-wall surveillance through system modeling and simulation. Proof-of-concept systems been demonstrated, simulation analysis has been reported [11]-[17]. Academic community has also actively involved in STW development, the latest progress are introduced in [18]-[21].

1.3 Limitations of the Available Technology

The minimum functionality of STW system can be itemized as: 1. Determining location of targets in a room, 2. Determining if inhabitants are armed or not, 3. Mapping the contents of the room (tables, doors, windows etc.), 4. Providing the above information in real-time mode, 5. Being a portable system.

The four prototyped systems introduced above represent the state-of-art See-Through-Wall development as of May 2007, but each still has its own limitations. Time Domain's RadarVision, for example, can only fulfill Functionality 1, 4, and 5. It shows a moving object's range and its direction behind a wall in real time, but dose not provide much information about the target itself or the building layout, which makes a significant difference under military operations. Another example, Eureka Aerospace's ImpSAR provides a 2D camera-photo-like image with fine resolution, but as a trade-off, ImpSAR set-up needs to be moved to utilize a large SAR aperture (14 foot) in order to achieve the good image resolution. Xaver 800, a recent addition and sells at $100,000, is superior compared to the other two since Camero claims to give a detailed picture of everything in the room and even 3D image around targets in real time mode. Xaver 800 is the only prototype that meets all five minimum functionalities, but it is expensive and relatively heavy and big. Radar Scope is only a motion detector, which can sense the presence and range of human being behind wall, but not provide any further detailed information.

UWB STW technology has demonstrated up-to-now a great potential to some extent, but numerous improvements still can be envisioned for future systems especially in the image formation and data acquisition. Different from traditional radar operation, STW system has to deal with highly multipath and highly refractive environment, and the highly complicated scattering mechanism makes high-resolution microwave imaging very challenging. The many unsolved technical challenges that need to be tackled include antenna design, complicated propagation channel modeling, array deployments, inhomogeneous background, distortion through complex wall structures, real-time detection, and high-resolution time-efficient imaging method, which are only a partial list. Such studies would require serious theoretical and experimental considerations.

Table 3: Features of Various Systems

System Characteristics	RadarVision	ImpSAR	Xaver 800	Radar Scope
Bandwidth:	1 – 3.5 GHz	3.5 GHz	7 GHz	Unknown
Range Accuracy:	- 1 meter to +1 meter	5 cm	Unknown	N/A
Range:	20 meter	100 meter	20 meter	15 meter
Real-Time Operation	Yes	No	Yes	Yes
Imaging Dimension:	2D	2D	3D	N/A
Stand-off:	10m from structure, detects 10m thru structure	100m from structure, detects 10m thru structure	10m from structure, detects 10m thru structure	Need to attach to wall
Size:	56cm x 35.5cm	Less than 4 cubic foot	84cm x 84cm	Size of a telephone handset
Weight:	4.5 kg	Less than 14 kg	10 kg	< 1 kg
Development Status:	Product available	14 foot aperture.	Product available	Product Available
Price:	> $30,000	Not Available	> $100,000	$1,000

1.4 Motivation and Investigation Areas

The STW community has been aggressively involved in investigating the fundamental problems, such as STW propagation mechanism and time efficient high-resolution imaging formations to improve the STW technology. These studies would require serious theoretical and experimental considerations. Due to the complexity associated with developing a custom STW system, these studies highly dependent on conceptual STW systems, which are comprised of commercial RF/Microwave instruments such as oscilloscopes and network analyzers. A conceptual system will provide necessary experimental capability, but it is a high-cost platform, especially if intending to acquire the real-time capability. Hence the need has arisen for having a standalone, cost-effective, and real-time UWB STW platform, which may facilitate the development of various STW concepts or image formation methods. Not only does a cost-effective UWB hardware platform would be helpful for the STW development, but it can also be applied to solve other related UWB problems such as medical imaging and software defined radios.

The need has arisen for having a practical, cost-effective, and high-performance UWB imaging hardware system for the STW community. Such a system must be portable, relatively simple to implement, and have real-time capability. Non-critical parts of the system, such as oscillator, mixers, filters, and amplifiers, can be Off-the-Shelf components, while the essential parts, such as the UWB signal acquisition system and the antenna, must be customized low-cost designs. Not only does a cost-effective UWB hardware would provide the experimental verification and evaluation of any see-through-wall imaging application, but it can also be applied to solve other UWB problems such as medical imaging, quantitative nondestructive evaluation, and further related applications.

The primary goal of this research is to develop a high-performance real-time STW platform. Once this system is developed, it will be utilized it to study the associated modeling and scattering problems, such as the wall effect on STW imaging and UWB radar signature of various targets, which are essential issues to improve STW system performance. The proposed developed system will complement the existing technologies and will enhance operational effectiveness.

This dissertation is organized as follow. Chapter 2 of this dissertation first addresses the advantage and necessity of utilizing a UWB system in time domain. As an essential step to study the fundamental issues that will guide the STW imaging system development, Chapter 3 will thoroughly study the effect of walls and UWB array deployment on STW image quality through numerical simulation. The UWB scattering mechanism will investigated and shed the lights on real-time system hardware development. Chapter 4 will addresses the wall material characterization over UWB frequency range, which is a key point for selecting the operating frequency for STW detection. Particularly, the study is to characterize the insertion loss of various wall types and develop an efficient through wall propagation model. As part of the standalone system development, Chapter 5 discusses the design and fabrication of a full Synthetic-Aperture-Radar (SAR) array and

its associated switch design. Based on the preliminary study presented from Chapter 2 to Chapter 5, a conceptual demo STW system is developed based on common RF instrument. Experimental results of such a conceptual system are compared to numerical simulation results. A universal STW automation and control subsystem, which is independent of a STW system's operating frequency, is introduced to the STW community. Finally, a standalone reconfigurable STW system is developed in Chapter 7. The real-time data acquisition is a bottleneck of the UWB system development. Chapter 7 introduces for real-time STW application a high-performance low-cost UWB data acquisition module which is based on commercially available low-speed Analog-to-Digital converter and Field-Programmable-Gate-Array (FPGA) technology. Summary and conclusion will be given in Chapter 8.

Chapter 2 . WHY TIME-DOMAIN

In principle, a signal may be represented in either the frequency or time domain, and the conventional radar systems normally reconstruct a signal from discrete samples in the frequency domain. As a first step of building a See-Through-Wall (STW) system, measurements and experiments were carried out to explore the STW features in the frequency domain. The study would reveal the potential advantages of time domain over frequency domain in UWB STW imaging applications.

2.1. Frequency Domain Study

The free-space see-through-wall experiments were carried out to explore the feasibility of STW application. A full anechoic chamber experimental set up was built to effectively perform comprehensive frequency domain measurements on a simplified STW system model. The anechoic chamber absorbs all the multipath signal and reflections and results in most accurate results. The Vector Network Analyzer (VNA) was used to extract a desired component of transmitted/received signal, such as the direct reflection from targets. The time gating feature of the VNA is used to reduce the undesired signal components such as the multi-reflections from the environment. The VNA's frequency domain data is then processed through the embedded Inverse Fourier Transform processor and demonstrated as time-domain pulse data.

Inside the anechoic chamber, a wooden wall is implanted in the anechoic chamber to simulate the STW environment, Figure 2.1 (a). Both the transmitting and receiving antennas are UWB horn antennas (see Figure 2.1 (b)) and were fixed on a 0.5m distance from the wall. The two antennas are attached to HP 87510c network analyzer which was fully 2-port calibrated such that all the cables losses were accounted for in this calibration procedure. The analyzer is adjusted to work between 8-10 GHz. Two typical targets, copper metal sheets of size 50cm X 50cm and an adult male are prepared to thoroughly demonstrate the effect of the target type on the received signal. The distance of targets from the transmitting and receiving antennas and from the wall are flexible to be changed within the experiment.

2.2. Measurement Results

The setup was firstly arranged for monostatic measurements. The blue UWB horn shown in Figure 2.1 (b) was used as both the transmitter and the receiver. The reflected signal which is measured before implanting the wall is shown as the dashed line in Figure 2.1 (a). The quick high reflected pulse around 0.5 ns is due to the cable connection mismatches. After implanting the wall against the antenna with approximately a 55 cm distance, the reflected signal is critically changed to exhibit the multiple reflections induced by the wall. In fact, the transmitted wave is bouncing between the wall and the transmitting horn. This can be verified simply by calculating the delay between two consecutive bounced waves which is equal to the time the wave takes to travel from the transmitting horn hitting the wall and returning back to the horn.

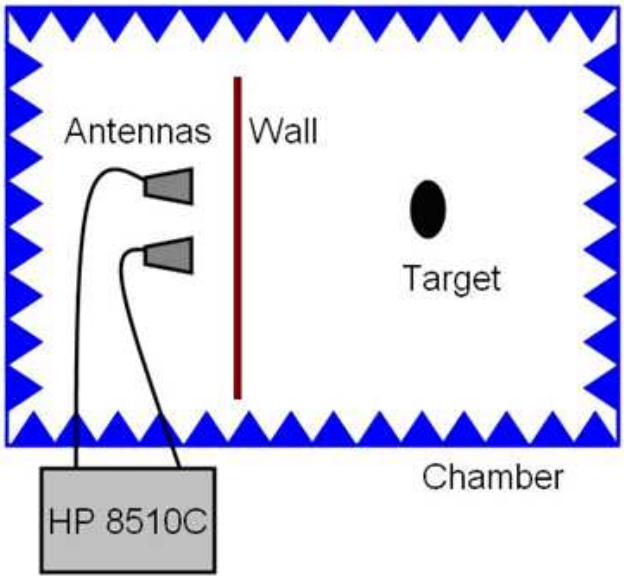

(a) Top View of Chamber

(b) Antennas and Wall

Figure 2.1: Chamber Experiment.

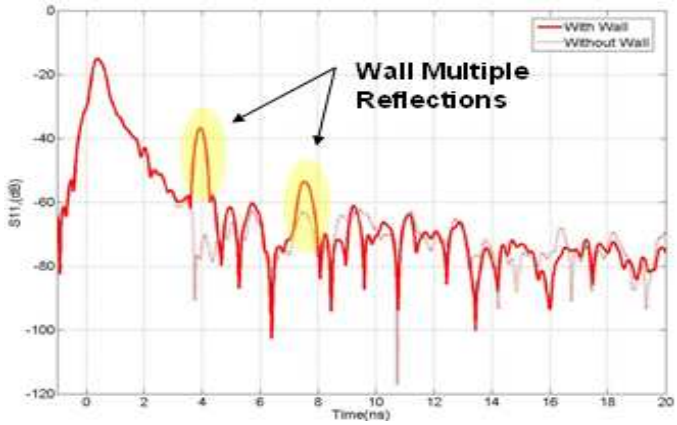

(a) with and without wall.

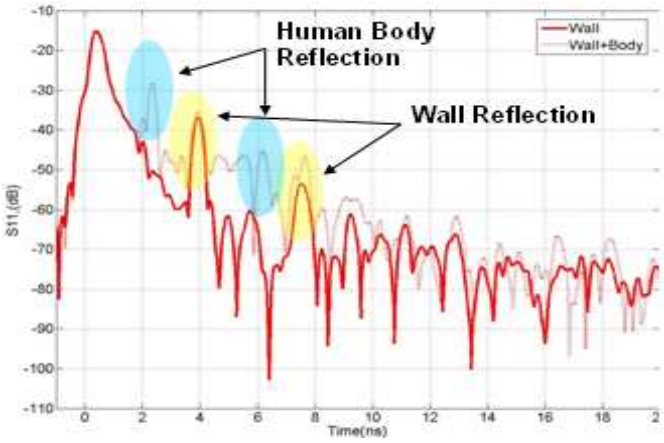

(b) with human body target in front of the wall

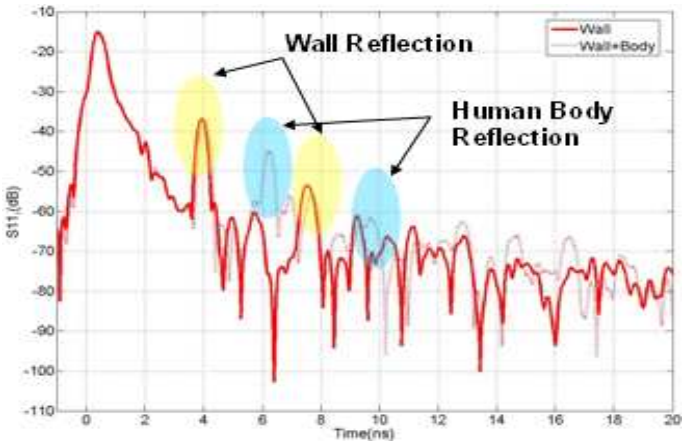

(c) with human body target behind the wall.

Figure 2.2: Monostatic reflected time domain pulse

The next step was to demonstrate the effect of a human body target on the reflected signal. The human target is standing between the horn and the wall first. As shown in Figure 2.2 (b) the multiple reflections from the body can be distinguished from that of the wall. Then moving the human body behind the wall on a further distance (85 cm from the transmitting antenna) will give a clearer view for the reflected signal that would enable us to easily identify the body multiple reflections from that reflections of the wall, as shown in Figure 2.2 (c). Notice here that the wave is bouncing between the transmitting horn, the wall and the human body target.

After measuring human body, the target is switched to a metal sheet while keeping the same target-to-antenna distance. Figure 2.3 compares the pulse signal resulted from the metal and human targets, which are placed at the same distance from the antenna. As expected, a metal sheet will introduce higher reflections and increases the amplitude of the reflected pulse indicated by the VNA.

The anechoic chamber setup was secondly arranged for bistatic measurements. The blue UWB horn Figure 2.1 (a) is used as a transmitter while the white UWB horn is used as the receiver. Both the transmitting and receiving antennas were at the same height of 1.5 m. Similar to the monostatic measurements, the reflected signals are measured before and after implanting the wall, the reflections from the metal and human target are compared as well. The results are plotted in Figure 2.4.

The wall reflections can be identified clearly at around 7 ns as shown in Figure 2.4, which corresponds to the signal's round trip travel time for the transmitter-wall-receiver distance of 1.1m. Adding the human target to the bistatic setup will add extra pulse reflections in the reflected signal at 11ns, again, which corresponds to the signal's travel time for the transmitter-body-receiver distance of 3.4m. There is a second pulse response at 16 ns, which is caused by the multiple reflections from the human body. Replacing the human target with the metal sheet increases the amplitude of the reflected pulse by almost 20 dB, shown in Figure 2.4(c), due to the higher reflection from the metal.

The above measurements are carried in the frequency domain using the VNA. The time domain pulse information has been converted from the frequency domain through FFT. The results reveal a lot of important information, for example the multiple reflections observed in the time domain will help in the extraction of the target range. The amplitude level of these reflections too will help in identifying the target type. At a first glance, the frequency domain operation could provide all necessary information to implement the STW application. Then, why would we be developing an UWB time domain system? In next section, we will compare the advantages and the disadvantages between the frequency and time domains, and rationalize the need of time domain operation for STW.

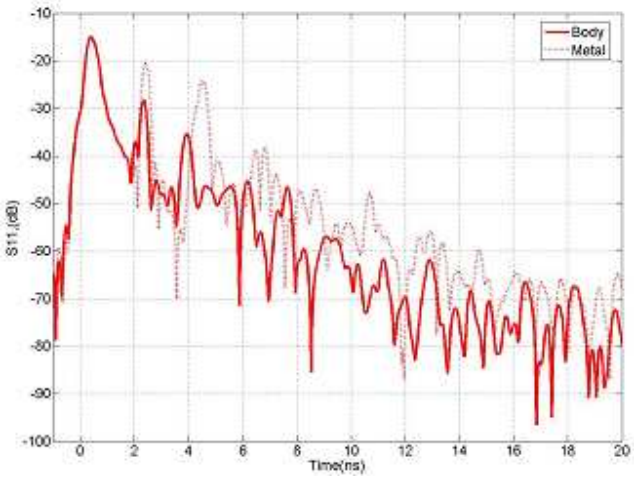

(a) human vs. metal targets in front of the wall.

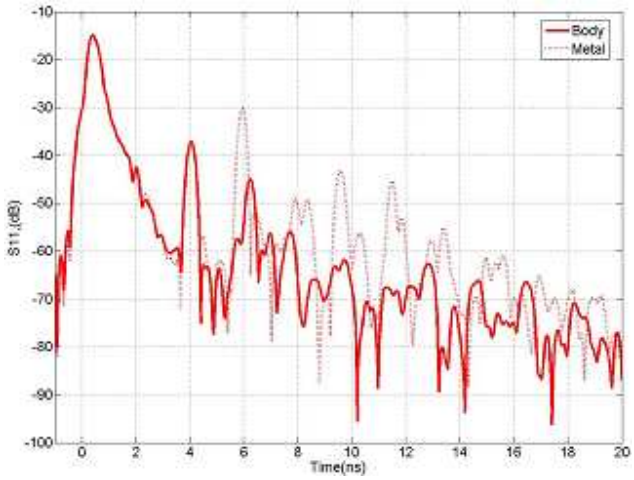

(b) targets behind the wall.

Figure 2.3: Monostatic reflected time domain pulse.

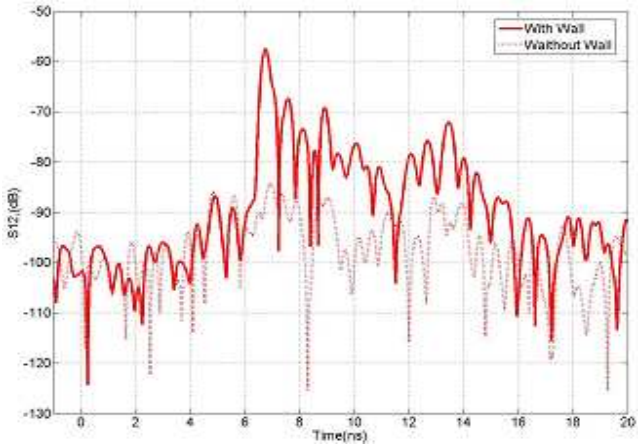

(a) with and without wall.

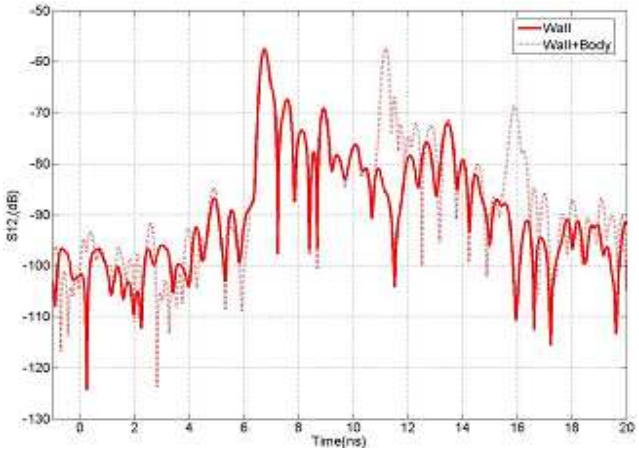

(b) with human target in front of the wall.

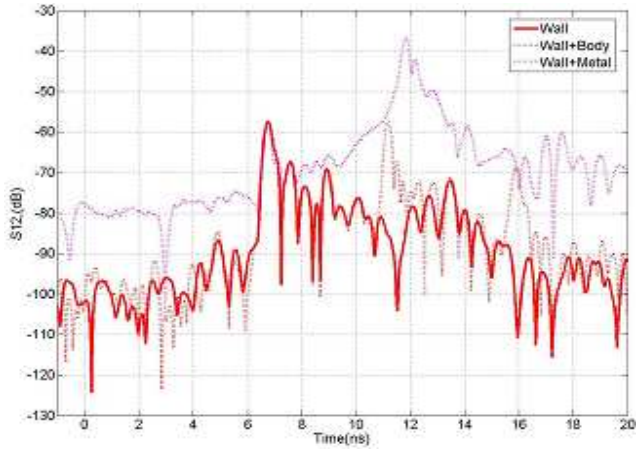

(c) with human body target behind the wall.

Figure 2.4: Bistatic reflected time domain pulse

2.3. Why in Time-Domain

This section is to investigate the differences between carrying out STW measurements directly in the time domain and carrying out the same measurements in the frequency domain then transforming the collected data to the time domain. A brief comparison between the two approaches is given first. Table 4 shows the advantages and disadvantages of carrying these measurements at either time or frequency domain. It is clear that the time domain method is less complex but it is more susceptible to various sources of noise. Frequency domain measurements, on the other hand, have better control on calibration and power levels. The frequency domain and the time domain data are connected through Fourier Transform.

For a time window size T and number of sampling points N, define the sample spacing $\tau = T/N$ and the sample points $t_k = k\tau$, for k = 0, 1, …, (N-1), then define a discrete time domain signal as:

$$f_k = f(t_k) \qquad \textbf{(2.1)}$$

Associated with this we define the frequency sampling points $\omega_n = \frac{2\pi n}{T}$, where the number $\frac{2\pi}{T}$ is the fundamental frequency. Now let's consider the problem of approximating the FT of f at the points $\omega_n = \frac{2\pi n}{T}$ and have

$$F(\omega_n) = \int_0^T e^{-i\omega_n t} f(t)dt \text{, n = 0, 1, …, } (N\text{-1}). \qquad \textbf{(2.2)}$$

If approximating this integral by a left-endpoint Riemann sum approximation using the points t_k defined above:

$$F(\omega_n) \approx \tau \sum_{k=0}^{N-1} e^{-i\omega_n t_k} f(t_k) \text{, n = 0, 1, …, (N-1).} \qquad \textbf{(2.3)}$$

Substitute the definition of ω_n, t_k and τ and have,

$$F(\omega_n) \approx \frac{T}{N} \sum_{k=0}^{N-1} e^{-i2\pi nk/N} f(t_k) \text{, n = 0, 1, …, (N-1)} \qquad \textbf{(2.3)}$$

Let's consider a time domain pulse signal of 200ns period, which can be translated to 30m radar detection range by

$$D = \frac{T * C}{2} = \frac{200ns * 3e8m/s}{2} = 30m \qquad \textbf{(2.4)}$$

Assuming the pulse signal is sampled at 100ps/sample interval for a desired range resolution, the system bandwidth is:

$$BW = \frac{0.35}{\tau} = \frac{0.35}{100\,ps} = 3.5GHz \qquad \textbf{(2.5)}$$

To replicate the same system in the frequency domain, the frequency source need to have 3.5 GHz range, and sweeps at a step of 5MHz,

$$f_n = \frac{\omega_n}{2\pi} = \frac{n}{T} = \frac{n}{200ns} = n * 5MHz \qquad \textbf{(2.6)}$$

A total of 700 frequency points need to be swept across the 3.5 GHz range to achieve the equivalent time-domain operation. A network analyzer provides a maximum of 800 sampling points within a certain bandwidth. However, the network analyzer represents the state-of-art frequency domain measurement techniques. It is impractical to implement such kind of a high performance swept signal source in a standalone UWB system as it is quite expensive too. The operation in the frequency further places a constraint on the achievable resolution in the STW application.

On the one hand, the operation of an UWB system in the frequency domain is limited by its complexity in the signal source and signal processing. On the other hand, the advance of UWB hardware technology has made it relatively an easy task to directly generate and process UWB time-domain pulse signal. Hence, the time domain processing becomes an attractive option for a STW imaging system.

Table 4: Comparison between Time and Frequency domain measurements

Time Domain	***Frequency Domain***
Requires only a single measurement	Requires measurements over a set of discrete frequencies
Waveform gives insight into the physical problem at hand	Requires manipulations such as IFT to visualize the data
Operates directly on time domain data avoiding transform errors	Errors are introduced upon using Fourier and inverse Fourier transforms
More susceptible to noise Existing algorithms are only for CW not transient signals	Wide varieties of noise reduction algorithms are very efficient. Not limited by signals waveforms as frequency domain convolution circuitry can be used before using Fourier transforms.
Measurements are limited by the generated pulse characteristics including any time jitter	
Requires a trigger signal that will suffer more attenuation and dispersion for longer distances between the transmitter and receiver	The VNA requires cable connection and its attenuation could be calibrated
Digital sampling oscilloscopes are not common	Standard equipment, narrow band amplifiers are cheap
The time required for data acquisition limit the measurements to slow varying channels	The sweeping time is the limiting factor for acquiring the impulse response
Preserves the causal and stable signals	Using filters and the Fourier transform could cause non-causal and instability

Chapter 3 . STW SIMULATION BASED ON CFDTD

Microwave imaging is typically an EM inverse scattering problem, which has been widely studied due to its increasing range of applications, such as target identification, medical imaging, material characterization, geophysical survey, remote sensing, nondestructive evaluation, and now See-Through-Wall imaging [27]-[39]. STW could be basically a Synthetic aperture radar (SAR) based system, and therefore imaging methods generally developed for conventional radar systems can be efficiently used for STW application as well after taking STW's unique features into account like antennas' locations constraints and the wall loss and dispersion. High-resolution SAR imaging algorithms, such as domain integral equation, diffraction tomography, model fitting method, and migration method, which are classified and discussed in [27] all could have potential implementation in STW systems.

The use of the STW systems is mainly dependent on the development of an image formation technique to reconstruct raw radar signals and literally and rapidly interpret it in terms of target type and shape. However, the electromagnetic environment associated with the STW scenarios, and the complex wall and building structures introduce new challenges to the image formation, compared to the conventional SAR technology. The new EM environment needs to be studied to provide the necessary design guidelines for the system development.

In a large scale, STW community is interested in the radar imagery of full rooms or whole buildings, including humans and other objects inside these buildings. Particularly, the effect of wall structure needs to be analyzed so that advanced image formation method can be developed to compensate for the image distortion due to this effect and provide better STW image quality.

Such studies can be carried out efficiently through numerical simulation. Considering the scale of this problem, the Finite Difference Time Domain (FDTD) method, a full-wave time-domain numerical procedure, is an ideal tool for UWB simulation since it provides direct solution of the time dependent Maxwell's curl equations using the finite-difference technique [41][42]. By time stepping, the incident wave is tracked as it first propagates to the structure and then interacts with the latter through current excitation, scattering, multiple scattering, penetration and diffraction.

The simulation study is carried out here using a Conformal Finite Difference Time Domain (CFDTD) software package (see Figure 3.1) [49]. A room with a floor and walls of various materials is modeled as shown in Figure 3.2. Transmitting and receiving antennas are located outside the room and radiating an UWB pulse, and targets with different size/type are placed inside. The scattered field due to the targets is calculated and recorded at the receiver position. The modeled room (3.5m x 2.5m x 2.4m) used here, as an example, has a concrete floor and 3cm-thick drywall walls. Two 30cm conducting cubic boxes are placed inside the room as targets. One transmitter and sixteen receiver points are distributed at the side of the room in the XZ plane, corresponding to a

transmitting horn and a 16-element receiving array. The receiver points are observation points where the EM field magnitudes are recorded and saved for post-processing. The UWB source is a 1ns Gaussian pulse centered at 2 GHz (shown in Figure 3.3), and the model cell is 1cm cubic, the size of which corresponds to $1/15^{th}$ of a wavelength at 2 GHz.

The simulation focuses on the following parametric studies:

1. The effect of the wall materials on the image.
2. The effect of the receiver and transmitter numbers on the image.
3. The effect of the array element spacing distances on the image.
4. The effect of the center frequency and pulse width on the image.

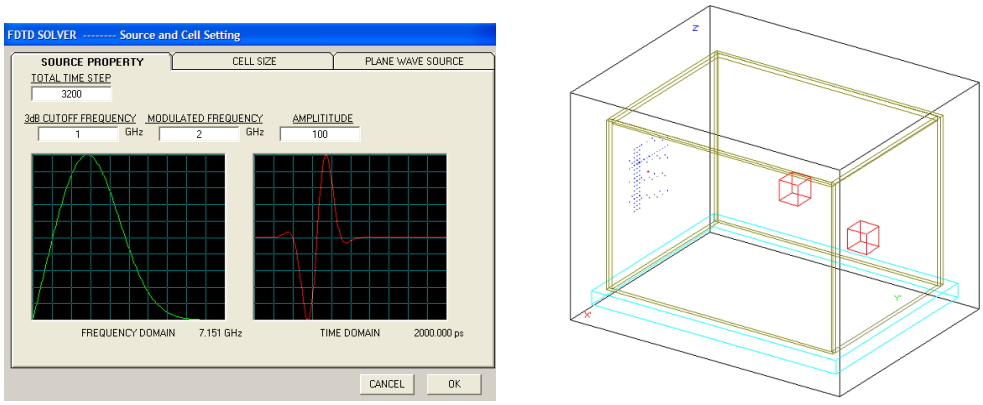

Figure 3.1: CFDTD User Interface.

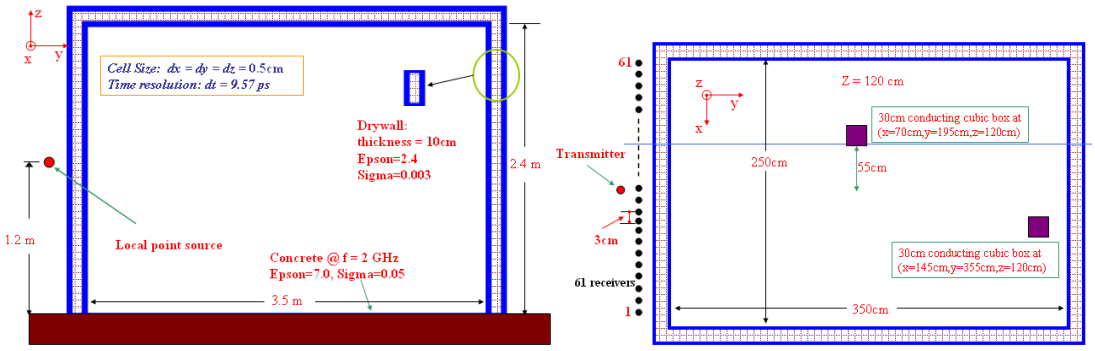

Figure 3.2: CFDTD Model Geometry.

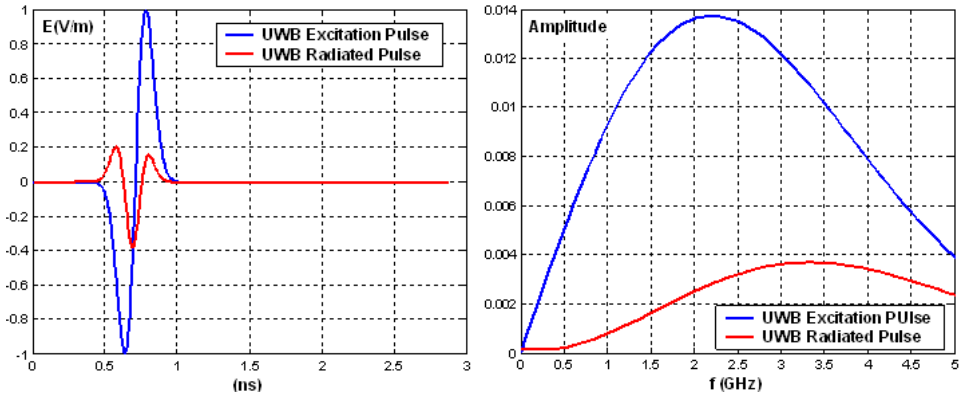

(a) UWB Pulse in Time Domain (b) UWB Pulse in Frequency Domain

Figure 3.3: UWB Pulse.

3.1. Implemented Image Formation Methods

The purpose of this simulation is to study the wall effect in STW various scenarios. Since the development of an advanced STW image method is beyond the scope of this dissertation's work, only well-established UWB SAR algorithms will be implemented here to process the simulation data and study the wall effects. Although an efficient high-performance STW algorithm is not yet available, but progress has been reported to modify the classical SAR algorithms for STW radar [18]-[20], which has also been used in our study. For the completeness of the discussion, the implemented image formation methods are outlined in this section.

A. Sum-and-Delay Far-Field Synthetic Beamforming

The synthetic beam-forming process is shown in Figure 3.4, [40] . Focusing of the beam in a direction θ implies that the summation of all the received signals should produce a maximum value for that particular direction. Since the received In-phase and Quadrature signals may be seen as vectors, the summation is equivalent to equating their phases so that the resulting sum will produce a maximum for that direction. It is accomplished by applying the proper phase shifts to each channel of the received signals. In SAR, these phase shifts are applied to array signals by software in post-processing stage, to form a synthetic beam at the particular direction. Signals coming from all other directions or angles will not add up to produce a maximum beam.

Once the data acquisition is completed on each receiving array element, the antenna outputs can be combined with the proper phases and amplitudes to focus the beam in any direction. Let $s_i(t)$ be the complex received signal from antenna "*i*", then the time-domain sample of the received signal is:

$$s_i(n) = x_i(n) + jy_i(n) \qquad \textbf{(3.1)}$$

where x_i and y_i are the in-phase and quadrature components of the received signal. The output I_j for a direction θ_j as a function of the time sample *n* is given by the following relation:

$$I_j(n) = \sum_i^N w_i s_i(n) e^{j\varphi_{i,j}} \qquad \textbf{(3.2)}$$

This equation assumes that all the signals coming to the antennas follow parallel paths. This assumption is valid only if the target is located in the far field of the antenna. Focusing of the beam in the near field implies that the phase correction will depend on the target range as well. In this case, the beam is focused to a single point instead of a particular direction. Near-field focusing would increase the computational burden by a factor of possibly a few hundred times. Backprojection is typical near-field SAR image formation method, and will be briefed next section.

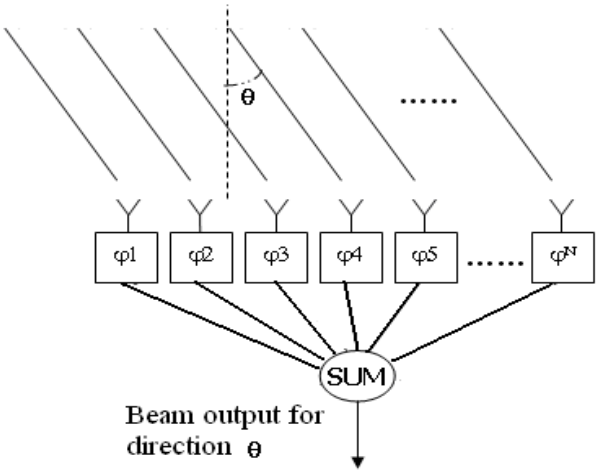

Figure 3.4: Synthetic Beamforming Process.

B. Near-Field Backprojection

The principle of backprojection method is to calculate the beamforming output power at specified grid points in the x-y-z three-dimensional domain [40]. Considering a bistatic radar of a single transmitter and an *L*-element receiver array, both located in the XY-plane, as shown in Figure 3.5, the problem is simplified to a two-dimensional case. Assuming that an isotropic point target is located at the coordinate origin, any of the receiver elements is at a distance R away from the target. The region of interest will be divided into a finite number of grids in the x-y-x 3D domain. An imaging space enclosing the point target can be defined by an M-by-N-by-K matrix with indices m=1,…, M, n=1,…, N, and p=1,…, P, corresponding to x, y, and z axis respectively. If M=1, N=1, or P=1, the imaging space is reduced to a 2D image plane. The complex amplitude of an image pixel at the (m, n, p) grid is obtained by applying time delays to the corresponding receiver data, and producing the image through backprojection method. The backprojected field intensity from the (m, n, k)th grid due to the l^{th} receiver can be represented by

$$I(l,m,n,p) = [d_{rl}(m,n,p)d_t(m,n,p)] * s_l(t)\,|_{t=[d_r(m,n,p)+d_t(m,n,p)]/c} \quad \textbf{(3.3)}$$

Where s_l is the time domain signal from l^{th} receiver, d_{rl} is the Cartesian distance between the grid point (m, n, p) and l^{th} receiver, d_t is the Cartesian distance between the grid point (m, n, p) and the fixed position of the transmitter, $t = [d_r(m,n,p) + d_t(m,n,p)]/c$ is the signal transit time from the transmitter and to lth receiver, and c is the speed of light. The total back-projected field intensity at the (m, n, p) grid point is summed over all the *L* receivers as

$$I_{total}(m,n,p) = \sum_{l=1}^{L} I(l,m,n,p) \quad \textbf{(3.4)}$$

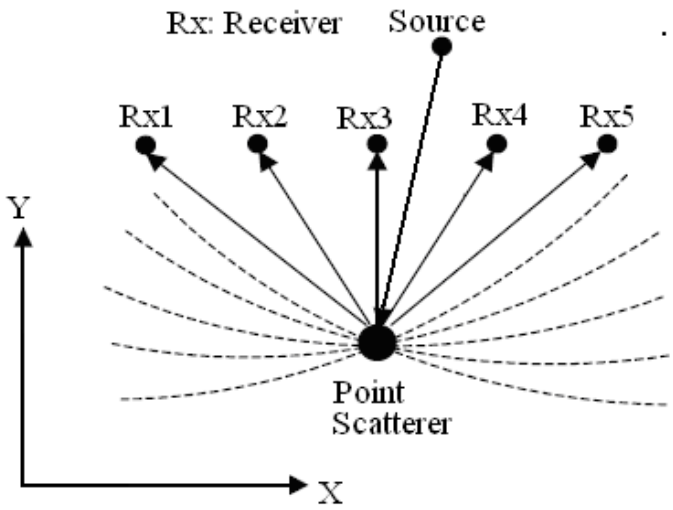

Figure 3.5: Back Projection.

Different from the demodulated baseband complex signal $s_i(t)$ used in (3.1), $s_l(t)$ in (3.3) represents the received radar signal before I/Q demodulation, which is the return pulse modulated at the carrier frequency. Since the demodulation moves the modulated pulse signal from carrier frequency down to the baseband in the spectrum domain, s_l can be constructed directly from the measured I/Q signal. By the nature of the I/Q signal, first we convert the I/Q complex waveform to the real transmitted pulse waveform as follows,

$$s_i^r(t) = sign[x_i(t)] * \sqrt{x_i^2(t) + y_i^2(t)} \qquad \textbf{(3.5)}$$

where the operation *sign*[ ] takes the positive or negative sign of I channel signal as the phase and the square root is the magnitude of the converted signal. Then we re-modulate the converted signal $s_i^r(t)$ by Fourier Transform $s_i^r(t)$ and shifting the baseband spectrum to carrier frequency and this operation is shown as follows,

$$S_l(f) = S_i^r(f - f_c) = (FFT\ [s_i^r(t)])\ |_{f = f - f_c} \qquad \textbf{(3.6)}$$

Finally, $s_l(t)$ is the inverse Fourier Transform of (3.6),

$$s_l(t) = IFFT\ [S_l(f)] \qquad \textbf{(3.7)}$$

Once I/Q signals are measured, Operations (3.5) – (3.7) can be done in software. Since $x_i(t)$ and $y_i(t)$ are actually the time-domain samples $x_i(n)$ and $y_i(n)$ and digital Fourier Transform is required.

The back projection shown in (3.3) can also be processed by applying frequency-dependent phase delays in the frequency domain. Replacing the time domain signal by its

frequency domain representation $s_l = \sum_{k=1}^{K} S_l(\omega_k) e^{j\omega_k t}$ in (3.3), the back projection becomes,

$$I(l,m,n,p) = [d_{rl}(m,n,p) d_t(m,n,p)] * \sum_{k=1}^{K} S_l(f_k) e^{j2\pi f_k t} \mid_{t=[d_r(m,n,p)+d_t(m,n,p)]/c} \quad \textbf{(3.8)}$$

For better accuracy, the *I(l, m, n, p)* can be normalized with respect to the pattern of the transmitting and receiving antennas.

C. Correction of Defocused Image through Dielectric Walls

The classical microwave imaging techniques based on free-space line-of-sight propagation can be used for STW application after accounting for the presence of the dielectric wall present between the targets and the radar. The wall will introduce significant target image distortion if not corrected. The effect of the wall includes multiple reflection, refraction, and dispersion. The refraction due to the interface of two different medians can be corrected with a time domain method.

The simplest model for the dielectric wall with a uniform thickness *t* and dielectric constant ε_r is shown in Figure 3.6. We assume the wall size in length and height is very large compared to one wavelength of the radar signal. Considering a 2D imaging case, where a 1D array is deployed along the x-axis in the XY plane and the propagation path is only in the XY plane. A point target is placed at position *P(Xp, Yp, Z)* at one side of the wall, and a transmitter or a receiver at position $R(X_r, Y_r, Z)$ at the other side. When no wall is present between the target and the radar, the signal path between the point target P and the receiver R is the Cartesian distance given by,

$$d_r = \sqrt{(X_p - X_r)^2 + (Y_p - Y_r)^2} \,. \quad \textbf{(3.9)}$$

Similarly, assuming a transmitter $T(X_t, Y_t, Z)$, the signal path between P and T is,

$$d_r = \sqrt{(X_p - X_t)^2 + (Y_p - Y_t)^2} \,. \quad \textbf{(3.10)}$$

The total time delay of received signal is

$$t = [d_r(m,n,p) + d_t(m,n,p)] / c \,. \quad \textbf{(3.11)}$$

When a wall slab is placed between the target and the radar, the geometric signal path between the target and receiver is different from free space case and is represented by

$$L = L_1 + L_2 + L_3 , \quad \textbf{(3.12)}$$

and the actual electrical length is,

$$L_{ef} = L_1 + \sqrt{\varepsilon_r} L_2 + L_3 \,. \quad \textbf{(3.13)}$$

The actual electrical length of the signal path could be significantly greater than that in free space. If not taking the wall effect into account while imaging, severe distortion in terms of range and shape prediction is expected. A common method to solve this 'geometrical' problem is to find the actual electrical length of path, $L_{ef,}$ through numerical iteration and minimization. Assuming the wall thickness "*t*" and the dielectric constant ε_r are known, the only difficulty in finding L_{ef} *is to* determine the intercepting points where the ray strikes the front and back interfaces and reaches the observation point. Once the intercepting points are identified, the ray paths in air and inside the dielectric wall can be easily solved. Of course real life practical problems would include more unknowns like wall thickness, layer structure, and its properties. Snell's Law of refraction can be used to determine the intercepting point; it states,

$$n_0 \sin \theta_1 = n_1 \sin \theta_3 , \quad \textbf{(3.14)}$$

where n_0 and n_1 are the refractive index in air and inside the wall, respectively. Assuming the wall to be non-magnetic, Snell's Law becomes

$$\sin \theta_1 = \sqrt{\varepsilon_r} \sin \theta_3 \quad \textbf{(3.15)}$$

$$\sin \theta_2 = \sqrt{\varepsilon_r} \sin \theta_4 \quad \textbf{(3.16)}$$

When iterating the trial intercepting points on the interfaces, Snell's Law and Ray optics are satisfied only at the actual intercepting point. Once the intercepting point is identified, the actual values of L_1, L_2, and L_3 will be calculated using Snell's Law and further used to correct image distortion. Authors in [20] developed an iterative algorithm to solve the problem of the unknown thickness and dielectric constant. However, a computationally efficient algorithm is still not available yet.

In the previous correction process, prior knowledge of the wall properties, such as wall thickness t and dielectric constant ε_r are required. Under practical conditions, such information is usually unknown to the operator, therefore, must be derived from the received signal. The overall electrical delay caused by the wall can be obtained from the reflection and transmission measurements, thus the electrical thickness of the wall can be estimated. However, different combination of physical thickness and dielectric constant can produce the same electrical delay through dielectric walls. The work here will not discuss the solution to estimate the wall parameters from the reflection and transmission data, but some references are provided. The authors in [17] proposed a method based on the magnitude of the reflection coefficients and of one the transmission coefficient to determine the complex refractive index of concrete. The method only requires a single frequency, but it demands the measurement of reflection coefficients from many incidence angles plus a transmission coefficient, and the thickness of the material must be known a priori. The author in [18] developed several practical and fast algorithms to estimate the property of the wall slab without the need for any prior information of the material.

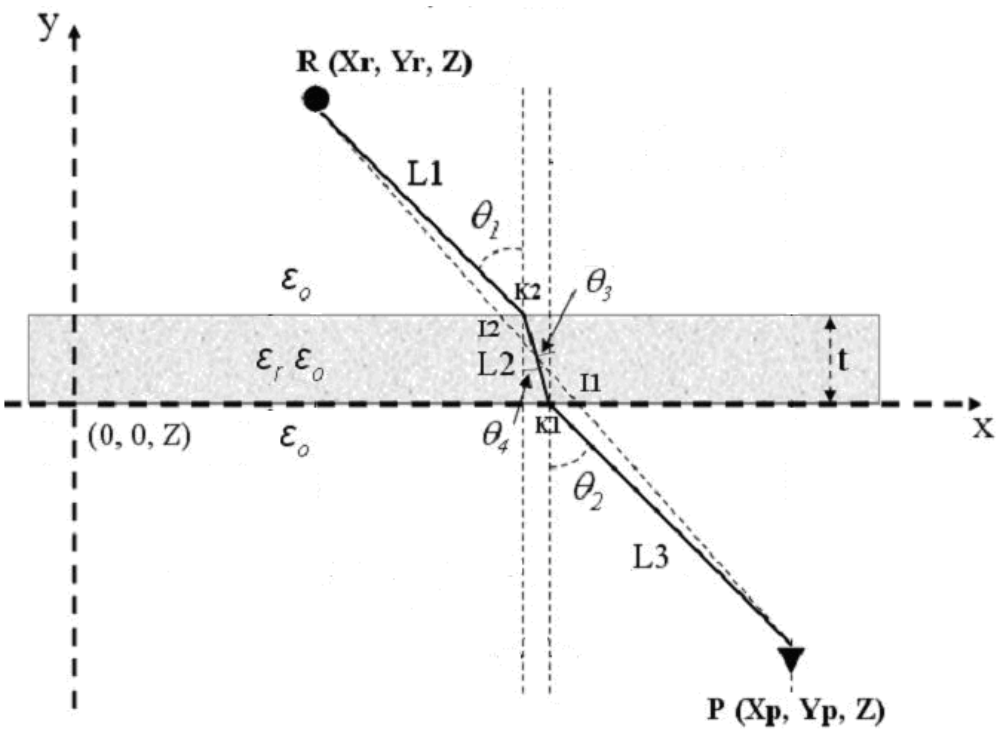

Figure 3.6: Dielectric Wall Model.

3.2. Simulation Result

A. Single Target at Various Locations

Using the back projection formation methods, the images of a 10-cm cubic conducting box at locations P1-P8 inside the room are generated. All 61 receiver elements are used and their element spacing is 3 cm. The coordinates of these locations are shown in Figure 3.7. Figure 3.8 shows the recorded response at the center receiver element when the box is placed at different positions. The first and second pulses (the second pulse is encircled in red) correspond to the reflecting signal from the front and back interface of the wall layer. The traveling distance between these two pulsed responses is around 30 cm, which matches the round-trip electrical length while propagating in the wall slab. Compared to the reflection from the wall, the target response is very small and invisible, and therefore the time-gating is used to eliminate the wall effect and show the reflection from the target, which is demonstrated in Figure 3.9. The time-gated signal is used to generate the images of the conducting box at locations P1-P8. The image for each location is displayed by Figure 3.10. Every image is normalized to the peak magnitude level and only the magnitudes from 0 to -16 dB are displayed. For locations 1, 2, 3, 5, 6, and 7, the box image is displayed more clearly due to a stronger return signal to the receivers on the side of the room, as compared to that of the other locations 4 and 8. While the box is at locations 4 and 8, stronger side lobes are observed because the decreasing magnitude of the reflected signal, which is comparable to the reflection from the room structure. The box at location 1 (line of sight) generates the most focused image compared to others. In general, as the box moves farther away and aside from the UWB radar setup, the generated image is more out of focus than that of location 1. This is attributed to the decreasing magnitude of the reflected signal, the dispersion of the propagating pulse, and the decreasing magnitude of the reflected signals. It shows the receiving isolated impulse response at *Rx41* as the conducting box travels inside the room in steps of 20 cm.

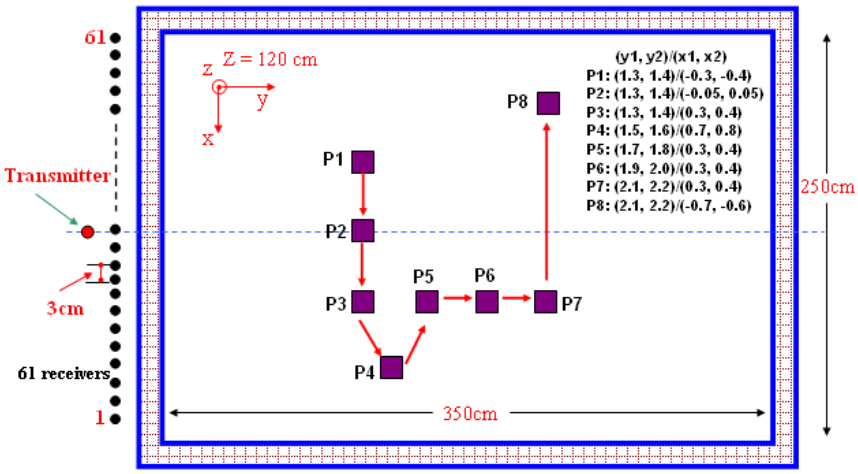

Figure 3.7: A Target at Various Positions.

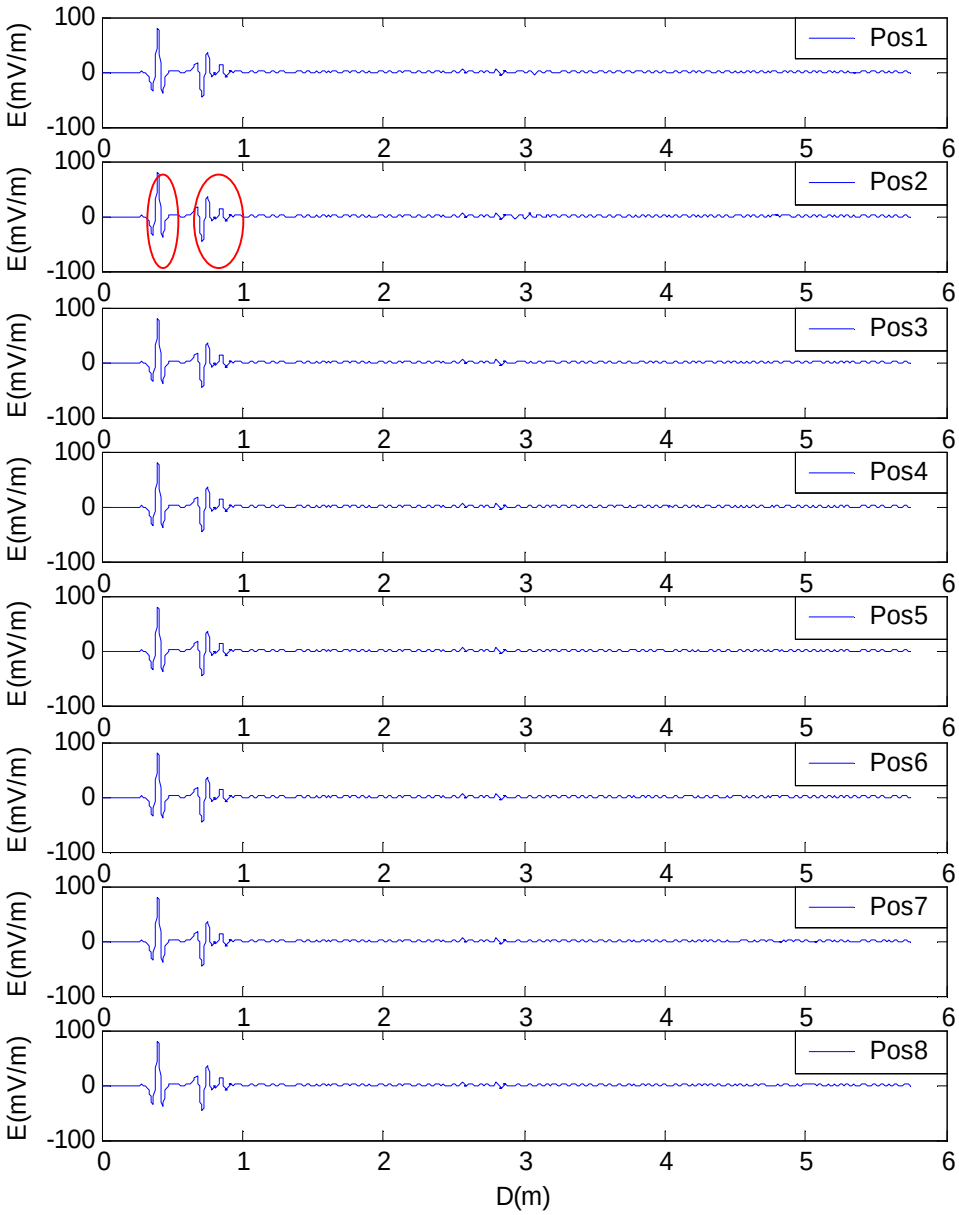

Figure 3.8: Recorded Response at the centered receiver element.

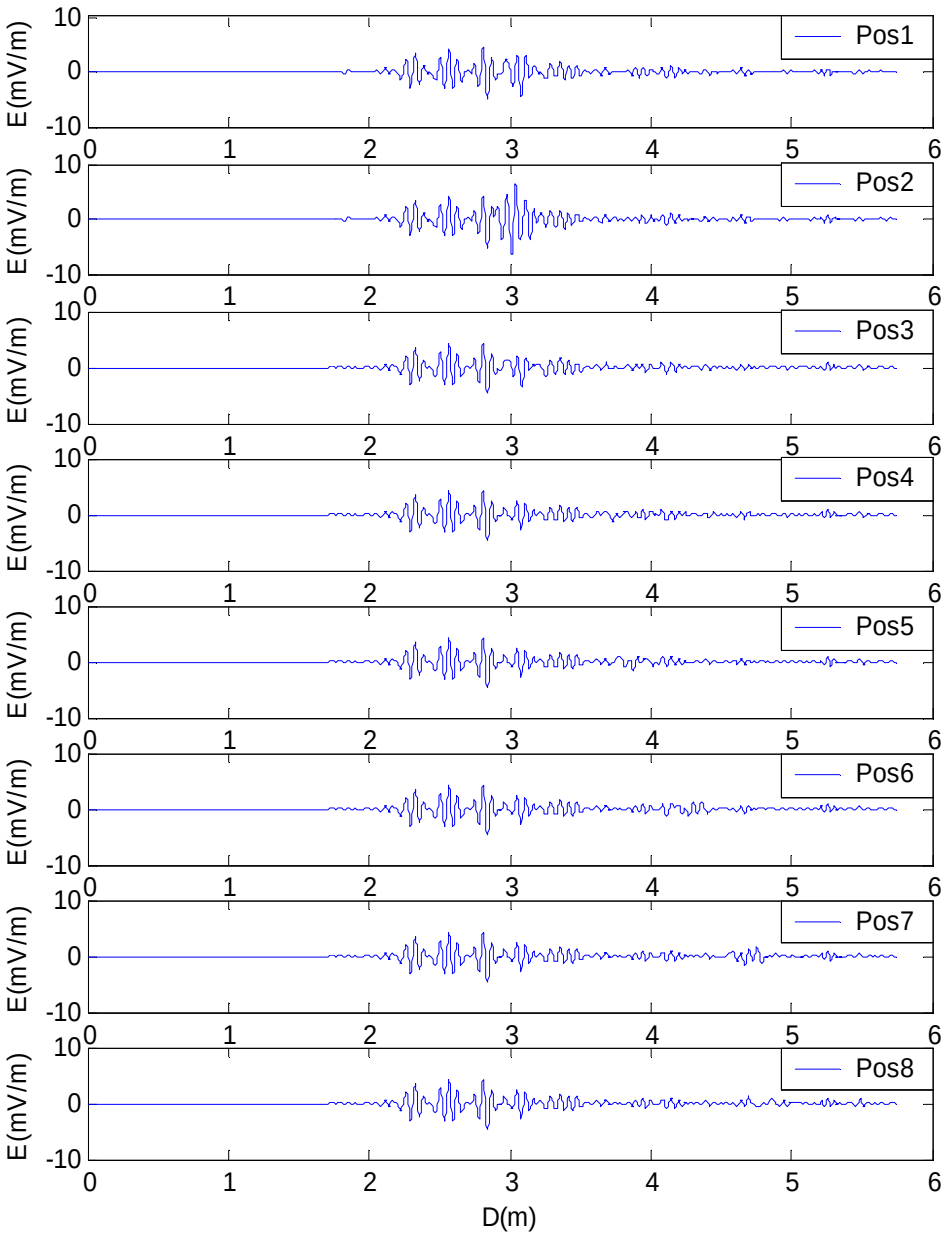

Figure 3.9: Time-Gated Response at the centered receiver element.

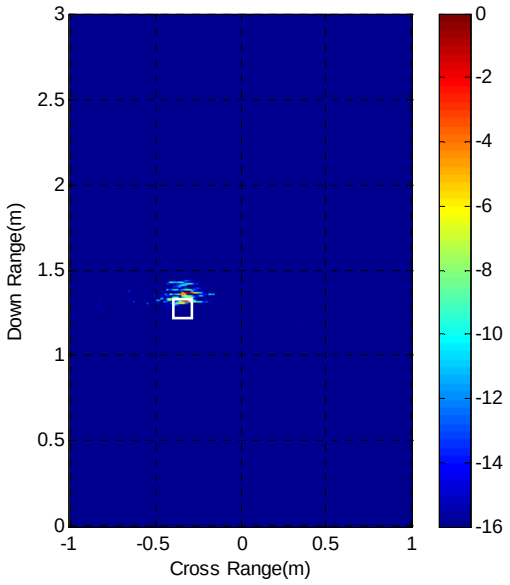

(1) Location P1

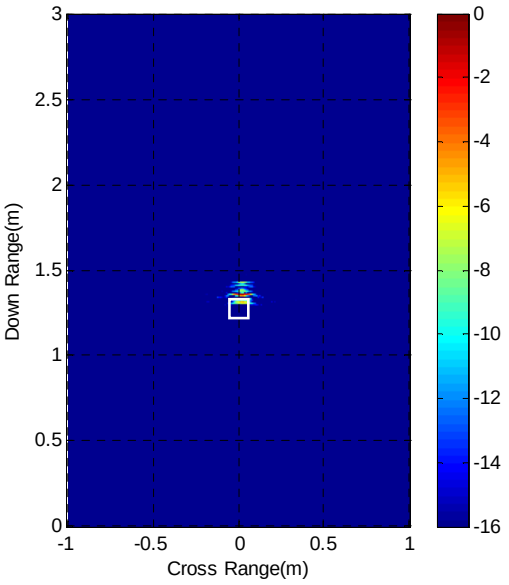

(2) Location P2

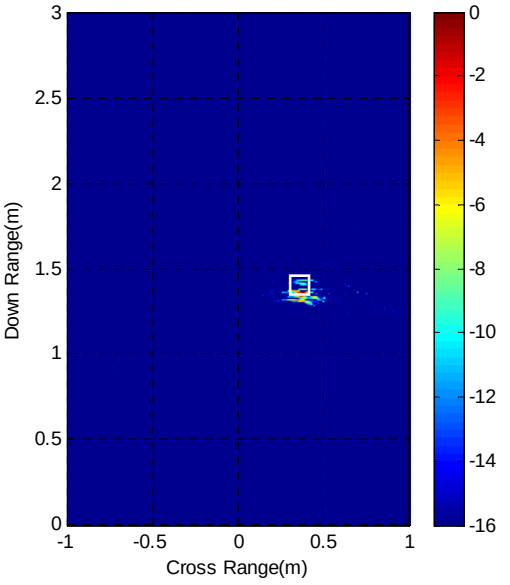

(3) Location P3

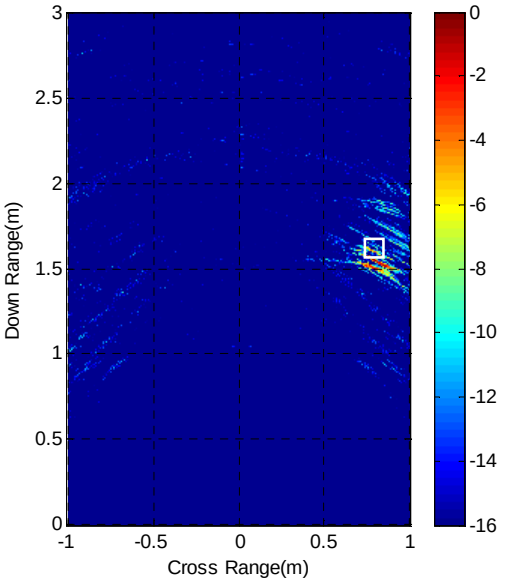

(4) Location P4

Figure 3.10: Images of Box at Different Locations.

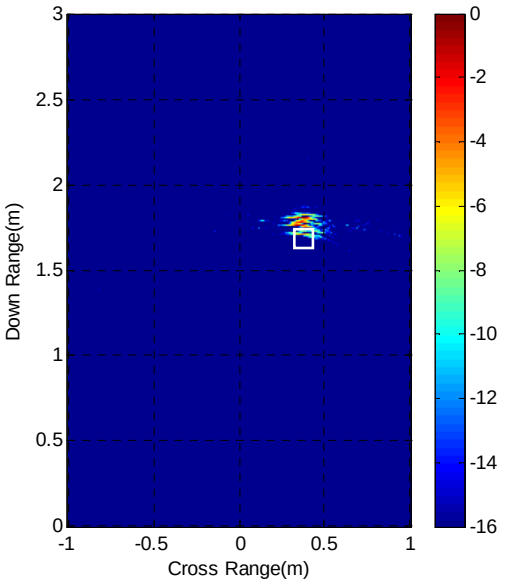

(5) Location P5

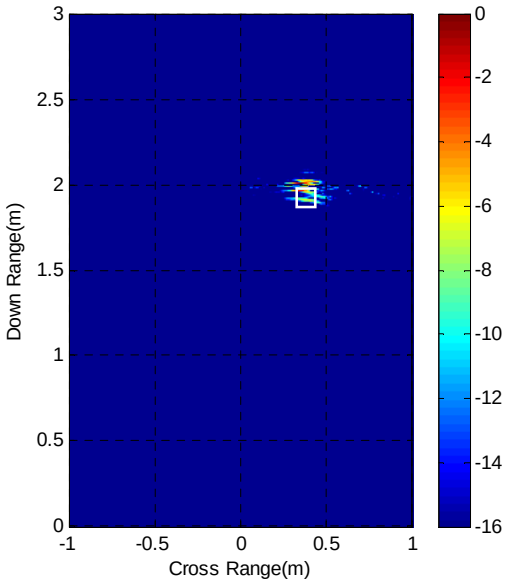

(6) Location P6

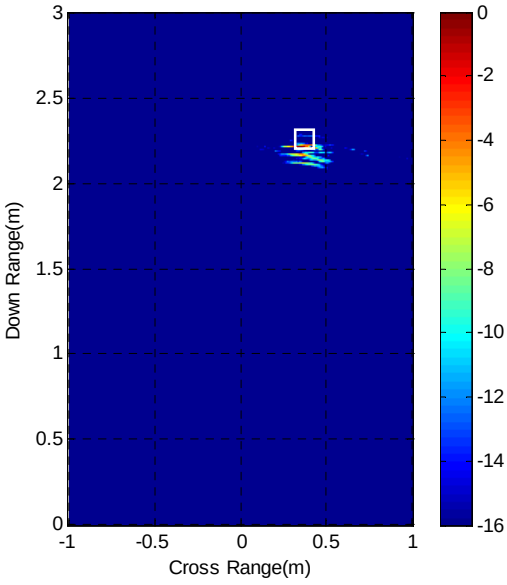

(7) Location P7

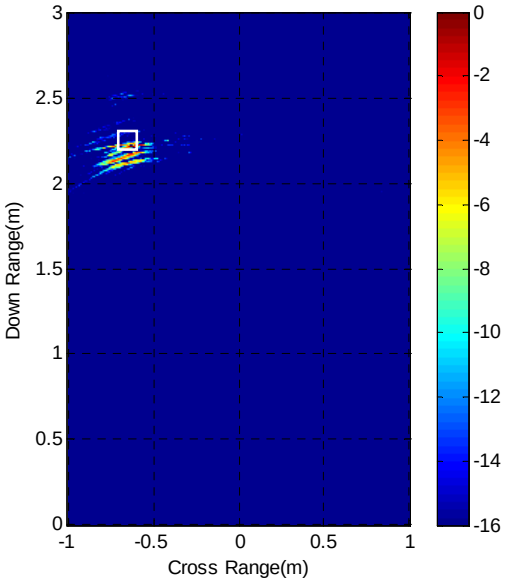

(8) Location P8

Figure 3.10: Continued.

B. Effect of Aperture Size and Number of Elements

The array element spacing distance *d* and the array aperture length *L* have significant effects on the image quality. Figure 3.12 displays the images for different values of *d* but for a fixed value of *L*=180 cm; the smaller *N*, i.e. the number of receivers used the larger the value of spacing *d*. The *N* is the number of receivers utilized in image formation. With an aperture length *D* = 180 cm, the resolution of the generated images, representing the conducting box, are the same for all the cases studied in terms of the image focusing. However, a larger spacing distance *d*, which corresponds to a smaller number of receivers, would result in higher sidelobe levels and the existence of false targets or elevated noise background as seen in Fig,. 3.11. Next, we fix the number of used receivers to generate images to be 15, while changing the spacing distance *d* from 3 cm to 12 cm. Figure 3.13 shows the effect of such move, where the larger the spacing distance d with the same number of receivers, more focused images will be generated because of the larger value of *L*. In general, larger aperture size *L* is preferred to generate better focused images. In Figure 3.13, the image pixel value threshold is set at -16 dB for viewing the sidelobes effects. Figure 3.14 resets the threshold at -6 dB and only plots the peak magnitude of the image pixels. Figure 3.14 clearly shows a better image focusing, while increasing the aperture size.

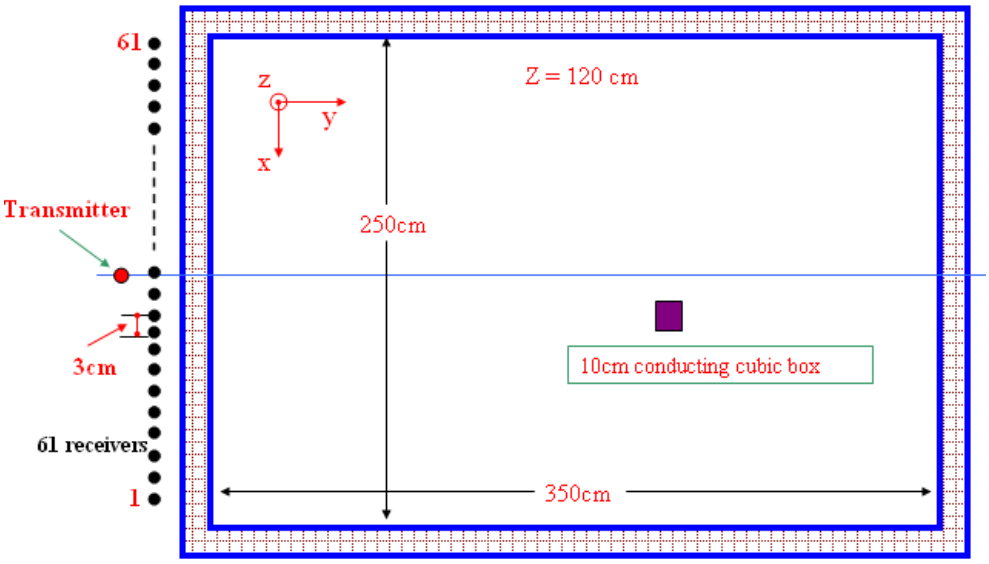

Figure 3.11: Target Location.

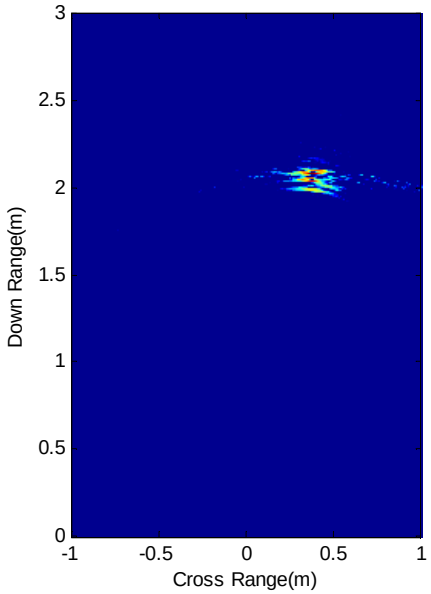

(1) N = 60, L= 180 cm, d= 3 cm

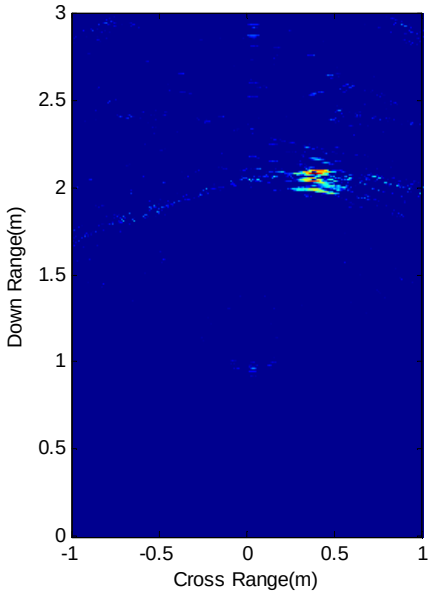

(2) N = 30, L= 180 cm, d= 6 cm

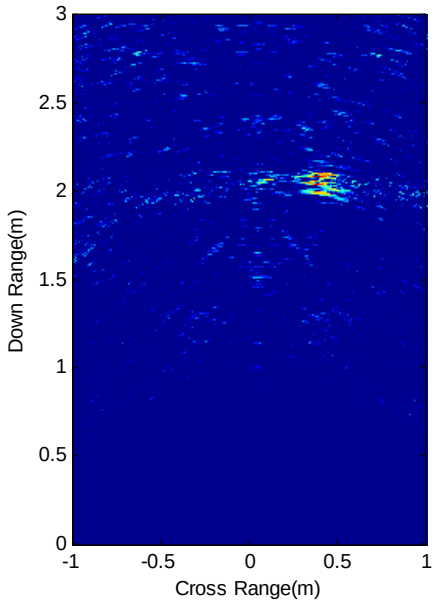

(3) N = 20, L= 180 cm, d= 9 cm

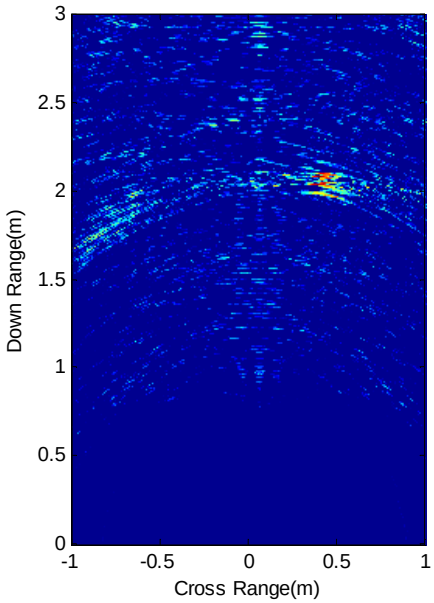

(4) N = 15, L= 180 cm, d= 12 cm

Figure 3.12: Images Generated with Fixed Aperture and Various Elements Number.

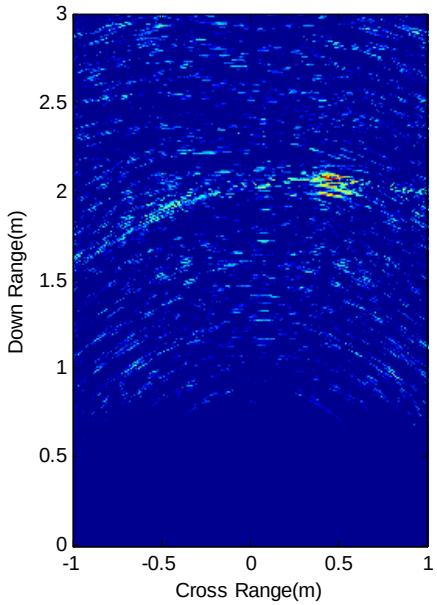

(5) N = 12, L= 180 cm, d= 15 cm

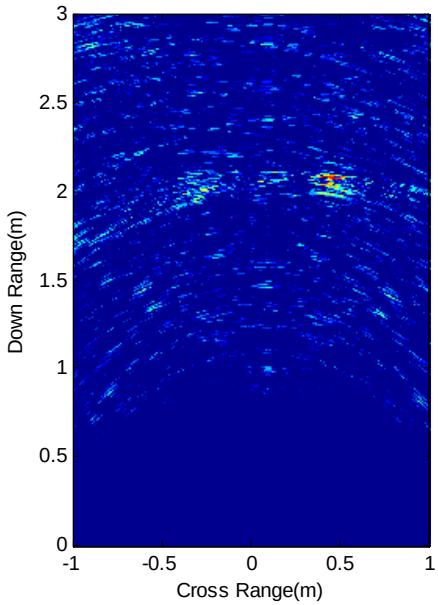

(6) N = 10, L= 180 cm, d= 18 cm

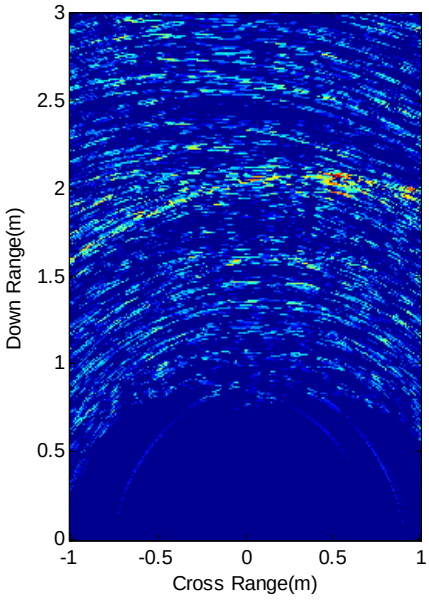

(7) N = 6, L= 180 cm, d= 30 cm

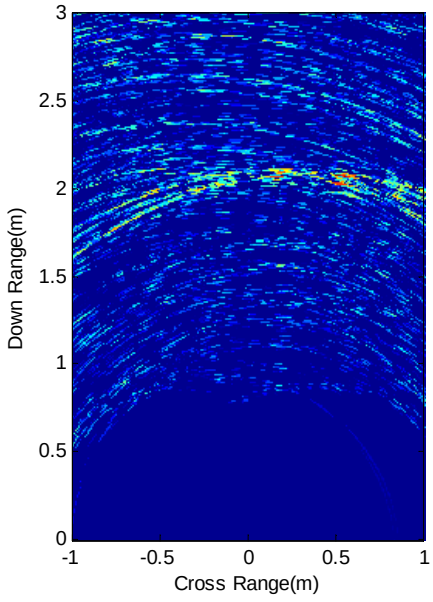

(8) N = 5, L= 180 cm, d= 36 cm

Figure 3.12: Continued.

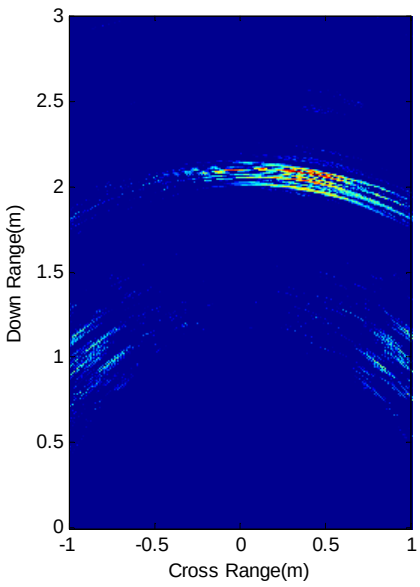

(1) *N*=15, *L*= 45 cm, *d*= 3 cm

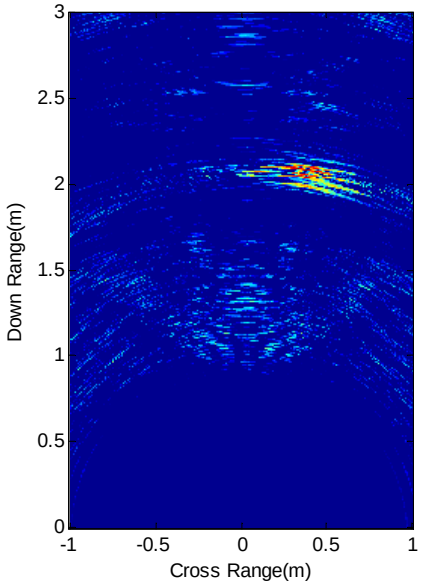

(2) *N*= 15, *L*= 90 cm, *d*= 6 cm

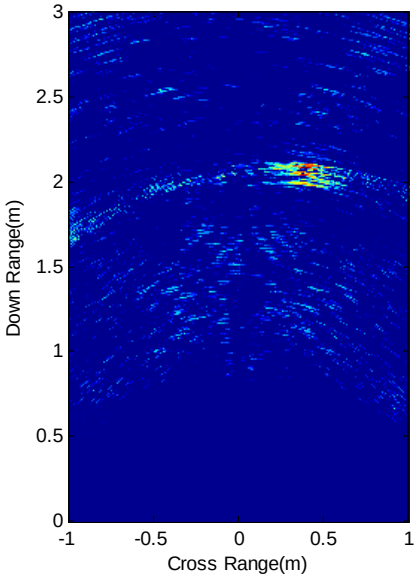

(3) *N*=15, *L*= 135 cm, *d*= 9 cm

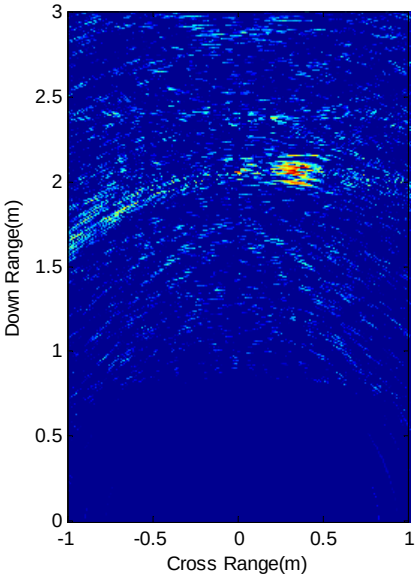

(4) *N*=15, *L*= 180 cm, *d*= 12 cm

Figure 3.13: Images Generated with Various Aperture Size and Fixed Number of Elements N.

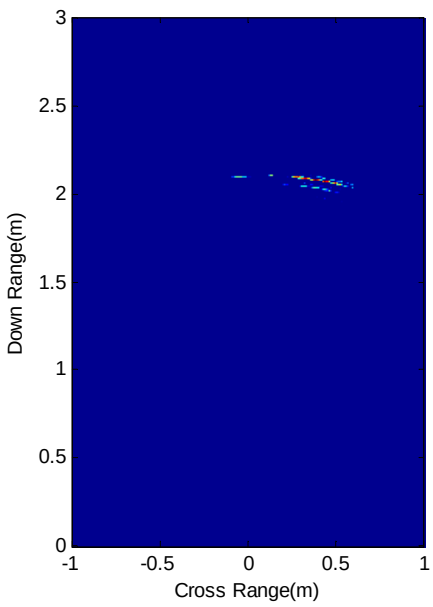

(1) *N*=15, *L*= 45 cm, *d*= 3 cm

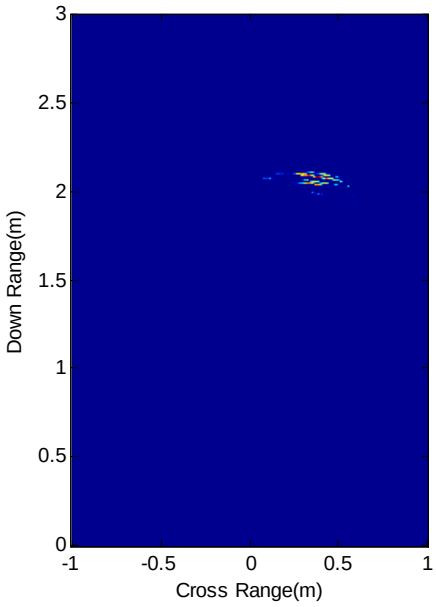

(2) *N*= 15, *L*= 90 cm, *d*= 6 cm

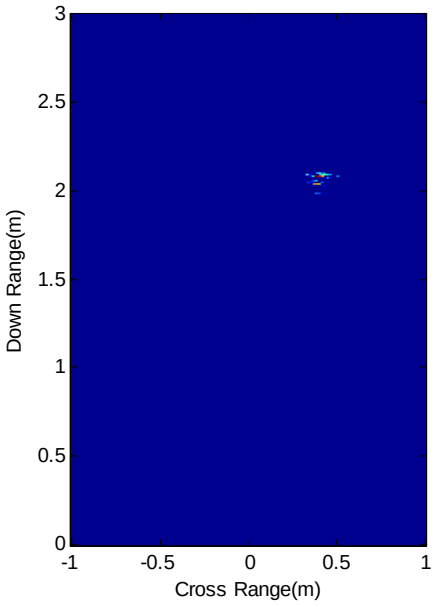

(3) *N*=15, *L*= 135 cm, *d*= 9 cm

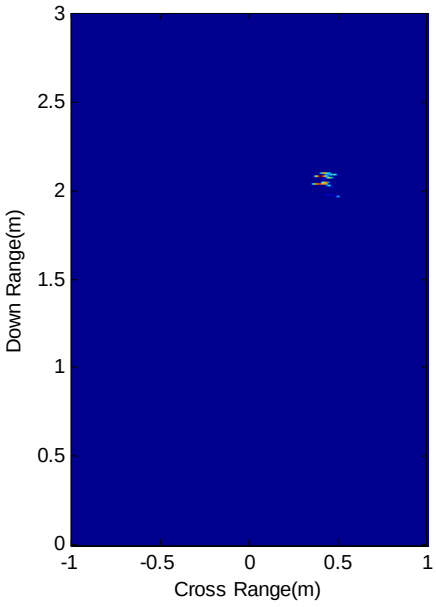

(4) *N*=15, *L*= 180 cm, *d*= 12 cm

Figure 3.14: Peak Detection for Fig. 7.12.

.

C. Effect of Carrier Frequency

Based on SAR theory, using a higher carrier frequency should provide a better cross-range resolution. Figure 3.15 displays the Sum-and-Delay formation results of two cubic boxes while the pulse is centered at 1 GHz, 2 GHz, and 4 GHz. Obviously, the higher carrier frequency generates more focused image, particularly in cross-range.

D. Effect of Wall on Image

The following discussion processes the receiver data as if the wall does not exist. The resulted image is defocused from its true position. A transmission and reflection measurements of the pulse propagating through the wall layer is done and shown in Figure 3.16. The transmitter and receiver are 0.5 m away from each other, and a 10-cm thick uniform wall is placed between them. The calculations have been carried out for discrete set of dielectric constants in the range of 1 to 9 and in steps of 2. Figure 3.17 displays the transmitted pulse recorded by the Receiver 2. The traveling distance between the transmitter and Receiver 2 is increasing upon increasing the dielectric constant from 1 to 9. The transmitted pulse too is further delayed and distorted. Figure 3.18 displays the reflected signal from the wall, which is recorded by Receiver 1. The separation between the first and second reflected responses (shown in red in Fig. 3.17b) corresponding to the round-trip electrical length of the wall thickness. For a fixed physical wall thickness of a 10 cm, the round-trip pulse traveling a distance in the wall layer, as expected, is increasing with the increase in the wall's dielectric constant.

Previous figures demonstrate the signal itself travelling through a wall slab. Now two conducting cubic boxes are placed inside a room, one with a 10 cm length and the other is 20 cm, as indicated in Figure 3.19. The generated image of the two targets is shown in Figure 3.20. With the increasing dielectric constant, the images of targets are displaced farther and farther from their true locations. Due to the higher reflections in this case from the wall and the less signal levels reflected back from the targets, strong side lobes occur for high dielectric constants ~ 8, and the image of the 10-cm cube is barely detectable.

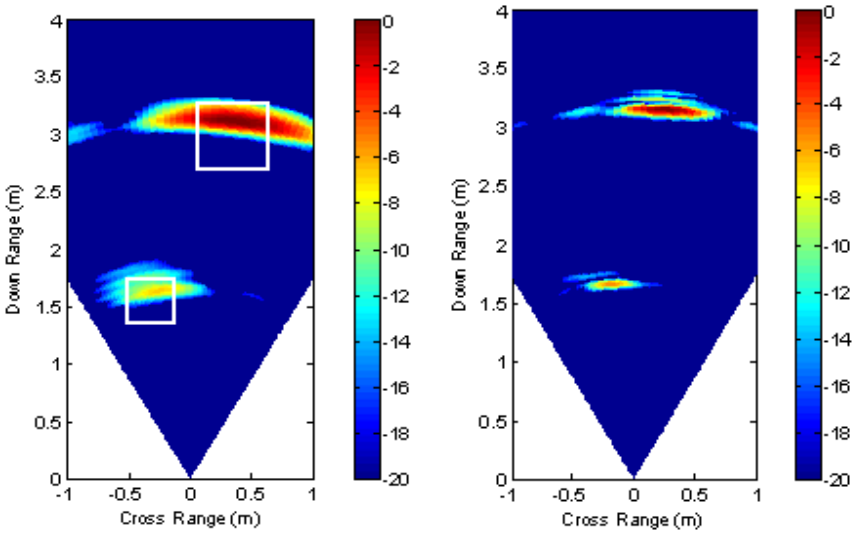

(a) 1 GHz Center **(b) 2 GHz Center**

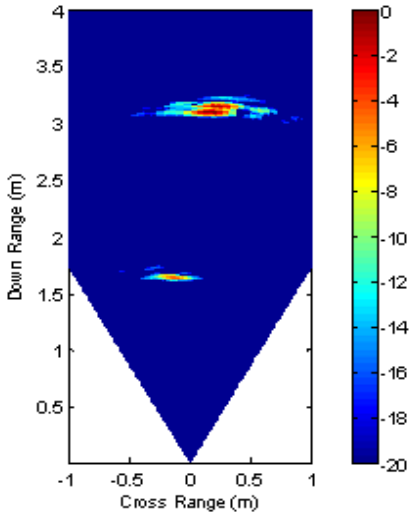

(c) 4 GHz Center

Figure 3.15: Images Generated by Using Different Carrier Frequency.

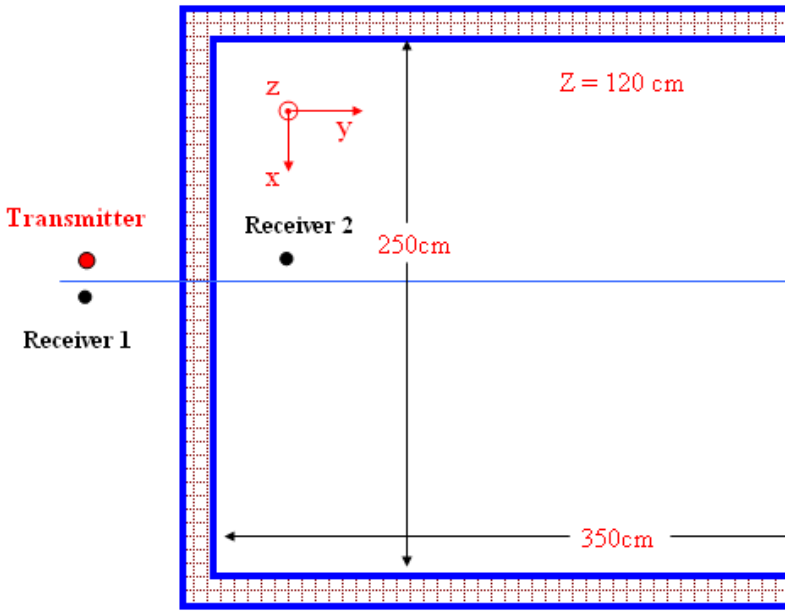

Figure 3.16: Transmission and Reflection Measurement.

.

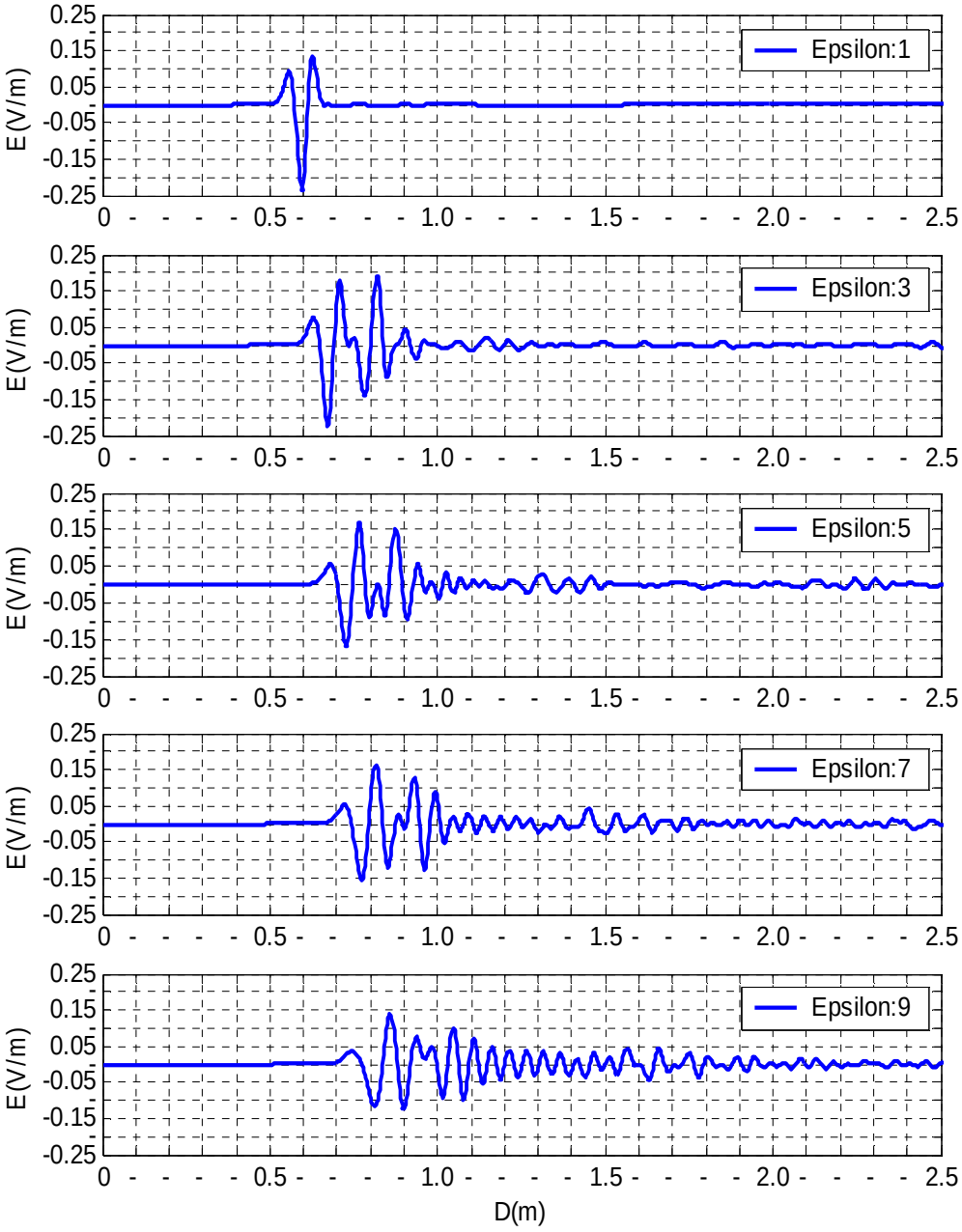

Figure 3.17: Transmitted Pulse through Wall.

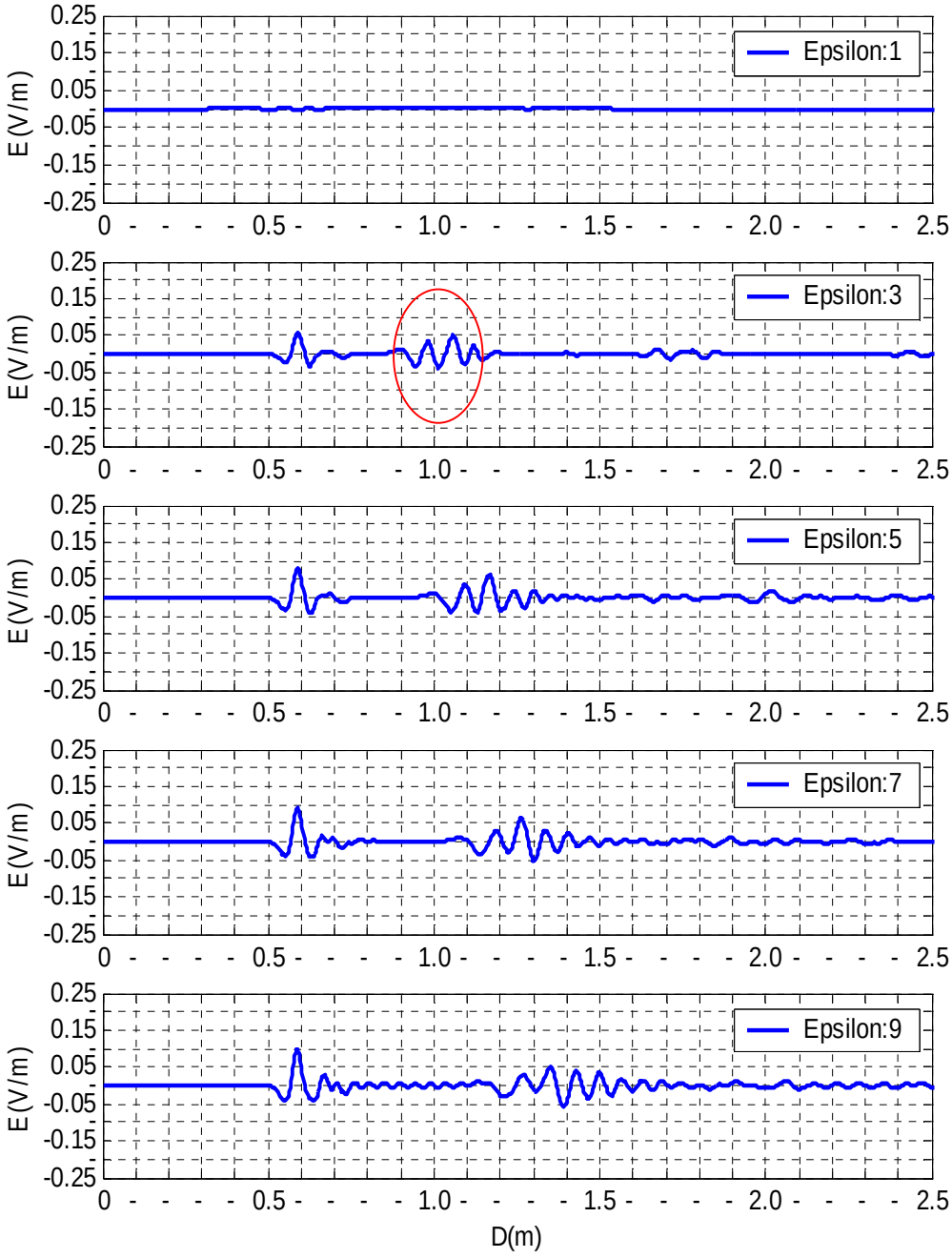

Figure 3.18: Reflected Pulse from Wall.

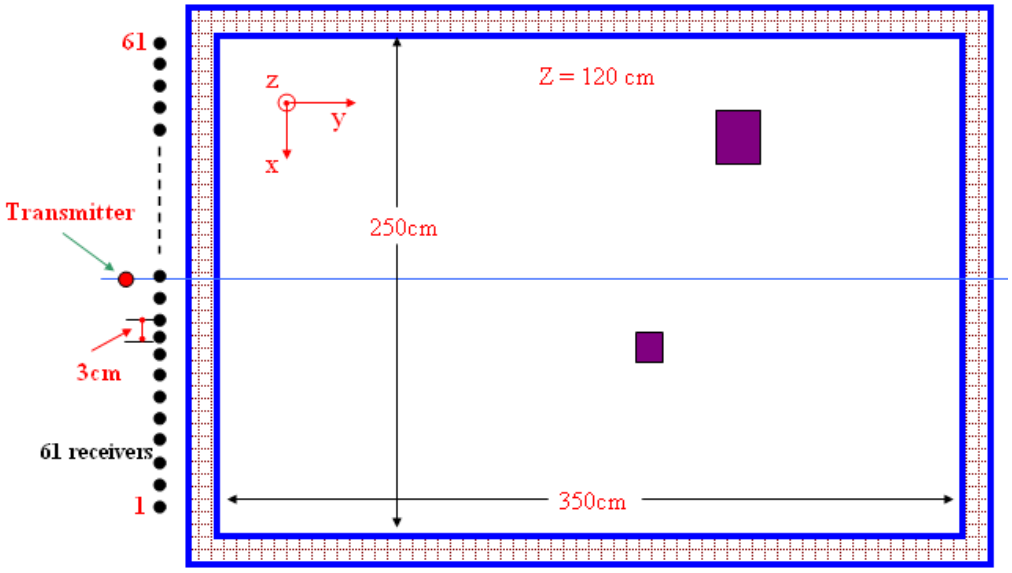

Figure 3.19: Two Targets inside Room.

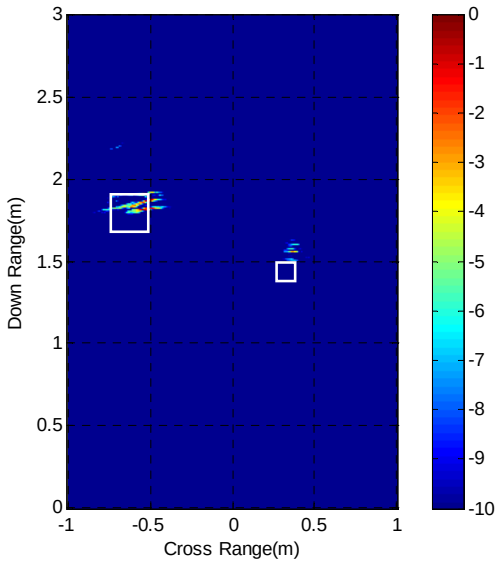

(1) Wall Dielectric Constant: 2.4

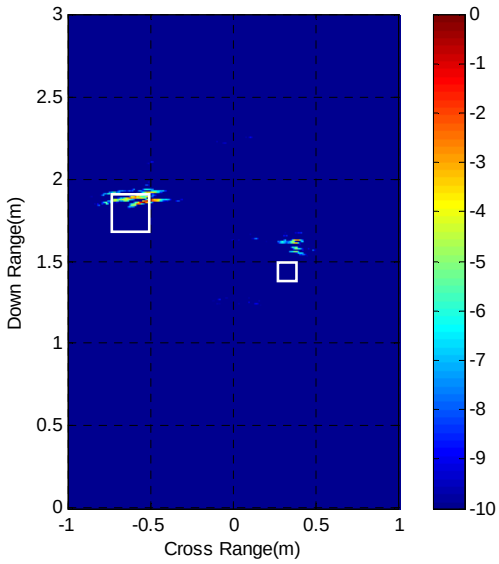

(2) Wall Dielectric Constant: 4

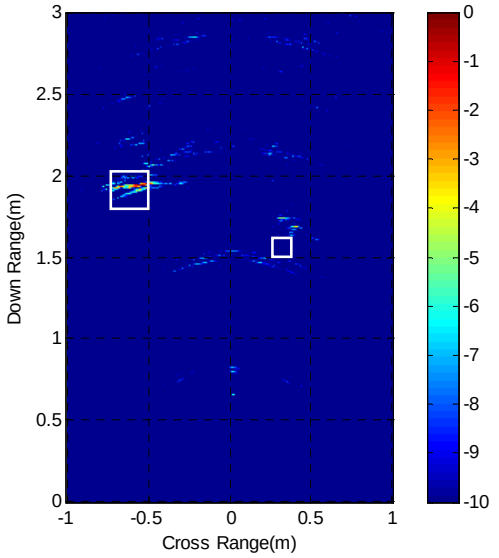

(3) Wall Dielectric Constant: 6

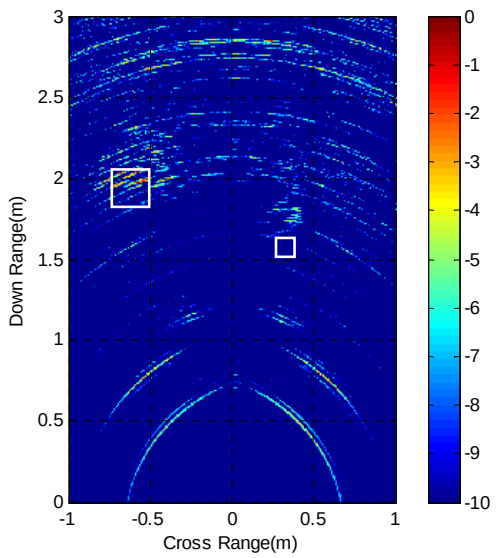

(4) Wall Dielectric Constant: 8

Figure 3.20: Gated Images of Two Targets inside Room.

The results shown in Figure 3.20 clearly indicate that the presence wall will cause significantly defocusing image. However, the methods described Section 3.1(C) can be employed to correct the defocusing effect, if the wall information such as thickness and dielectric constant is known. The algorithm is developed in Matlab, and applied to simulation data. In the simulation, a concrete wall of $\varepsilon_r = 7$ and 20cm thickness is placed 1.5m in front of the transmitter and receiver locations. A 12cm-square metal sheet is placed 3.4m in front of the transmitter and receiver. One transmitter and sixteen receiver is uniformly distributed along the center of the cross rage, and the receiver spacing is 2.4cm. The CFDTD pulse source is with 1 GHz bandwidth and centered at 5 GHz. Figure 3.21(c) illustrates the conventional Backprojection image, which reveals the defocused/delayed position of the wall and target. Figure 3.21(a) zooms into the small region around the target and it shows the target's position is at 3.7m and offset from its true position at 3.4m, due to the concrete wall slowing down the signal speed. Applying the correction algorithm on this small region, the offset is being illuminated and the resulted image shows the real location of the target at 3.4m.

Based on the previous simulation analysis, several conclusions can be drawn. First of all, the conventional SAR theory is still valid to a great extent, and can be applied to STW applications. For example, in a STW scenario the effect of array configuration, in terms of the receiver number and the element spacing follow the same rule as that for the conventional SAR radars; for example increasing the operating frequency will result in higher range resolution as well. However, one unique constraints of the STW implementation is its very limited options for array configuration, and will make it harder for direct implementation of many conventional SAR algorithms for STW. For example, Algorithms based on domain integral equations [28] model targets and media as grids of permittivity while they assume that antenna scans around target, which is not realistic for implementation into See-Through-Wall application. High-resolution diffraction tomography method [29]-[31] also requires scanning the antenna around the target.

Secondly, the correction of the wall effect remains a great challenge for a high-resolution STW imaging. STW may require high resolution better than 10 cm, so that it can discriminate between a combatant/bystander and even possibly identify side arms or larger weapons. The defocusing of images due to the wall effect needs to be compensated to acquire such a high resolution. Although some progress has been reported and the correction issue [18]-[20], the reported method only solves a simplified model based on time-consuming iterative method.

Thirdly, a practical system has to implement a multiple imaging schemes to take advantage of different imaging methods. As a real-time operation, STW system further requires the imaging algorithm to be fast and stable, which is a condition usually conflicts with high resolution imaging. With a multiple imaging schemes implemented in a system, a fast but low-resolution algorithm can be used to scan a large scene and to provide coarse target information, and then only a relatively small area is zoomed-on, and the target will be fine processed for high resolution. For experimental purpose, two classical UWB SAR imaging algorithms, Sum-and-Delay and Back-projection [40], have been

implemented for my system. The time-domain Sum-and-Delay method will do fast scanning over a large room area, while the Back-projection method will be used to process a zoomed-in smaller area.

Finally, parallel computational resource is desired for an efficient STW modeling. Results have shown that FDTD is a good procedure for UWB STW analysis, but this technique is very computational intensive. For example, modeling the 3.5m x 2.5m x 2.4m room with a 1 cm cubic cell in a CFDTD, requires on the order of 4 Gbytes RAM and 40 CPU hours. This problem can be overcome by using the ECE Flux cluster of 24 computer nodes, which is configured to run parallel CFDTD software and dramatically reduces the computational time.

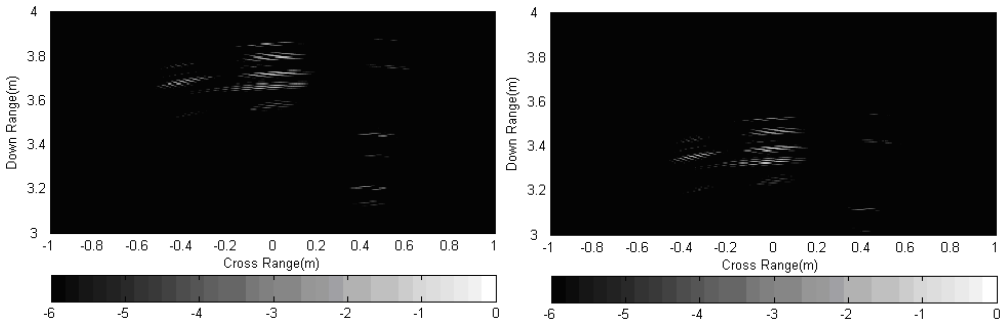

(a)Before Wall Correction (b)After Wall Correction

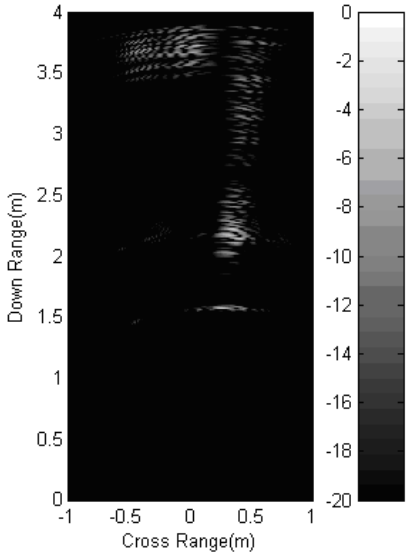

(c) Backprojection View

Figure 3.21: 12cm Metal Panel, 3.4m away from radar, through 20cm-thick concrete wall.

Chapter 4 . WALL CHARACTERIZATION AND FREQUENCY SELECTION

The propagation characteristics of UWB signals are essential for the optimal design and implementation of STW systems. In this chapter the loss mechanisms of various types of walls is evaluated as a function of frequency. The objective is to examine propagation through walls made of typical buildings materials and experimentally acquire UWB characterization of these materials. Along with the simulation, the experimental data will provide useful insight regarding the operating frequency selection and advanced wall correction method when designing a practical system. Several types of walls will be investigated including drywalls, brick-walls, woods, and concrete-walls, which are typically encountered in a building.

4.1. Fundamentals of EM Propagation

In the analysis of harmonic time dependence, one uses the conductivity σ in S/m of the medium or equivalently uses the complex dielectric constant ε_r having a positive real part and a negative imaginary part, $\varepsilon_r = \varepsilon_r^{'} - j\varepsilon_r^{''}$ where $\varepsilon_r^{''} / \varepsilon_r^{'} = \tan\delta$. Measurement of ε_r has been previously reported of many wall materials, Table 5, It is important to know here, however, that these reported, [52],[53], and measured values are only nominal values as many of these walls have complicated structures and made of many different materials or comprised of many layers. For example, bricks could be made out of different materials including air and glass could be metalized. Additionally, humidity can play an important role in changing their electric characteristics given that water has a very high dielectric constant. It is expected that dried bricks for example would have lower dielectric constant and significantly lower loss factor compared when it is wet. Additionally, these materials could have frequency-dependent complex dielectric parameters, hence reported values is given as measured at a specified frequency and environment conditions.

Table 5: Material Characteristics.

Material	$\varepsilon_r^{'}$	**σ S/m**	**tan δ**
Glass	3.8-8		$<3\text{x}10^{-3}$ @ 3 GHz
Wood	1.5-2.1		<0.07 @ 3 GHz
Gypsum board	2.8		0.046 @ 60 GHz
Chip board	2.9		0.16 @ 60 GHz
Dry brick	4		0.05-0.1 @ 4.3 GHz
Dry concrete	4-6		0.1-0.3 @ 3, 60 GHz
Aerated concrete	2-3		0.1-0.5 @ 3, 60 GHz
Limestone	7.5	0.03	
Marble	11.6		0.078 @ 60 GHz
Ground	7-30	0.001-0.003	
Fresh water	81	0.01	
Seawater	81	4	

To investigate the loss mechanism from EM point of view, we will assume plane wave propagation in the far field of EM radiation, and let us assume that when a plane wave propagating in air it encounters a boundary with a different dielectric constant, therefore part of it will be reflected and part of it will be transmitted. The reflection and transmission coefficients are generally function of the incident plane wave incident angles and polarizations. Table 6 summarizes the reflection and transmission coefficients as a function of the incident angle. Reflection coefficients are generally higher for higher dielectric constants and that of TE are generally higher than TM for oblique incidence. When a wall structure of multiple dielectric layers is encountered, faces of the walls are parallel to each other and can be approximated as multi-dielectric layers. The reflection and transmission coefficients through the whole structure can be calculated using the transmission line approach. The reflection and transmission coefficients are listed in Table 6. The expressions in Table 6 and Table 7 are valid also for walls with losses where the propagation constant becomes complex. These coefficients are function of frequency and some frequencies can pass through the wall with relatively low reflections which is important observation for UWB applications. One advantage of using UWB signal to see through wall (except in a very lossy media) is that there is always a fraction of the spectrum that would penetrate through the building well enough that allows: post-processing to recover the image behind the walls, estimate wall materials, and correct image defocusing. However, due to the complexity of these analytical expressions, it is very difficult, if not impossible, to use the reflection or transmission coefficient in a closed analytical form for STW.

Table 6: TE/TM Coefficient at a Dielectric Interface.

	reflection	transmission
TE	$\Gamma_{TE} = \frac{Z_d^{TE} - Z^{TE}}{Z_d^{TE} + Z^{TE}} = \frac{\cos\theta - \sqrt{\varepsilon_r}\cos\theta_T}{\cos\theta + \sqrt{\varepsilon_r}\cos\theta_T}$	$T_{TE} = 1 + \Gamma_{TE} = \frac{2\cos\theta}{\cos\theta + \sqrt{\varepsilon_r}\cos\theta_T}$
TM	$\Gamma_{TM} = \frac{Z_d^{TM} - Z^{TM}}{Z_d^{TM} + Z^{TM}} = \frac{\sqrt{\varepsilon_r}\cos\theta - \cos\theta_T}{\sqrt{\varepsilon_r}\cos\theta + \cos\theta_T}$	$T_{TM} = 1 + \Gamma_{TM} = \frac{2\sqrt{\varepsilon_r}\cos\theta}{\sqrt{\varepsilon_r}\cos\theta + \cos\theta_T}$
Where $\cos\theta_T = \sqrt{1 - (\sin\theta / \sqrt{\varepsilon_r})^2}$		

Table 7: TE/TM Coefficient through Dielectric Layer

	reflection	transmission
TE	$Z_{in} = Z_w \dfrac{Z_L \cos\beta_w w + jZ_w \sin\beta_w w}{Z_w \cos\beta_w w + jZ_L \sin\beta_w w}$ $Z_w = \dfrac{\sqrt{\mu_0/\varepsilon_0}}{\cos\theta_T} = \dfrac{\sqrt{\mu/\varepsilon}}{\sqrt{\varepsilon_r - \sin^2\theta}}$	$T_{TE} = 1 + Z_{in}$
TM	$Z_{in} = Z_w \dfrac{Z_L \cos\beta_w w + jZ_w \sin\beta_w w}{Z_w \cos\beta_w w + jZ_L \sin\beta_w w}$ $Z_w = \sqrt{\mu/\varepsilon}\cos\theta_T = \sqrt{\mu_0/\varepsilon_0}\dfrac{\sqrt{\varepsilon_r - \sin^2\theta}}{\varepsilon_r}$	$T_{TE} = 1 + Z_{in}$
Where $\cos\theta_T = \sqrt{1-\left(\sin\theta/\sqrt{\varepsilon_r}\right)^2}$, Z_L is that for Air		

4.2. Experiment and Modeling of Wall Characterization

The characterization method adapted here is based on measuring an insertion transfer function, defined as the ratio of two signals measured in the presence and in the absence of the material under test. The insertion transfer function can be obtained either through frequency-domain measurements using a vector network analyzer, or by performing time-domain measurements using a pulse generator and a sampling oscilloscope and then Fourier transforming the measured signals into the frequency domain. Here, the frequency-domain technique is used to attain the measurement data.

The experimental setup to evaluate the transmission through the walls is indicated in Figure 4.1. The transmitting and receiving antennas are positioned on a line of sight, and the transmission coefficients are measured with and without the presence of these wall slabs that are presumed to be located between these transmitting and receiving antennas. The insertion function is attained by normalizing the transmission coefficient with walls in comparison to that without walls. In general, the horn radiation pattern must be taken into account for large angular displacements. However, for narrower incident angles (i.e. slightly off-the horn broadside radiation) the effect of the radiation pattern is only few decibels.

HP8510C network analyzer and two identical standard horns are used. The two antennas are connected to port 1 and port 2 of the vector network analyzer and separated by 10m. Both the input return and transmission coefficients are recorded as a function of frequency, i.e. S11 and S21. For a high accuracy, the locations of the transmitter and receiver are fixed and the walls are mounted on a moveable platform. In this setup, the incident waves are assumed to be TEM waves and have normal incidence conditions. The

loss through a wall is calculated from normalizing the insertion loss "S21" measured when the wall is between the antennas, to the S21 without the wall in between (i.e. free space S21).

Figure 4.2 plots the RF attenuation for different types of walls, based on our measurements, in comparison to Currie, et al [52][53] . The results show that most walls, such as dry wall, plywood, and bricks are fairly transparent to radar frequencies, thus making through-the-wall imaging possible. But in reality, materials are often soaked with water, which will cause even relatively higher attenuation through the walls, and this additional loss must be taken into account [54]. If radar signal must penetrate concrete block, a practical operational frequency is about 3 GHz, otherwise the usable frequency range should not be greater than approximately 10 GHz. Various techniques to characterize wall materials for UWB STW and communication applications were addressed in [55]-[66].

The measured results were utilized to develop a transmission line equivalent circuit of wall for the normal incidence. The model has been developed in Advanced Design System (ADS) [x] and is shown in Figure 4.3. The wall slabs and free space paths were represented by transmission-lines components in ADS. The material properties, such as wall thickness and dielectric constant, can be adjusted accordingly. This model is to run frequency domain S parameter sweep and the previous real wall measurement can be replicated in ADS. Figure 4.4 shows the insertion loss versus frequency for drywall slabs with different wall thicknesses, where the measured results of insertion loss match the simulation very well.

The proposed model is simple and very sensitive to both the real and imaginary parts of the dielectric constants of the material, and has produced very good results. This method; however, is based on assuming non-dispersive material properties, i.e. constant complex dielectric constant within the operating frequency range. This assumption is generally accepted for materials such as wood, glass, dry-wall, and Styrofoam. Bricks and concrete walls are generally however, has a slight frequency dependence as their imaginary part (i.e. loss tangent parameters increase at higher operating frequencies), and other measurements methods should be considered. Hence, predicted results are an estimate of the average dielectric constant of the material within the operating frequency range.

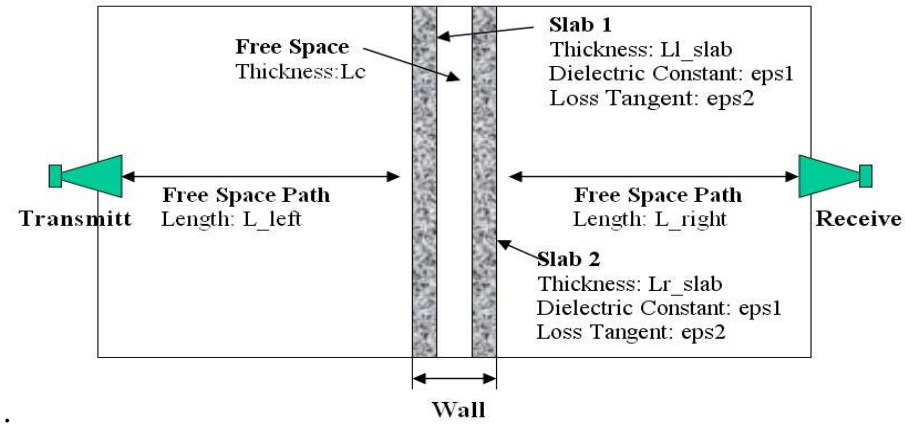

Figure 4.1: Loss Measurement Setup.

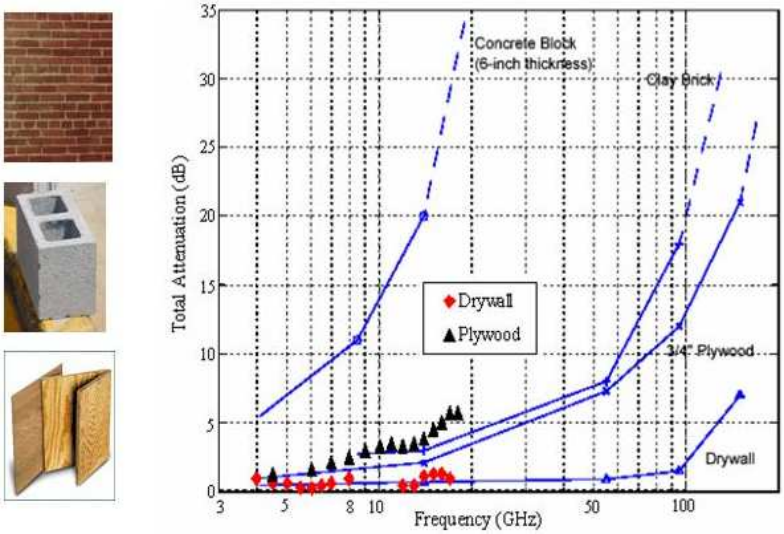

Figure 4.2: Attenuation of Different type of walls versus frequency.

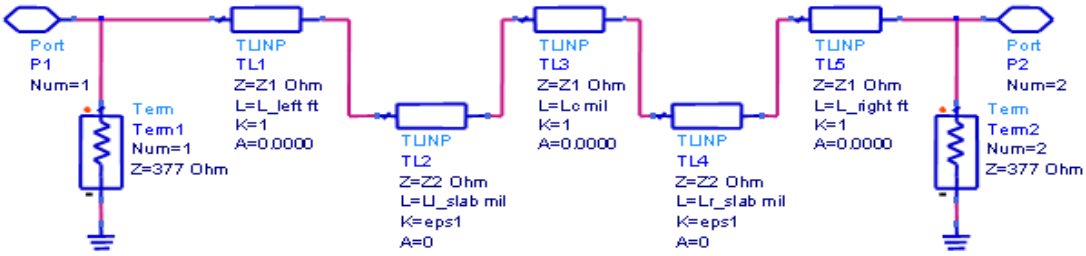

Figure 4.3: ADS Model.

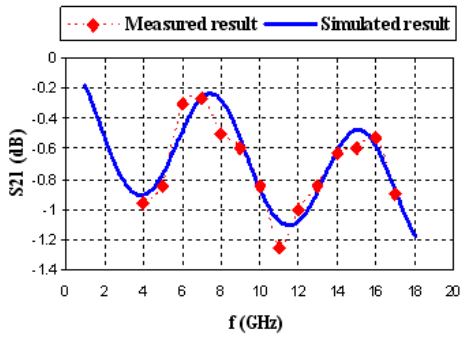

(a) 1/2 inch Slab

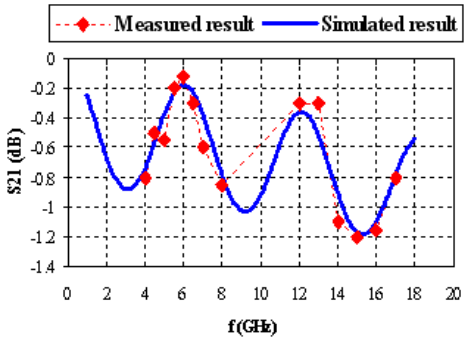

(b) 5/8 inch Slab

Figure 4.4: Insertion loss versus Frequency for a Drywall
(Dielectric Constant was predicted to be 2.4@10 GHz).

The addressed measurement and modeling provide valuable insight to the STW system implementation. First, UWB technology provides the flexibility of choosing the operating frequency over an extremely wide frequency range, below 900 MHz, or from 3.1 GHz to 10.6 GHz according to FCC definition. The attenuation/loss data in Figure 4.2 indicates that lower frequencies are generally preferred for their favorable propagation through materials (less attenuation and backscattering). On the other hand, radar technology prefers higher frequencies in order to achieve finer cross-range resolution. Hence, for a practical system implementation, a trade-off must be made among the operating frequency, the system power, and the designed radar resolution.

Secondly, the straight-forward ADS model can serve as an efficient and accurate tool to characterize various wall structures. Since the insertion loss and dispersion of the waves greatly depends on the wall type, the operating wavelength and bandwidth, a first step in developing STW imaging method, is to study the effect of wall on the transmitted UWB signal. In Chapter 3, FDTD-based computational method has been presented for STW EM simulation. However, it is time-consuming and requires huge computational resources. The proposed ADS model can do fast simulation while providing relatively accurate result.

When encountering a wall structure, initial values for the material parameters based on previously published results, summarized in Table 6, can be fed into the ADS model, the general return loss and transmission properties can be discovered, in terms of magnitude and phase over a wide frequency range. If starting from measurements on a complex multilayer wall structure, the model parameters, such as dielectric constant and loss tangent can be tuned and optimized until it matches the measurements, thus providing an estimate for the overall wall materials characteristics. This simple ADS model will help to take the wall effect into account, particularly when compensating the wall effect during imaging formation for both normal and oblique incidence.

It is important to recognize here that in real life scenarios, wall composition is not known. In other words, practically, it would be difficult or even impossible to measure transmission coefficient. Additionally, there is no way to identify the wall thickness or the layer compositions. It is a challenge nowadays for STW technology to develop efficient algorithms to estimate the wall physical parameters based on reflection measurements only. This could be in either frequency or time domain. This is typically an inverse scattering problem from an EM point of view.

Chapter 5 . ULTRA WIDEBAND VIVALDI ANTENNA ARRAY

Compared to conventional narrow band systems, it is challenging to design an antenna for UWB systems since one must consider the trade-offs of wide bandwidth, good input match, small size, minimal dispersion, and low cost. A number of UWB antennas and some of their characteristics are summarized in Table 8. This list illustrates some of the most common designs and limits of their operation. On this list, spiral antennas are dispersive in nature, and therefore not suitable for short pulse applications. Patch antenna normally has small bandwidth; however, its bandwidth can be extended by stacking multiple resonant sections of different dimension, at the expense of complexity in its design and fabrication. Meanwhile, TEM and Bow-Tie antennas have the required EM characteristics of an UWB application, but their large sizes make it difficult to use them in a practically portable system or an array system.

For a STW application, the transmitting and receiving antennas must be compact and lightweight for portability. Besides the requirements on their physical size, the antenna must be able to transmit UWB pulses with minimal distortion. The antenna's radiation pattern needs to be accounted for also since significant image distortion might be seen due to the radiation pattern angle dependence. One novel design of UWB patch, Vivaldi antenna has been reported to be used for STW application, because of its favorable characteristics: simple structure, light weight, wideband, high efficiency, and high gain characteristics. Theoretical and experimental analysis of Vivaldi antenna characteristics can be found in [67]-[77].

This chapter will discuss the development of a Vivaldi antenna array for STW [67]. In this design Antipodal Vivaldi antenna element and Wilkinson power divider are used to achieve a bandwidth from 8 to 12 GHz. The main advantage of this element over regular Vivaldi antenna element is that very wideband performance can be achieved using the antipodal tapered slot with its inherently simple wideband transition from microstrip line to parallel-strips.

Table 8: Antenna Characteristics

Type	**Bandwidth**	**Polarization**	**Size**
Patch	Large	Linear/Circular	Small
Slot	Medium	Linear	Small
Spiral	Large	Circular	Small
TEM	Wide	Linear	Large
Bow-Tie	Wide	Linear	Small

5.1. Design of Antipodal Vivaldi Element

The array design starts from a single Antipodal Vivaldi element, shown in Figure 5.1. For Vivaldi antenna, the exponential tapered profile is a common shape to obtain wideband 10dB impedance. The exponential taper profile is defined by the opening rate R and the two points $P_1(x_1, y_1)$ and $P_2(x_2, y_2)$ (use the first and the last points of the exponential taper)

$$y = c_1 e^{Rx} + c_2 \qquad \textbf{(5.1)}$$

where

$$c_1 = \frac{y_2 - y_1}{e^{Rx_2} - e^{Rx_1}}, c_2 = \frac{y_1 e^{Rx_2} - y_2 e^{Rx_1}}{e^{Rx_2} - e^{Rx_1}} \qquad \textbf{(5.2)}$$

Given the highest frequency of operation (f_H), the width W of the tapered slot antenna should satisfy equation (5.3) to circumvent the grating lobes of Vivaldi array.

$$W < \frac{c}{f_H \sqrt{\varepsilon_e}} \qquad \textbf{(5.3)}$$

where ε_e is the effective relative dielectric constant. In addition, the antenna is fed by a microstrip through a stripline transition as shown in Figure 5.1. The element will be fabricated on Rogers 20-mil Roger 4003C material with a relative dielectric constant of 3.4. It is optimized in Ansoft High Frequency Structure Simulator (HFSS) tool to achieve both the compact size and good performance at the operating frequency band from 8-12 GHz. The dimensions indicated in Figure 5.1 are from the optimization results. The simulated far field radiation patterns of this element at a center frequency of a 10 GHz are illustrated in Figure 5.2. The element has ~ a 70^0 , 3-dB beamwidth and a 5-dB gain.

5.2. Design of the Vivaldi Subarray

Sixteen antipodal elements are combined through a Wilkinson power divider to form a subarray. A 3-section Wilkinson divider is chosen to compose the 16-way binary divider tree, which provides equal amplitude and phase signals over the 8-12 GHz bandwidth. A 1 to 4 Wilkinson divider was built to experimentally test the performance, shown in Figure 5.3: 1 to 4 Wilkinson Divider. The predicted transmission and reflection performance of the 4-way divider is shown in Figure 5.4: Divider Characterization(a). Insertion loss of each path is about 7dB with ±1dB fluctuation. Reflection at Port 1 is better than –10dB from 2 to 14 GHz, shown in Figure 5.4: Divider Characterization(b). Indicated in Figure 5.4: Divider Characterization(c), the worst-case relative phase imbalance is of 10^o degrees from 2 to 14GHz. The return loss of each port is below -10dB from 2 to 14GHz, and both are in excellent agreement with the predicted results. Measured results of other ports are not plotted out and they follow the same pattern as S21 and S11.

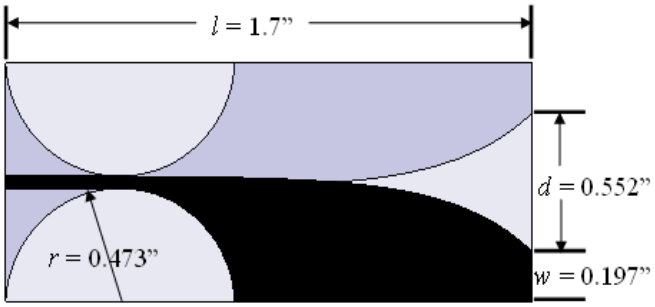

Figure 5.1: Designed Antipodal Vivaldi Antenna.

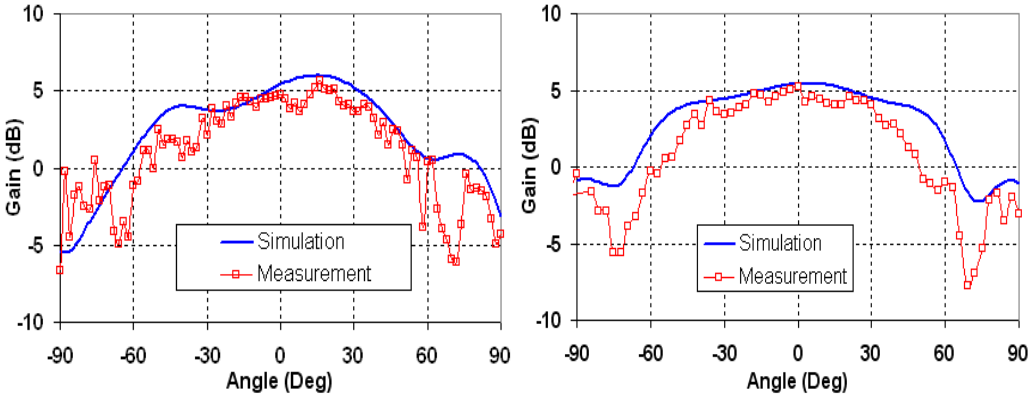

(a)E-plane (b) H-plane

Figure 5.2: Pattern of Single Element at 10 GHz.

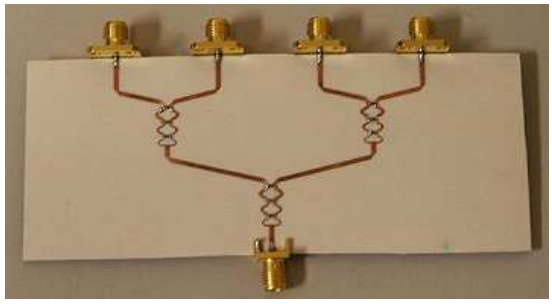

Figure 5.3: 1 to 4 Wilkinson Divider.

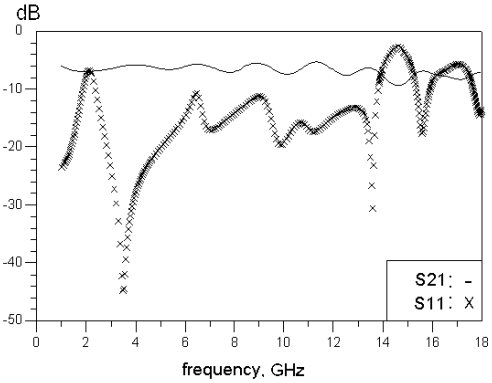

(a)Simulated Return loss and Transmission

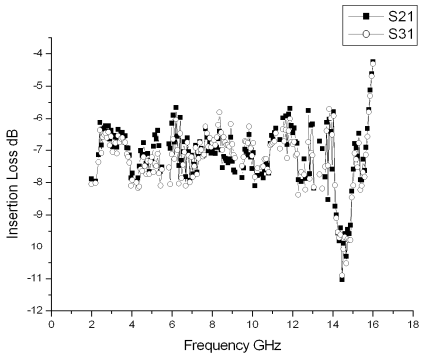

(b) Measured Insertion Loss

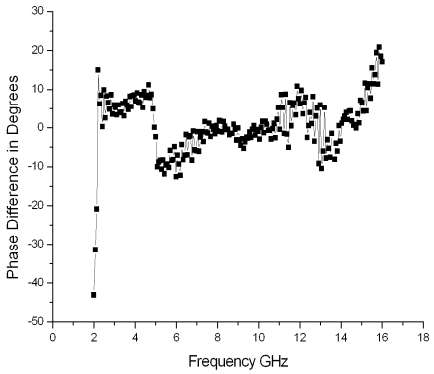

(c) Measured Phase Response

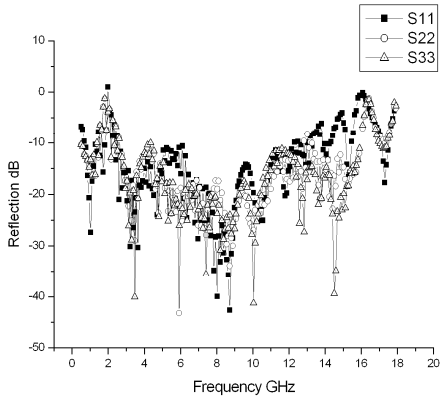

(d) Reflection of 4-way Wilkinson Array

Figure 5.4: Divider Characterization.

The top and bottom layers of the fabricated 16-element subarray are shown in Figure 5.5. The element spacing is equal to the width of an element, which is ($d+2w$) = 0.946" (24mm). To ensure no grating lobe, the following condition should be satisfied [78],

$$(d+2w) < \frac{\lambda}{1+|\cos\phi_0|} \qquad \textbf{(5.4)}$$

Where ($d+2w$) is the element spacing, λ is the wavelength at operating frequency, and ϕ_0 is the steering angle. At broadside, ϕ_0 = -90 degree, this reduces the earlier condition ($d+2w$)< λ. At endfire, ϕ_0 = 0 degree or 180 degree, it reduces to $d < \lambda/2$. This subarray has $\phi_0 = 90^0$ and is slightly smaller than λ_0 at 12 GHz, which predicts a grating lobe at the upper band of the operating frequency and should not be used at frequencies beyond 12 GHz to avoid grating lobes, however, higher sidelobe levels are expected at 12 GHz and above. The main beamwidth of an array is given by the following formula [78],

$$\Delta\phi_{3dB} = \frac{0.886}{\sin\phi_0}\frac{\lambda}{Nd} \qquad \textbf{(5.5)}$$

which predicts that around 10 GHz this subarray has a 4 degree 3-dB-beamwidth in the E-plane.

Radiation pattern of the 16x1 array are measured. Figure 5.6 shows that the array pattern is almost constant within the operating frequency range. The 3-dB beamwidth is about 4° in E plane and 70° in H plane. At 12 GHz, side lobes occur at 80^0, which is due to array element spacing. The measured gain varies from 13 dB to 14 dB, where about 3dB gain drop are related to the long feed-line of the 1:16 distribution network. The closest visible sidelobe occurs at 80^0 at 12 GHz in the E plane; and the 3-dB beamwidth is about 4° in the E-plane and 70° in the H-plane. The measured results match the theoretical values predicted by Eq.(5.4) and (5.5).

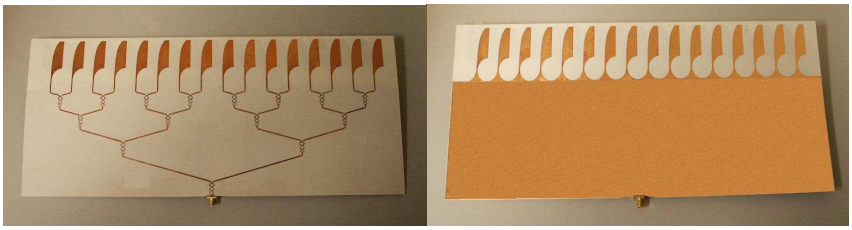

Figure 5.5: Top and Bottom views of 1x16 Vivaldi Array (7″ x 16″).

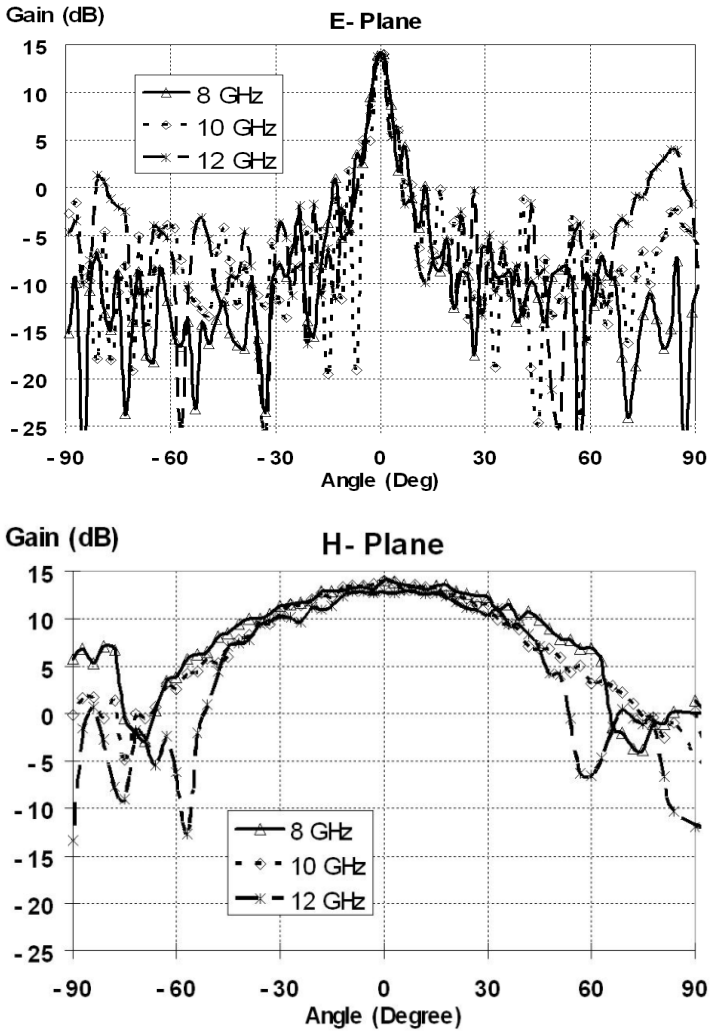

Figure 5.6: Measured Subarray Pattern.

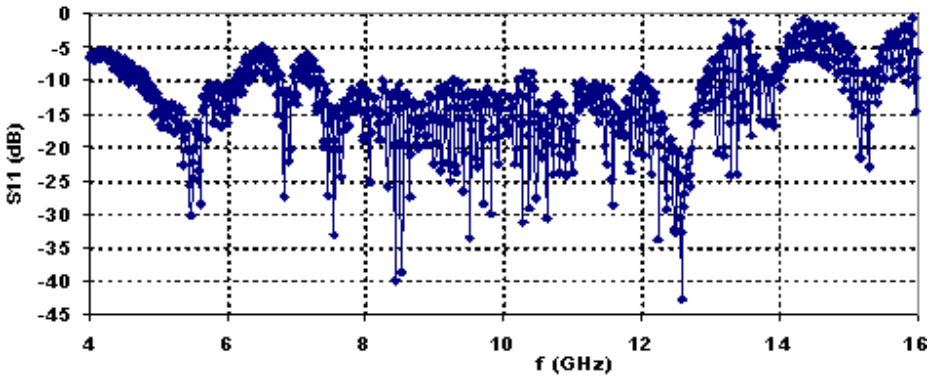

Figure 5.7: Measured Subarray Return Loss

5.3. Design of a Full Array

A full array with sixteen 16-element sub-arrays was built for 8-12 GHz operation and is shown in

Figure 5.8. This full array has a fixed elevation beam pattern (E plane) shown in Figure 5.6(a), and can be synthetically steered in the azimuth plane (H plane). The sub-array spacing is set to 2.4 cm, which is 0.8λ at 10 GHz for suppressing grating lobes over the scanning angle from -30^{o} to 30^{o}. The synthesized azimuth (H plane) 3-dB main beamwidth is around 40^{o} at broadside, according to Eq.(5.4). Because of the presence of $\sin\phi_0$ in the denominator, the beamwidth will get broader as the array is synthetically steered from broadside to near endfire. For a fixed operating frequency range, one can either increase the inter-element spacing d or the number of array elements N to decrease the main beamwidth and improve the array directivity. However, increasing N will make the array larger and more complicated to fabricate; increasing d will cause grating lobes and would limit the viewing angle. Depending on different applications requirements, a trade-off must be made between the array performance such as the main beamwidth and steering range, and the array design degrees of freedom such as the inter-element spacing and the number of elements.

A Single Pole 16 Throw (SP16T) switch, Figure 5.10, is designed to automate the SAR operation. The SP16T switch is comprised of 15 Single Pole Double Throw (SPDT) switch units, utilizing a binary tree structure Figure 5.9. The used SPDT MMIC unit is Hittite HMC347LP3 [79], with a 1.7 dB insertion loss, 40-dB isolation, and have a DC – 14GHz operating range. The MMIC board is made of 0.0508cm Roger 4003C substrate and placed in a customized aluminum housing package. The switch driver is comprised of 74HC04 chips and utilizes a 4:16 decoder topology. A 4-bit TTL word provides 16 logic states, from "0000" to "1111", each of which turns on the corresponding channel. By feeding 4-bit TTL signal to the driver, the chosen sub-array will be turned on. More details of the driver circuit design can be found in [79].

The simulation/measurement return and insertion losses results of the SP16T switch are demonstrated in Figure 5.11 The return loss is better than 12 dB within the 8-12 GHz operating band. The typical insertion loss is 8 dB and with less than ± 1 dB fluctuation for all the 16 paths (only results for one channel are plotted as example). This switch, however, has considerable high insertion loss of 8 dB, due to the high loss of its individual SPDT units. Considerable performance improvement and structure complexity reduction can be achieved upon utilizing the recently available SP4T switch HMC344. The simulation shown in Figure 5.11 predicts at least 2 dB less insertion upon using the new SP4T units.

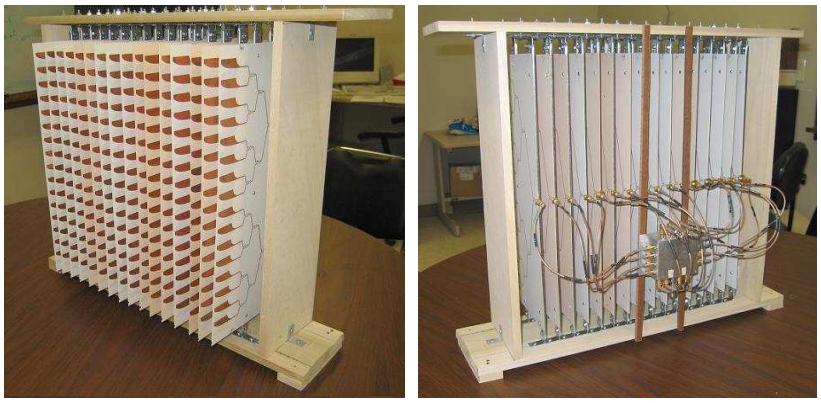

Figure 5.8: Full Array with SP16T Switch.

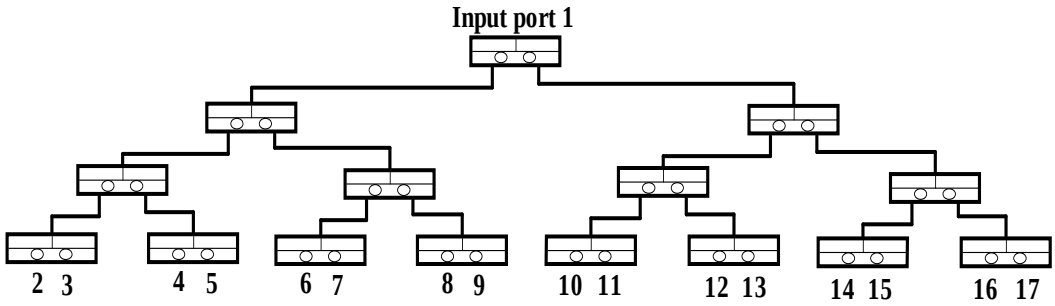

Figure 5.9: SP16T Binary Tree.

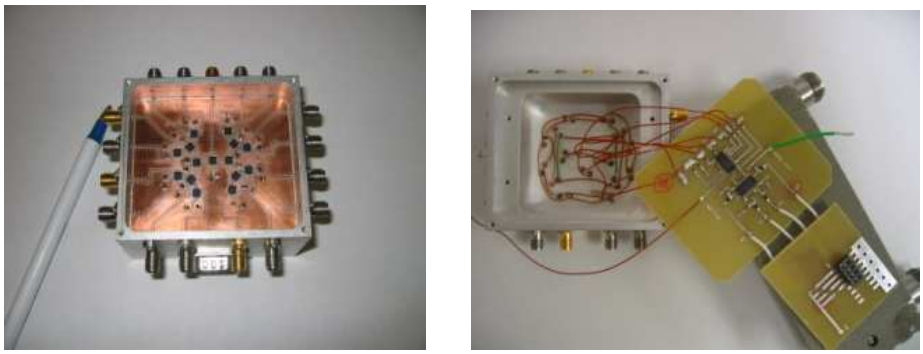

(a) MMIC Board and Housing Package (b) Driver Circuit

Figure 5.10: SP16T Switch.

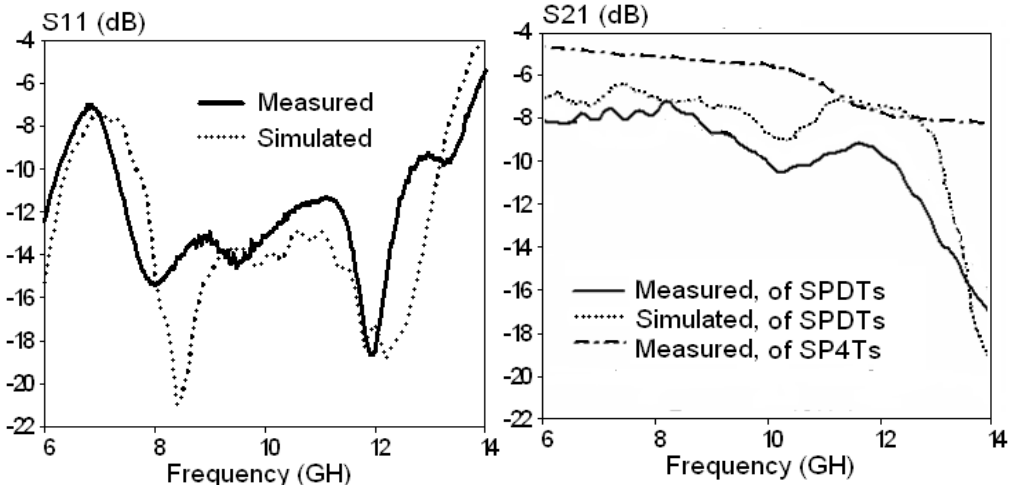

(a) Return Loss (b) Insertion Loss

Figure 5.11: Measurement Results of SP16T Switch.

5.4. Study of Mutual Coupling

The developed full array is for SAR operation where only one single antenna is used at a time. It is well understood that the mutual coupling would affect SAR's operation to a great extent, if not compensated during image formation. Hence, mutual coupling due to the presence of the neighboring elements must be minimized. An extensive set of measurements are carried out to evaluate such effects as function of each sub-array's location on the full array. The linear full array and its sub-arrays are represented as Figure 5.12.

In this implementation with a physical spacing of 2.4 cm, the coupling between these 16 sub-array elements is less than -23 dB as shown in Figure 5.13. The parameter S_{NM} represents the coupling level between the sub-array in the P_N and P_M positions, valued by HP8510C VNA's S-parameter measurement. Mutual coupling effect on the radiating element patterns has also been investigated as indicated in Figure 5.14, where the radiation pattern was measured first for one sub-array (the central one), then compared to those of adding N sub-arrays at both sides of the central one. In Figure 5.14, N=0 means there is no neighboring sub-array next to the central one, N=1 means adding one terminated sub-array at both sides of the central sub-array, and so on. The differences between these various radiation patterns are not significant and for all practical reasons they can be assumed constant in the SAR implementation.

The measurement indicates that the assumption that all sub-arrays are adequately independent of each other is a good approximation; otherwise extensive calculations are required to account for the radiation pattern variation and mutual coupling in the SAR code implementation. Wider spacing between the elements should reduce the mutual coupling between the elements, but it could cause unwanted grating lobes.

In conclusion, the design of a full SAR array based on Vivaldi antenna is presented. The array design is optimized to have a compact size and almost constant gain with its frequency range. The design of an ultra-wideband SP16T switch to automate the full array is also discussed. The full array is manufactured and connected to SP16T switch and will be utilized as part of STW imaging system. The implemented array covers 8-12 GHz and is geared towards see through low-loss material such as dry-wall for high resolution. As is discussed in Chapter 4, it may be desired to operate STW system at lower frequency for better signal penetration especially for lossy walls such as concrete walls. The nature of Vivaldi antenna allows it to be easily scaled up/down in frequency range to cover one specific frequency range while not changing its element configuration.

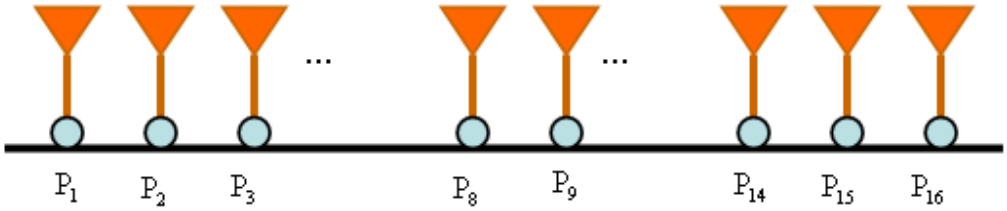

Figure 5.12: Element Locations.

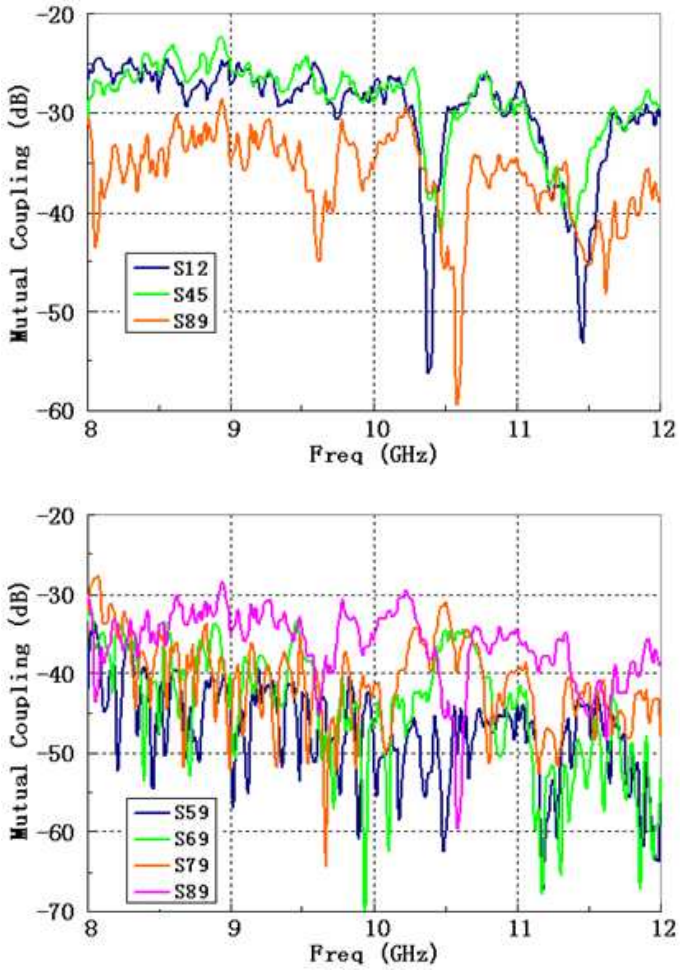

Figure 5.13: Mutual Coupling.

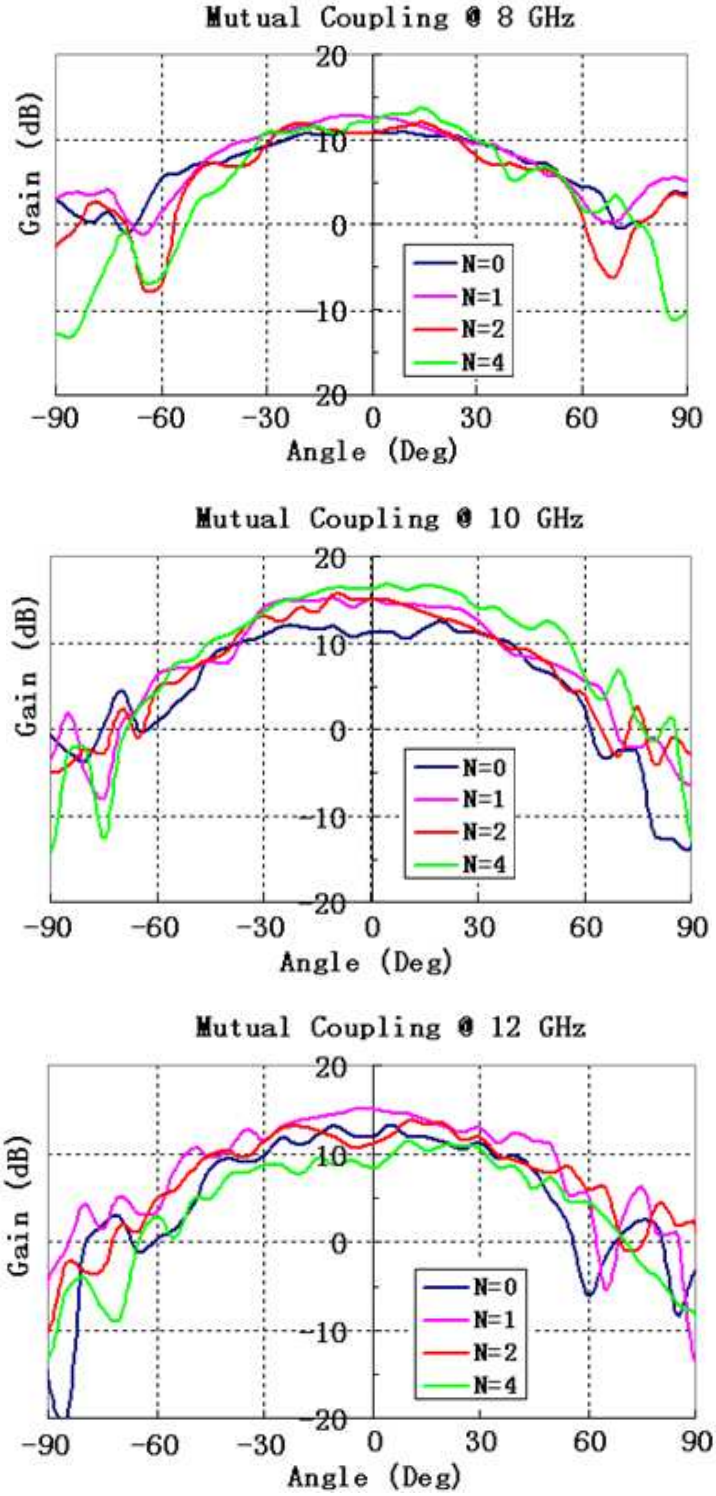

Figure 5.14: Subarray Patterns.

Chapter 6 . CONCEPTUAL SYSTEM BASED ON OSCILLOSCOPE

Based on the previous study of STW modeling, wall characterization, and image formation, a conceptual UWB STW imaging system is developed. The system is comprised of the previously developed UWB Vivaldi array, off-the-shelf components, and RF instruments. System integration including hardware and software aspects will be discussed in detail. The goal is to provide an experimental platform of minimum design complexity and cost, which is capable to run full-scale see-through-wall testing for concept demonstration and further imaging method studies [80][81]. The system leverages our efforts to develop Vivaldi antenna subarray and a custom UWB reconfigurable pulse generator [82]-[86]. The introduced system architecture, based on an oscilloscope, provides a simple and universal control/automation/data acquisition mechanism that is independent of the operating frequency. The current system is centered at 10 GHz to see through low-loss materials like drywall. However, a lower-frequency design to see through high-loss materials like concrete-wall can be reconfigured by replacing a few components in the radar transceiver and scaling the Vivaldi antenna elements, while the majority of the hardware and software modules remain untouched. Preliminary imaging results from the developed system will be discussed.

6.1. Transceiver Design

Since a carrier signal is required to up-convert the UWB signal to a high center frequency as 10 GHz, a conventional homodyne transceiver is implemented, as shown in Figure 6.1. In order to reduce the design cost and complexity, off-the-shelf products are used except a few key components, such as the array and the pulse generator. A typical example of an operating mode is: The transceiver sends out subnano-second pulse train at 10MHz rate, which is modulated by a 10 GHz LO signal through the mixer. The array received-signal is down-converted through I/Q demodulation, and then routed to the oscilloscope. The 10 MHz sine wave signal from a function generator instrument will feed the pulse generator, controls the pulse repetition rate, and also provides the sampling synchronization to the oscilloscope.

The mathematical forms of the signal flowing through the transceiver are derived as follow. The original transmitted signal is a pulsed modulated carrier as Eq.(6.1), where *p(t)* is the UWB pulse train and f_C is the carrier frequency.

$$S_T(t) = p(t)\sin(2\pi f_C t), \qquad \textbf{(6.1)}$$

The returned signal expressed in Eq.(6.2) will be a delayed replica of the transmitted signal,

$$S_R(t) = A * \sin(2\pi f_C t + \varphi(t)) = G * p(t - t_R) * \sin(2\pi f_C t - 2\pi f_C t_R), \textbf{(6.2)}$$

The phase term in $S_R(t)$ is introduced by the round-trip travel time from the radar to a target, assuming the distance between them is *R*. The phase term is expressed as Eq.(6.3).

$$\varphi = -2\pi f_C t_R = -2\pi f_C \frac{2R}{c} = -\frac{4\pi R}{\lambda}. \qquad \textbf{(6.3)}$$

The $S_R(t)$ can also have the following form:

$$S_R(t) = A * \sin(2\pi f_C t + \varphi(t)) = A * \cos(\varphi(t)) * \sin(2\pi f_C t) + A * \sin(\varphi(t)) * \cos(2\pi f_C t) \quad \textbf{(6.4)}$$

Through quadrature demodulation implemented by the homodyne transceiver, the in-phase and quadrature components can be separated from the received signal,

$$I = A\cos(\varphi(t))) \qquad \textbf{In-phase component,} \qquad \textbf{(6.5)}$$

$$Q = A\sin(\varphi(t))) \qquad \textbf{Quadrature component.} \qquad \textbf{(6.6)}$$

I and Q signal will then be translated into target range information, through Sum-and-Delay beamforming method or other advanced radar imaging methods.

6.2. System Integration

The overall STW experimental setup in Figure 6.2 consists of a customized radar transceiver, a Tektronix TDS8200 sampling oscilloscope, an Agilent 33220A function generator, an Agilent 83622B synthesized generator, and an Agilent E3631A DC power supply. An UWB horn with 1-18GHz range is used as the transmitting antenna and the full array is for receiving. The TDS8200 oscilloscope is to digitize the received radar signal and be the controller of the whole system. The 33220A function generator provides the pulse trigger signal and the sampling synchronization signal. The E3631A power supply feeds the necessary DC bias to various components in the transceiver and the SP16T switch. The 83622B synthesized generator is the source of LO signal. Figure 6.3 illustrates the interconnection of the system. There are two categories of interconnections: the first is for the system automation and control purpose, including GPIB bus connection between the instruments and the Parallel port connection from the TDS8200 to the array switch. The second is the microwave signal connections between the transceiver and instruments.

The STW system is controlled and automated by the TDS8200 oscilloscope, which is also a windows-based PC. A computing environment and a programming language, Mathworks Matlab, installs on the TDS8200 first. Then a Matlab command-line script is written to control the TDS8200 and other associated instruments through GPIB bus and Parallel ports on the rear panel of the TDS8200. The detailed methods of utilizing Matlab scripts to control the oscilloscope and other instruments through GPIB bus and Parallel port can be found in [87][88]. A flowchart of the developed script is shown in Figure 6.4. The script first initializes the TDS8200, setting up the sampling resolution, sampling points, memory length, and etc. Then it continues to send out commands through GPIB bus to configure the connected synthesizer generator, the power supply and the function generator for desired operating parameters. After that, the script sequentially sends out 4-bit code to the SP16T driver through the parallel port on the TDS8200. When a specific sub-array is turned on and stabilized, the script continues to instruct the TDS8200 to sample and store incoming signals from the transceiver. The sampling process is

completed if the data from all array channels are collected. A Matlab image formation module can be included in the script to process the collected radar signal and display images on the screen.

This experimental STW system using the developed synthetic aperture array provides a synthetic steering capability in the azimuth plane and allows static STW imaging. It provides much experimental flexibility. It is built for potential high-resolution imaging purpose, due to its high operating frequency around 10 GHz. However, for better penetration and lower loss, it is desired to operate a STW system at lower frequency such as around 3 GHz. Luckily, the flexible and simple array control/automation mechanism based on the sampling oscilloscope allows one to accommodate the system to a lower operating frequency with least modification. For example, the Vivaldi array can be easily scaled to frequency around 3 GHz; by using off-the-shelf UWB components, the RF transceiver can cover extremely wide frequency range; the Matlab-based oscilloscope control/sample/process script is a universal module regardless the system frequency; the use of a synthesized source provides a wide range of selection of the LO frequency. Sampling scope normally provides a wide analog bandwidth but extremely low sampling speed, which limits its use to repetitive signals and static scenarios. For a real-time application, high-performance real-time oscilloscope can be used. Following is one example of the experimental results. To have an optimized microwave frond-end/ transceiver design, the electronic design automation tool, Advanced Design System (ADS) can be used to perform the transceiver link-budge/noise analysis [89]. Particularly, ADS provides an UWB library of UWB components and UWB channel models, which allows an easy UWB system simulation [89].

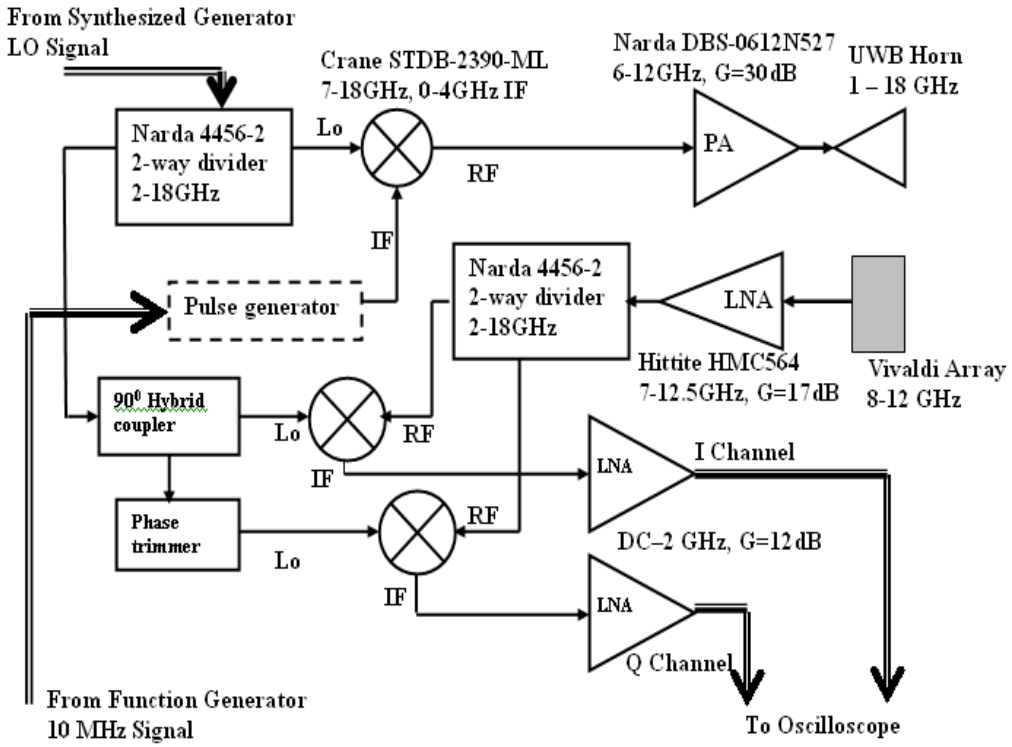

Figure 6.1: Radar Transceiver.

Figure 6.2: STW Setup.

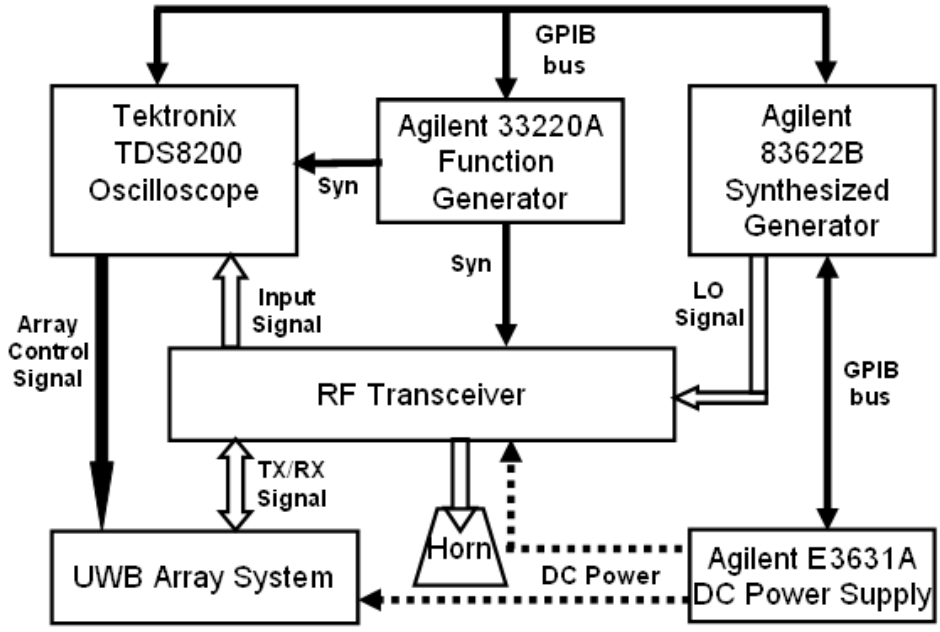

Figure 6.3: STW System Diagram.

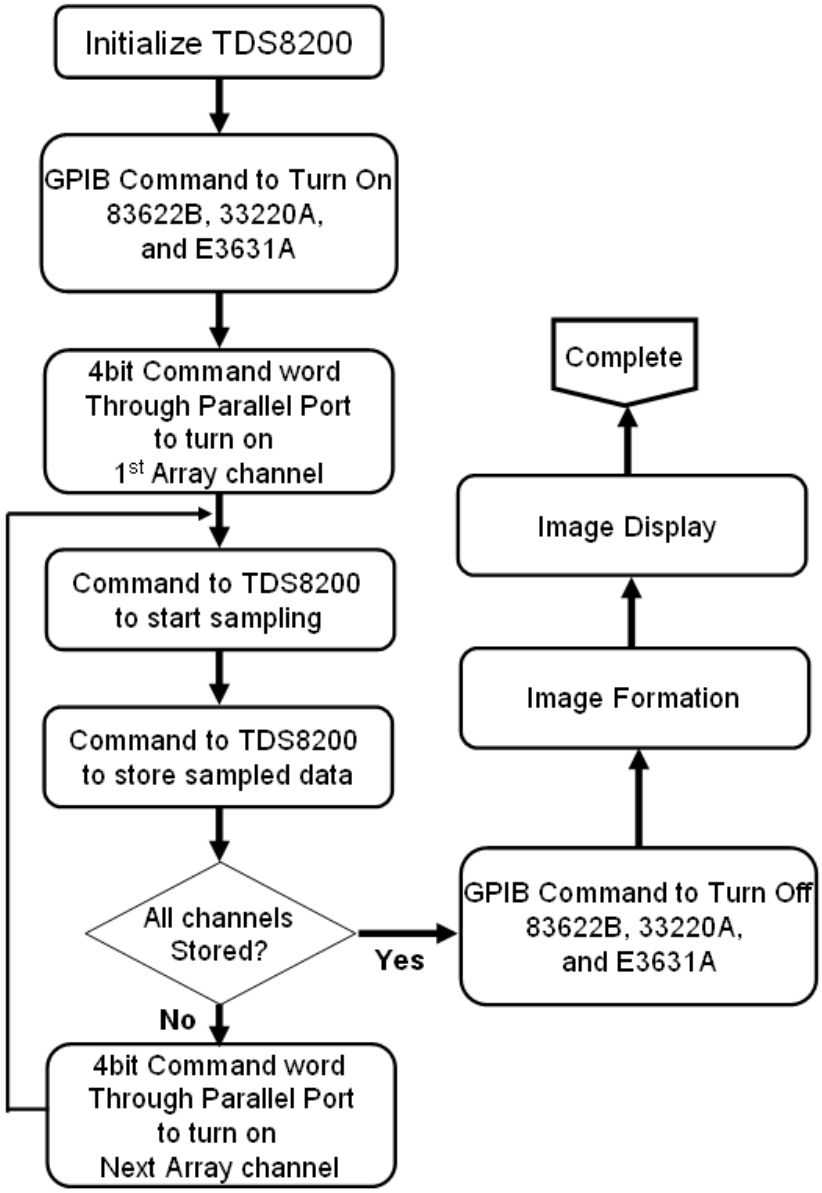

Figure 6.4: Flowchart of Matlab Script.

6.3. Experimental Result

As the first system test, a 50cm square metal plate was placed 8 meters in front of the array as a radar target and no wall is placed between the radar and the target. The reflected signal, received by the array and digitized by the TDS8200, is plotted on Figure 6.5. Each subplot (from C1 to C16) shows I channel trace in red and Q channel trace in blue. The data was processed through Sum-and-Delay beamforming algorithm. The resulted image is shown in Figure 6.6 and the red highlighted spot, target image, clearly identifies the position of the metal plate. The resulted image validates the proper functioning of the transceiver, the full array, and the system automation blocks.

STW experiments are then carried in a more sophisticated environment, inside a building corridor. The floor plan of the corridor is shown in Figure 6.7. The corridor is shielded by concrete walls on sides, with a side wall block on the far and two metal doors. A 0.5-inch-thick drywall panel is placed 0.5m in front of the radar system to simulate the wall structure. Two target objects are placed at the scanning plane of the SAR radar. One target is a metal cylinder with a 12cm diameter and 24cm height; the other is a 20cm x 15cm x 24cm metal tank. The oscilloscope-collected SAR data is processed through the time-domain Sum-and-Delay beamforming algorithm, which cause fast scanning over a large area. One typical resulted image is plotted in Figure 6.8. One may identify the locations of the two targets precisely, and discover rough layout information of the corridor. The reflection from the drywall is translated into the blurred spots in Figure 6.8. The positions of the side wall block and metal doors are well identified.

Because of the low loss and low reflection, the drywall is almost transparent to the radar signal, and doesn't cause severe defocusing on the image. However, the characteristics associated with a realistic STW application, such as the through-wall scattering mechanism and limited radar aperture size make it very difficult to form high-resolution images. The defocusing mechanism and its correction due to wall structures have been addressed in Chapter 3. A simplified wall model is presented again in Figure 6.9 to address the importance and challenge of image formation. The geometric signal path between Transmitter R and Target P is $L = L1 + L2 + L3$, but the actual electrical length is $Lef = L1 + \sqrt{\varepsilon_r} L2 + L3$. This wall effect need to be corrected otherwise will cause defocusing of images. Authors developed an iteration method based on the classical back-projection method to correct the defocusing due to an unknown wall. However, it is still impractical to use such a time-consuming method to solve the STW problem in a realistic environment where the much more complicated building structure presents.

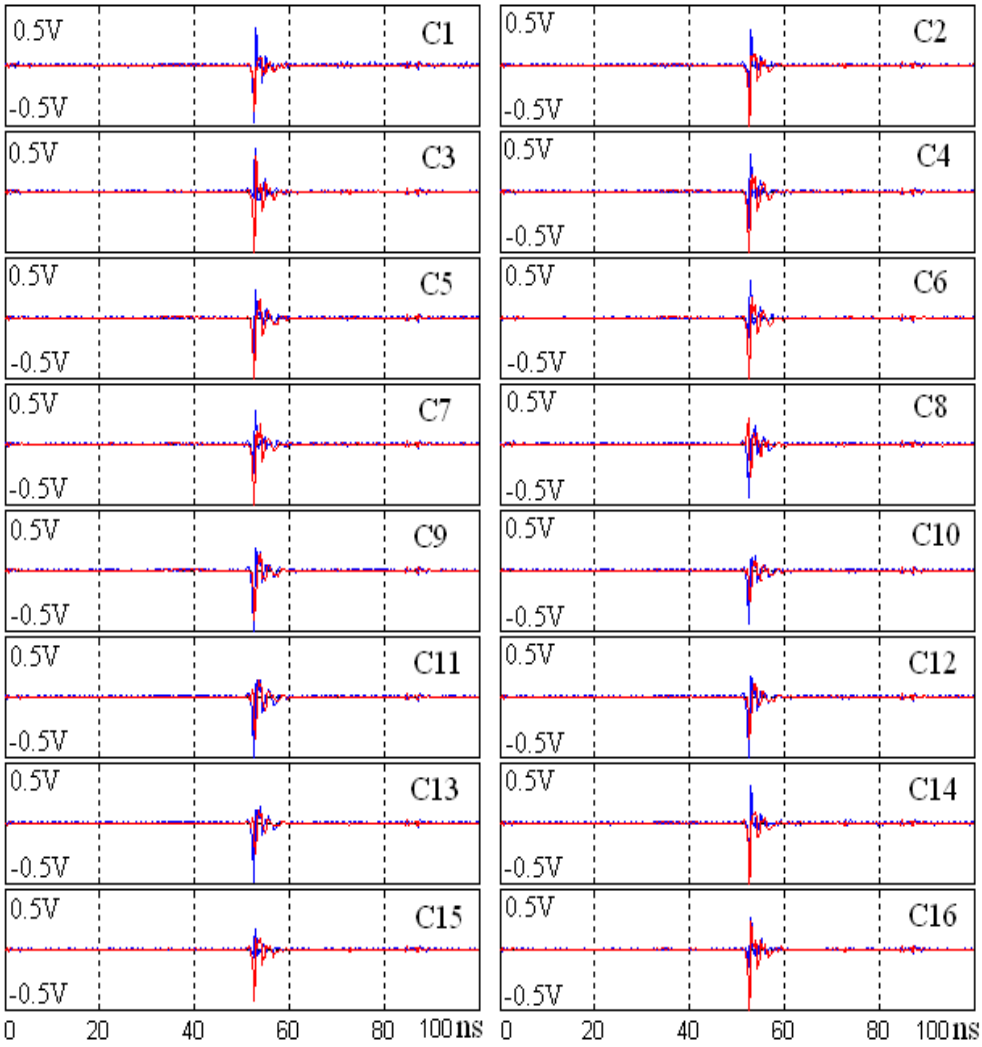

Figure 6.5: Full Array Time-domain Data.

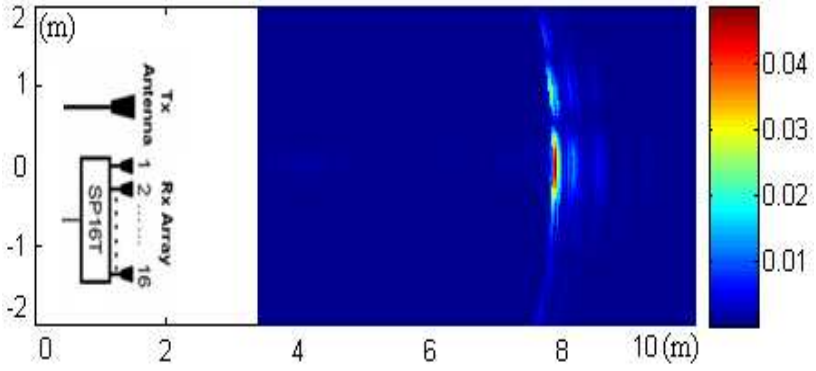

Figure 6.6: Synthetic Beamforming Image

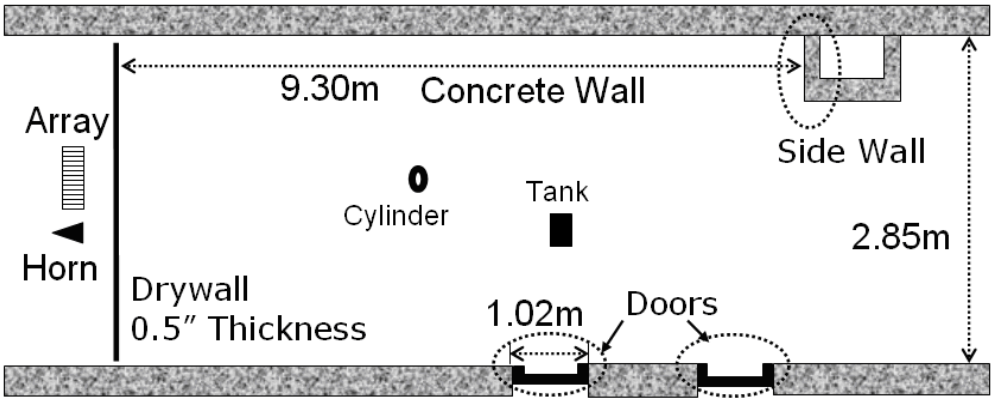

Figure 6.7: Diagram of Corridor.

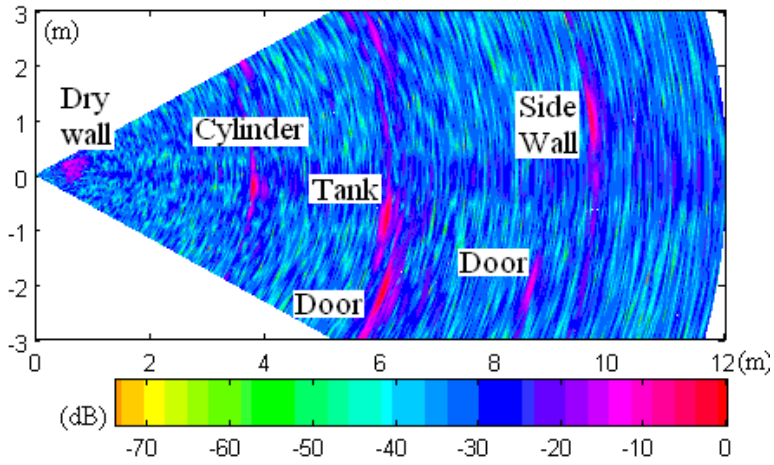

Figure 6.8: Far-Field Beamforming Image.

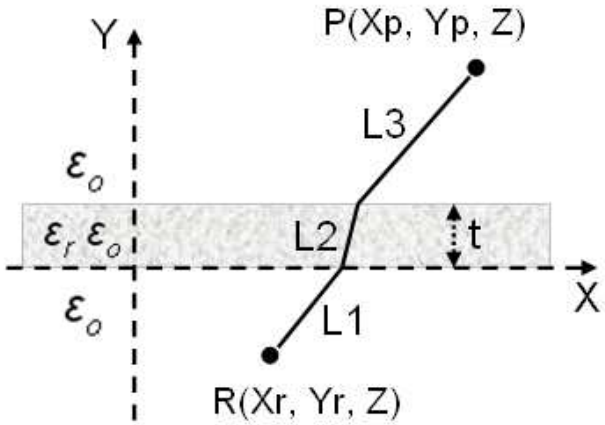

Figure 6.9: Dielectric Wall Model.

Leveraging the effort of STW simulation based on CFDTD, which has been discussed in Chapter 3, one real experimental scenario is then modeled in CFDTD to compare with experimental results. One simple experiment is carried out in an open space area first: a metal panel (12 cm x 24 cm) is placed at different distances from the radar directly (no wall in between), and the beamforming image is formed after collecting data from the receiving array. The targeted panel is placed 1.7m and 3.4m away from the radar. The corresponding model was built in CFDTD: a pulsed source centered at 10 GHz is implemented in order to simulate the actual experimental scenario. The images recovered from the simulated and actual experimental data are processed through Sum-and-Delay and Back-projection imaging method; then compared in Figure 6.10-Figure 6.13. The comparison shows very good agreement between numerical and experimental data.

The operation of the designed STW system has been validated through experiment and simulation. It provides the capability of azimuth-plane scanning and makes static imaging through low-loss materials. The system utilizes off-the-shelf components/instruments, and leverages the available hardware and software technologies. The introduced flexible system architecture allows reconfiguring the system to operate at various frequency ranges with little design effort and reconfiguration. The progress in UWB hardware development has made it possible to design a full system with reasonable cost and complexity.

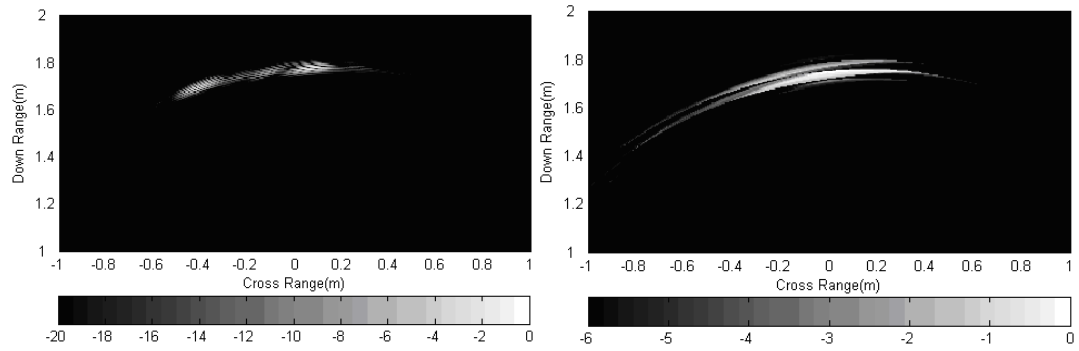

(a) Simulation: Backprojection (b) Measurement: Backprojection

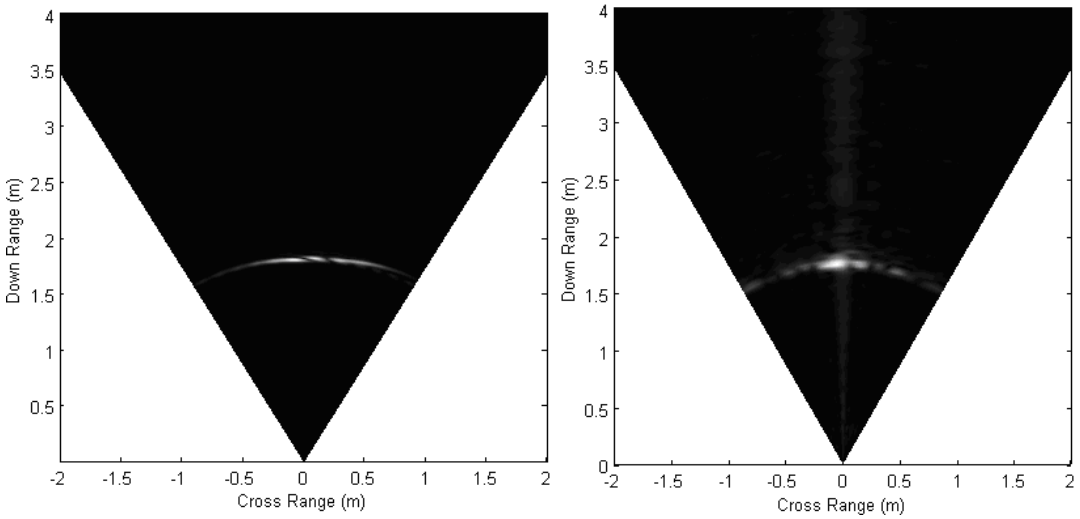

(c) Simulation: Sum and Delay (d) Measurement: Sum and Delay

Figure 6.10: Metal Panel – 12cm, 1.7m away.

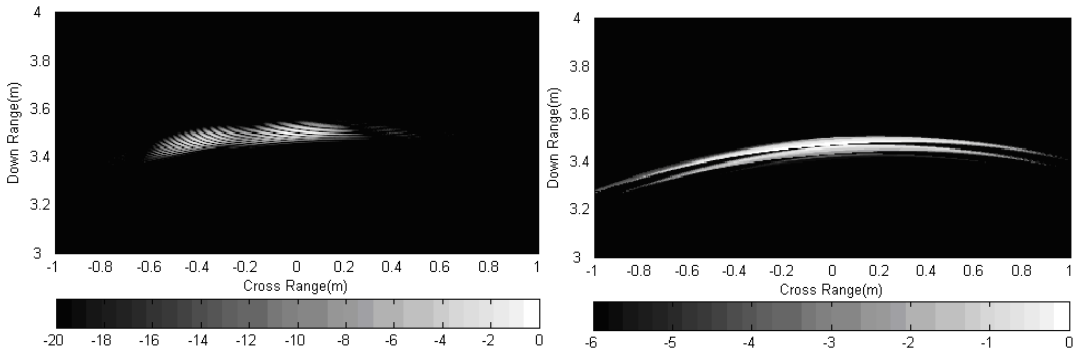

(a) Simulation: Backprojection (b) Measurement: Backprojection

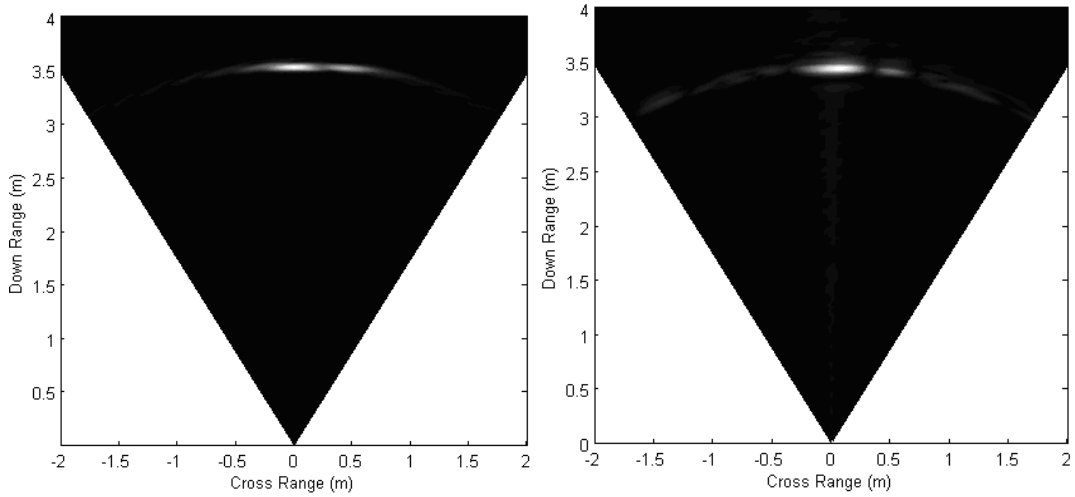

(c) Simulation: Sum and Delay (d) Measurement: Sum and Delay

Figure 6.11: Metal Panel – 12cm, 3.4m away.

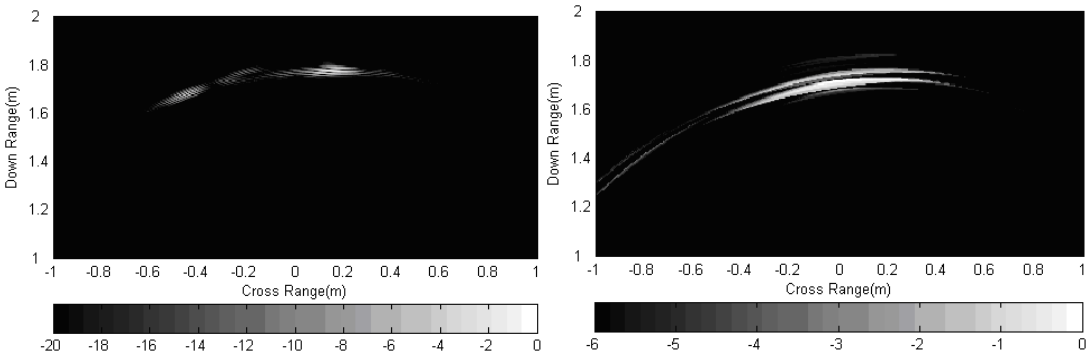

(a) Simulation: Backprojection (b) Measurement: Backprojection

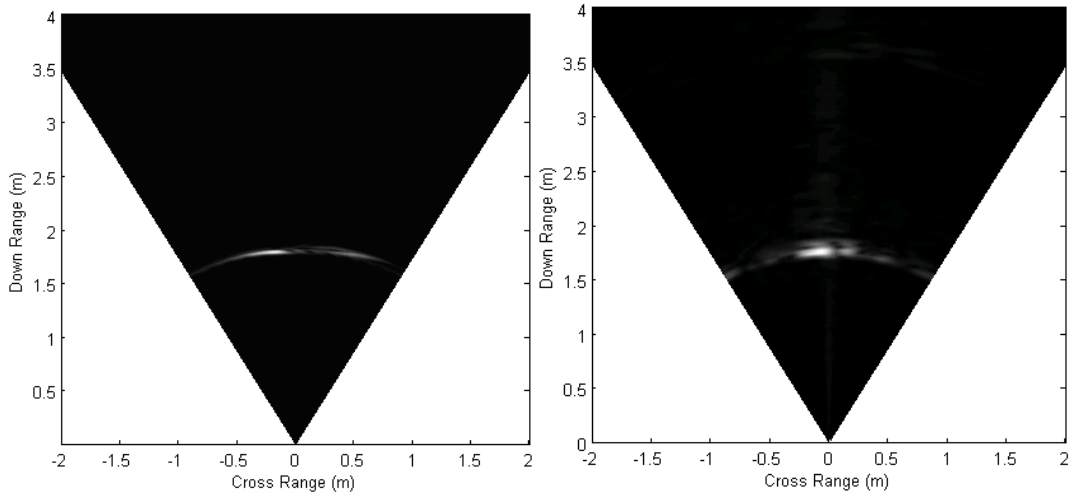

(c) Simulation: Sum and Delay (d) Measurement: Sum and Delay

Figure 6.12: Metal Panel – 34cm, 1.7m away.

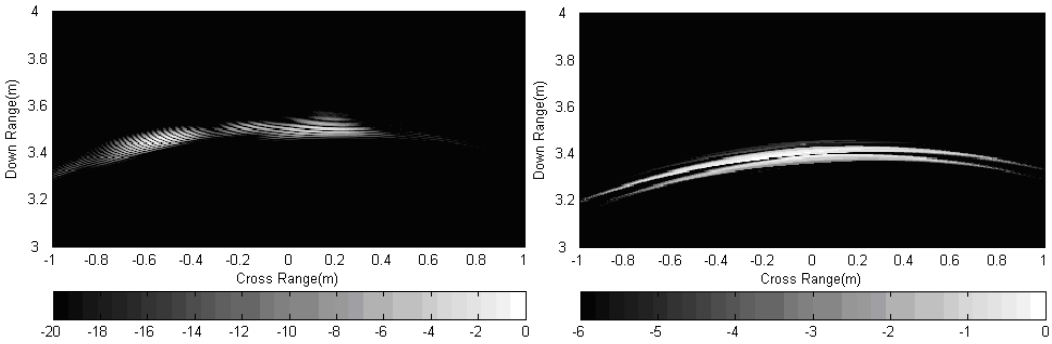

(a) Simulation: Backprojection (b) Measurement: Backprojection

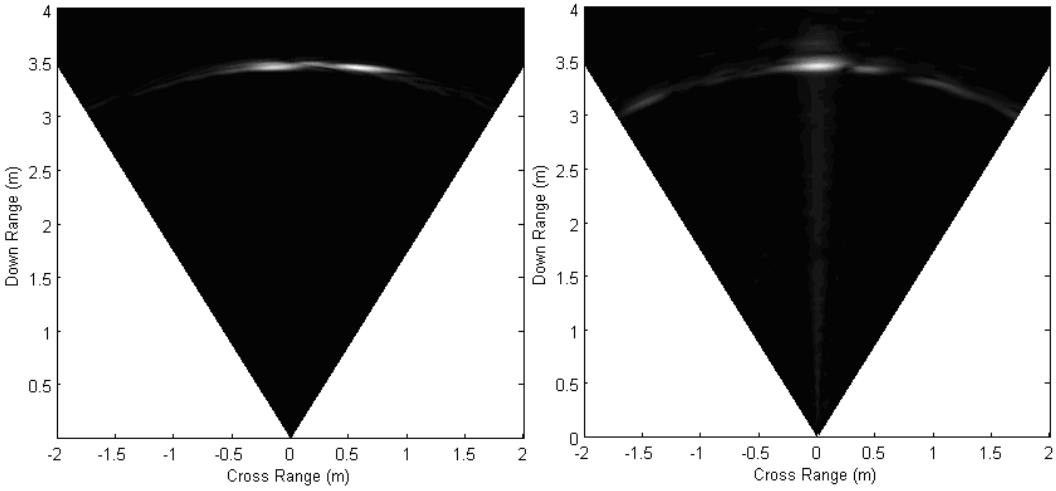

(c) Simulation: Sum and Delay (d) Measurement: Sum and Delay

Figure 6.13: Metal Panel – 34cm, 3.4m away.

Chapter 7 . STANDALONE REAL-TIME SYSTEM BASED ON FPGA

7.1. Design Consideration

There are various design parameters that need to be established before implementing the design concepts. First, the FCC requires that STW systems should operate either below 960 MHz or within the frequency band 1.99-10.6 GHz (Table 1). Our study in Chapter 4 shows that the practical frequency is below 3 GHz to best penetrate high-loss material such concrete block; meanwhile the frequencies up to 10 GHz have the potential of resolving higher imaging resolution and of resulting in more compact radar front-end (array size particularly), but only suitable for low-loss walls. The wall-associated feature leads to a necessary trade-off among minimizing propagation loss, maximizing imaging resolution, and maintaining a realistic front-end size.

Secondly, the system power requirement should be planned to accommodate the STW features. At a fixed operating frequency, the power requirement is determined by the radar equation,

$$SNR = \frac{PG\lambda^2\sigma}{(4\pi)^3 R^4 L F_n k T_o B} \qquad \textbf{(7.1)}$$

where P is the transmitted power, G the antenna gain, σ the target cross section, R the radar range, L the system loss, F_n noise figure, k Boltzmann's constant, and B is the noise bandwidth. In STW applications, the detection of human being could be of most concern. Studies show that the RCS of a human body at various positions (standing or kneeling) may swing between 0 to -20 dB, given that a human body has about 1 m^2 RCS [90]. The loss through walls could be significant, and a 10 GHz signal through a concrete block would suffer a 30 dB round-way loss [90]. Assuming a 14 dB SNR for a reliable front-end detection and a 10 dB antenna gain, a STW system would require at least 54-dB dynamic range (how many bits!!!!) for the front-end processing. For a practical system, the link budget needs to be analyzed, taking into account the radar front–end performance, the detection range, and the FCC rules if applicable.

The implementation of subsystems could be a hardware design, such as the front-end, or combination of hardware and firmware like the data acquisition module. For the microwave frond-end, the UWB pulse generator and the antenna array are of most concern. The UWB pulse will directly impact the system bandwidth and the range resolution. Various design methods have been reported to generate a pulse with the desired frequency bandwidth, pulse width, and pulse shape. Along with the generation of UWB pulse, the antenna need adapt to UWB transmission. Several types of antennas have been utilized in STW applications, including horn antennas, Vivaldi antennas, and patch antennas. The selection of antennas will eventually depend on the system's requirement on portability and bandwidth. The pulse generator and the antenna need custom consideration for their critical requirement on UWB performance. As of the rest

parts in the front-end like amplifiers, filters, mixers, and etc., commercially available off-the-shelf components could be sufficient for an experimental platform.

One great challenge of the STW system development may reside in the acquisition of UWB signal. For example, to capture an UWB pulse of 1ns width, a fine acquisition module needs to have 200ps sampling resolution (5GSample/s rate) and analog bandwidth of several GHz. Commercial solutions, such as PCI-based digitizers and real-time/sampling oscilloscopes, are available yet very expensive [92][93]. A custom low-cost data acquisition module will be favorable for a SWT platform. Two mostly used sampling methods can be considered for a custom design: real-time sampling and equivalent time sampling [94]. Luckily, in a STW scenario, the returned radar signal can be considered quasi-static and periodic within a short period of time, which makes equivalent time sampling a feasible option. The advantage of the equivalent-time sampling is to achieve a relatively high sampling resolution, such as 200ps/sample, at low real-time rate, i.e. 100MSample/s instead of 5GSample/s. Equivalent-time sampling method will also relax the specs of the data storage structure. A real-time digital data stream at 5GSample/s would be difficult to handle, while receiving a digital data stream at 100Msample/s will be a much more realistic.

A data acquisition module based on the equivalent-time sampling method could be sufficient for a STW system, but the acquisition time needs to budge against the detectable target speed in a real-time operation. The waveform samples need to be collected within the time period that a moving target takes to cross over one resolution cell while the returned waveform is considered ‘constant’. The target speed and the acquisition time are related by,

$$\Delta t = \frac{\delta R}{v} = \frac{3cm}{5m/s} = 6ms \quad \textbf{(7.2).}$$

Given a target moving at 5m/s and a 3cm resolution cell are assumed, the available time to collect the equivalent-time samples and recover one ‘constant’ waveform is then only 6ms.

Finally, for a standalone system, one digital control/process assembly is needed to integrate and synchronize various radar subsystems. It also needs to process the received radar signal. FPGAs have turned out to be an ideal platform for such a system prototyping [95]-[97]. Commercial FPGA boards can be used to implement the control/process module.

It is concluded that the developed system has to be an adaptable platform that can be utilized over a wide frequency range. It should cover a practical range of 15 m, and the power level/dynamic range should satisfy the experimental needs of see-through-concrete-wall. The microwave front-end discussed in Chapter 6, including the full array and transceiver, will be used for the real-time system. A real-time data acquisition module will be developed to handle a typical UWB pulse narrower than 1ns.

7.2. Design of the Data Acquisition Module

As previously discussed, an equivalent-time sampling method could be sufficient for a quasi-real-time STW application. The implementation of a data acquisition module typically includes both hardware and firmware developments. The hardware development is to integrate ADCs, timing circuit, memory, microcontroller, and auxiliary circuits on a printed circuit board. The firmware is a set of embedded programs to control the hardware. For any standalone system, the firmware development is a common practice, while the UWB hardware implementation will require high-speed wideband mixed signal circuitry designs and could be challenging. We introduce here a low-cost implementation approach that utilizes commercial ADCs and FPGA boards to realize high- performance data acquisition. Such approach needs not to go through the hardware development, but only requires a FPGA firmware implementation, which significantly cuts off the design lead time. This section will introduce the hardware module first, and the firmware design will be discussed in the next section along with the control/process assembly.

The used commercial products are one Avnet Xilinx Virtex-4 FPGA evaluation board and two MAX108 ADC evaluation boards (see Figure 7.1). The ADC has a 9-bit output, 2.2 GHz analog bandwidth and a 170 MHz maximum sampling rate [98]. Given the rule of thumb that every bit of an ADC represents 6 dB of dynamic range, the 9-bit ADC will provide the required 54 dB dynamic range. The Avnet board is populated with a Virtes-4 FPGA chip, 50 MHz oscillator, RS232 transceiver, I/O connectors, and etc [99]. An Avnet AvBus Breakout module (see Figure 7.1) is used to break in/out the digital date between the FPGA and the ADCs boards [99].

Equivalent-time sampling method requires a high-precision timing circuitry, which introduces a very fine delay, i.e. 200ps, to the ADC sampling clock and acquires samples at the correct time instant of a repetitive waveform. Programmable delay chips are often used. For example, AD9501 of Analog Devices has a 10ps incremental delay resolution and a 2.5ns full-scale range; MC100EP196FA of On Semiconductor provides the same 10ps delay resolution but with a maximum 10ns delay range. At first glance, such a timing circuitry seems missing from our proposed hardware module. However, we notice that FPGA boards are often equipped with clock generators with fine phase adjustment in order to align digital clocks. For example, the Avnet board integrates a TI CDC5801 clock multiplier/divider, for multiplying/dividing a reference input clock (REFCLK) to an output clock (CLKOUT). The output clock (CLKOUT) can be delayed/advanced in a minimum step of 1/384 CLKOUT period through the CDC5801's terminal controls [100]. The CDC5801 chip alone doesn't look more attractive than other programmable delay chips, but since one is already integrated on the Avnet board, it is possible to generate the equivalent-time sampling clock through FPGA firmware and get around the extra hardware design.

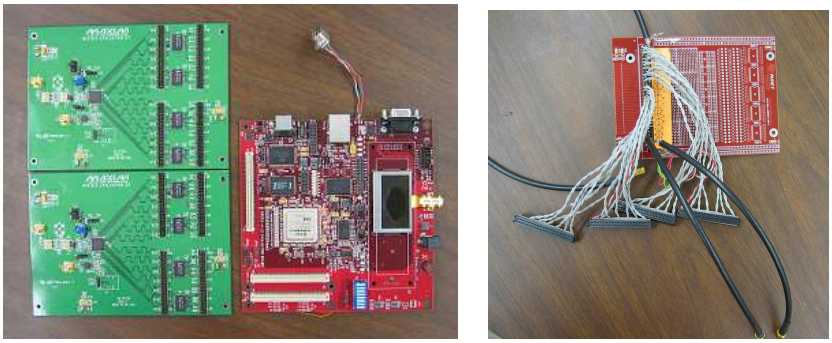

(a) Avnet and Maxim boards (b) Avbus Breakout module

Figure 7.1: Data acquisition hardware module.

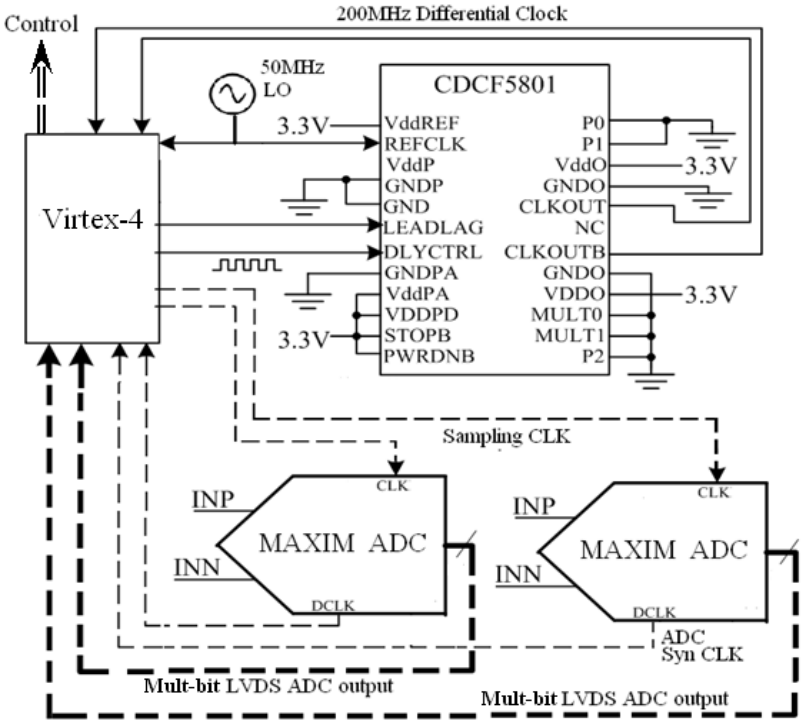

Figure 7.2: Diagram of the data acquisition hardware module.

The overall diagram of the data acquisition module based on the chosen hardware is demonstrated in Figure 7.2. On the Avnet board, the CDC5801's various control terminals are pre-connected to the Virtex-4 chip, including the CLKOUT/CLKOUTB clock output; one 50MHz oscillator is distributed to both the CDC5801 and the Virtex-4 chips simultaneously. One developed firmware running on the Virtex-4 chip would manipulate the CDC580, in terms of the frequency multiplication/division and the phase advancement/delay, to generate the sampling clock to ADCs, and simultaneously receive/store the ADC output samples. The FPGA firmware also generates the synchronization clock to the pulse generator and the 4-bit TTL signal to the SP16T switch driver. The interface between the Avnet board and the rest part of the system (dashed lines in Figure 7.2) is completed by the AvBus Breakout module. The Breakout module plugs into the AvBus connectors on the Avnet board, and enables an easy access to the I/O banks of the Virtex-4 chip. SMA cables are used to break out the ADC sampling clock and the pulse synchronization clock. Twisted-pair wires are used to connect each bit of the ADC's differential output to the FPGA board [101].

7.3. Design of the FPGA Firmware

The purpose of the FPGA implementation is to complete the UWB data acquisition firmware and also develop a control/process module which integrates the STW system. In FPGA development, users provide a schematic design or a hardware description language such as Very High Speed Integrated Circuits (VHDL) to define the behavior of FPGA [102]. Our schematic and VHDL design is done in Integrated System Environment (ISE), the design package provided by Xilinx Inc. The overall functional structure of the implemented FPGA system is demonstrated in Figure 7.3. There are five major blocks: a timing logic, memory banks, a beamformer imaging module, an embedded microprocessor, and a system control logic (FSM). The timing logic, along with the CDC5801 chip, realizes the equivalent-time sampling mechanism. Two memory banks with an identical structure are created for continuous data storage, which alternate to store incoming digital samples. Once a bank is fully loaded, the other will take over the storage task while the loaded one will interact with the post-processing blocks, the imaging or microprocessor modules. The system control unit (FSM) plays an essential role in coordinating each functional block.

Although the development of the FPGA firmware for a real-time STW system could be labor-intensive, the implementation process is standard and straight-forward, not different from the system prototyping of other applications. The use of FPGA as radar digital front-end has also been a common practice [103][104]. The implementation here doesn't intend to achieve an optimum design from the FPGA aspect, but to realize a fast STW system prototyping through the strength and easy use of the FPGA technologies. This section will address key FPGA logic elements and design features that particularly favor the STW real-time application.

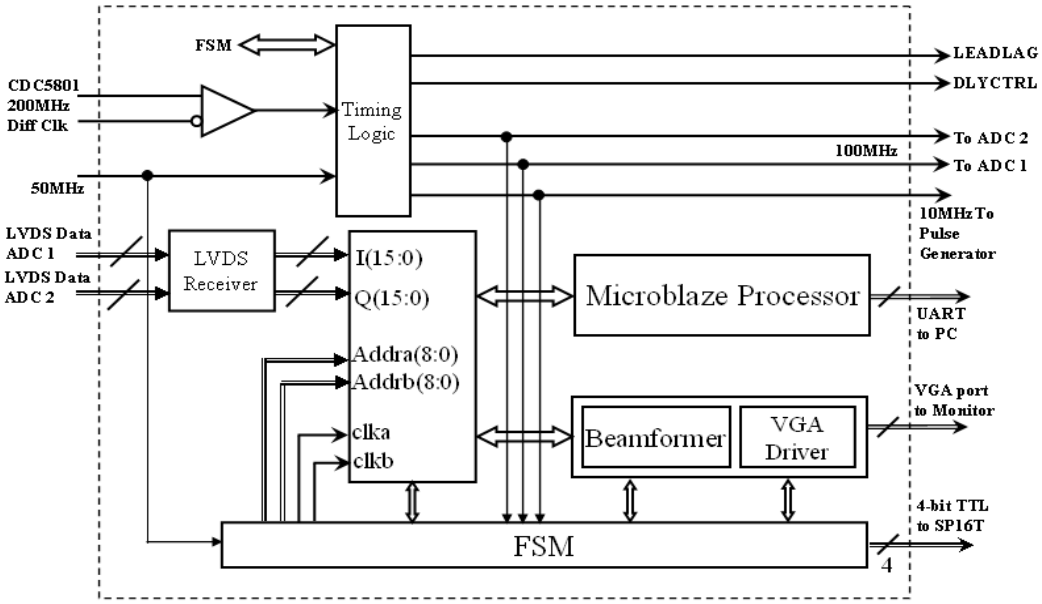

Figure 7.3: Functional blocks of FPGA system.

A. Generation of Equivalent-Time Sampling Clock

The timing logic is to collaborate with the CDC5801 chip and generate 100MHz ADC sampling clock, which has a relative phase difference to the 10MHz pulse train, as illustrated in Figure 7.4. The destined or intermediate clocks are aligned to the 50MHz clock with zero phase difference, after initializing the Virtex-4 and CDC5801 chips. Then the timing logic generates a series of control signal at the CDC5801's LEADLAG and DLYCTRL terminals (see Figure 7.5), which will delay or advance the 200MHz clock in a step of 1/384 period (13ps). The 100MHz clock will inherit the phase of the 200MHz clock; hence an adjustable phase difference measured in time will be established between the 10MHz pulse train and the 100MHz sampling clock, which enables the equivalent-time sampling. A 100MHz clock isn't generated directly because the CDC5801's minimum Multiply rate is 4.

During the 1st 10MHz clock cycle, the LEADLAG terminal of the CDC5801 is set low and a series of 200MHz clock cycles pass onto the DLYCTRL terminal (Adjust 1 in Figure 7.6). For every rising edge at DLYCTRL, the CDC5801's 200 MHz output is delayed by 1/384 period (13ps) [100]. After feeding 16 200 MHz clock cycles, the resulted 200 MHz clock will have 208ps delay compared to its original phase and also to that of the 10 MHz clock. When the 2nd 10 MHz clock cycle arrives, the timing logic will stabilize the phase difference by switching the signals on DLYCTRL and LEADLAG terminals to 50MHz and 200MHz clock respectively. Starting from the 3rd cycle, a delay of 208ps is established between the 10 MHz and 100 MHz clocks and the 100 MHz clock will trigger ADCs for 10 samples over one radar pulse cycle (100ns). The sampling will continue through N 10MHz clock cycles and accumulate/average the N samples at each of the ten sampling positions (N=4, Collect 1 in Figure 7.6). Then the timing logic switches back to the 'Adjust' mode, and feeds another 16 200 MHz clock cycles at DLYCTRL (Adjust 2 in Figure 7.6). Now the delay increases to 416ps and the second group of 10 samples with an averaging factor N will be collected. The process will repeat 24 times until reaching the maximum 5ns delay range (one period of 200 MHz). However, the required delay range is 10ns for the combination of a 10 MHz pulse repetition rate and a 100MHz sampling rate. The other 5 ns delay will be achieved through advancing 200 MHz clock 24 times at a 208ps step by pulling up LEADLAG terminal at "Adjust" stage. After 48 times of 'Adjust/Collect' cycles, the samples at 480 positions will be collected to recover the radar waveform of 100ns period. Given an averaging factor of 8, the number of elapsed 10 MHz pulse cycles is (8+2) x 48, i.e. 48s.

The 48s is the time to acquire the waveform from one array channel. The 4-bit TTL word to the SP16T switch driver needs to be increased from '0000' to '1111' at 0.48μs interval to turn on each array channel. It will take 48μs x 16, i.e. 0.768ms, to collect a full frame of array data. A finer sampling resolution such as 104ps can be achieved if the number of 200MHz clock cycles at DLYCTRL terminal during the "Adjust" stage is reduced to 8 instead of 16. The trade-off is that the number of 'Adjust/Collect' cycles becomes 96 and the time required to collect one frame increases from 0.768ms to 0.768ms x 2, i.e. 1.536ms. In principle, the finest sampling resolution would be 13ps, the minimal delay

step of the 200MHz clock. But the trade-off for an 'easy' implementation, which utilizes AvBus Breakout module as the digital data interface, is the degradation of the achievable resolution. The experiment result will show that this module succeeds in acquiring data with a 104ps resolution, which still makes this implementation an attractive solution for a quasi-real-time STW experiment.

B. Implementation of Memory Banks

For a fast prototyping, Virtex-4 FPGA's on-chip Dual-port Block RAM (BRAM) was implemented to store the ADCs' output. Given a sampling resolution of 216ps, the number of one frame array data is 480x2x16, i.e. 15360, and a total of 240 Kila-Bit BRAM (16-bit per sample, 15360 samples) is required. At first glance, the averaging factor of N will require N times of 240 Kila-Bit BRAM, but the simultaneous Read and Write feature of BRAM allows accumulating the N repetitive samples and only the final summed value will be stored. Virtex-4 chip family has up to 9.9 Mega-Bit BRAM which is sufficient to implement two identical BRAM banks to alternatively store the ADCs' output.

The 240 Kila-Bit BRAM will break into 16 smaller storage units, corresponding to 16 array channel, to allow parallel image processing which will be discussed later. The storage unit (see Figure 7.7) has two smaller-size BRAM elements loading separately the receiver's I and Q data. Port A of BRAM element is configured for writing and Port B only for reading data out. The 16 storage units will share the same set of Write/Read Enable and Address signals, the generation of which needs to be synchronized with the 100MHz sampling clock in Figure 7.6. At the 'Adjust' stage in Figure 7.6, the Write Enable (wea) is set low to disable writing into BRAM. At the 'Collect' stage, ten consecutive Write Address (addra(8:0)) repetitively appear at Port A during each of the N averaging cycle. The Read Clock (clkb) and Read Address (addrb(8:0)) at Port B will replicate those at Port A except being half clock cycle advanced than Port A. The 10 samples at the 1st averaging cycle are loaded to BRAM through Port A at the rising edge of 100MHz Write Clock (clka). From the 2^{nd} to the Nth averaging cycle, before a new sample is loaded to BRAM, the previously saved value will be read out from Port B and ready at A(15:0) port of the 16-bit adder. The adder accumulates the new sample and the previously saved value, and only the sum will be loaded to BRAM. In the end, the sum of N repetitive samples is stored for post-processing.

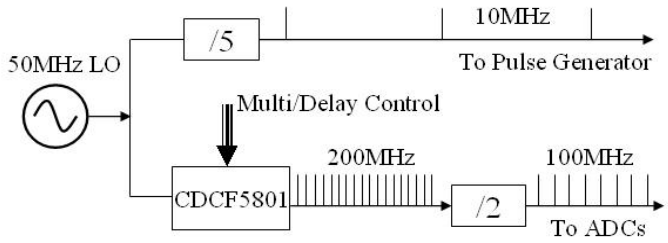

Figure 7.4: Destined and intermediate clocks.

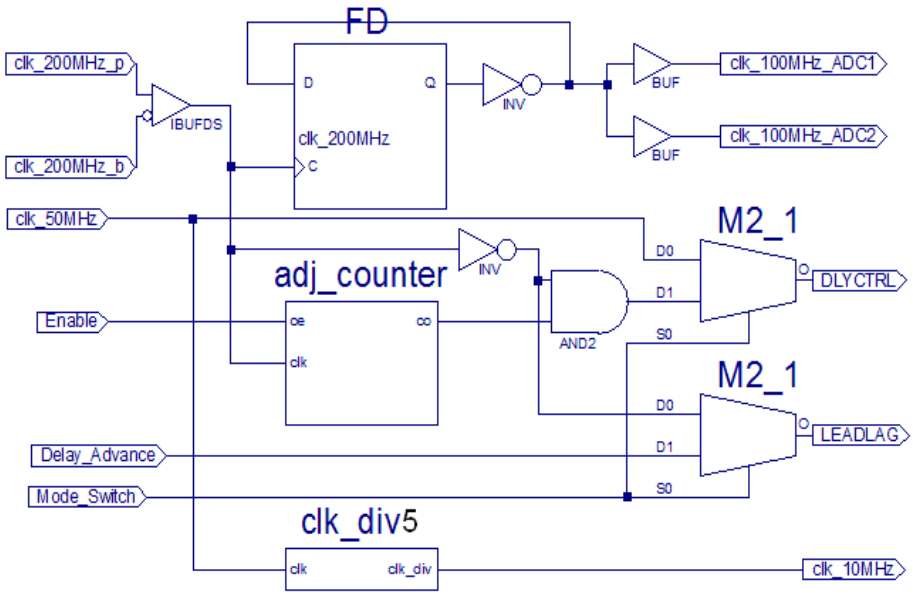

Figure 7.5: Schematic of timing logic.

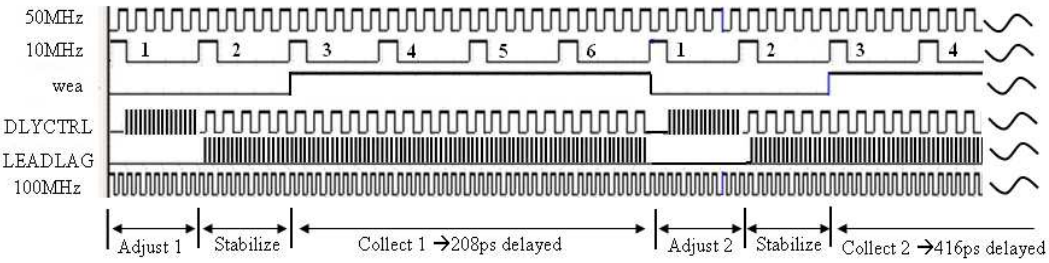

Figure 7.6: Timing sequence.

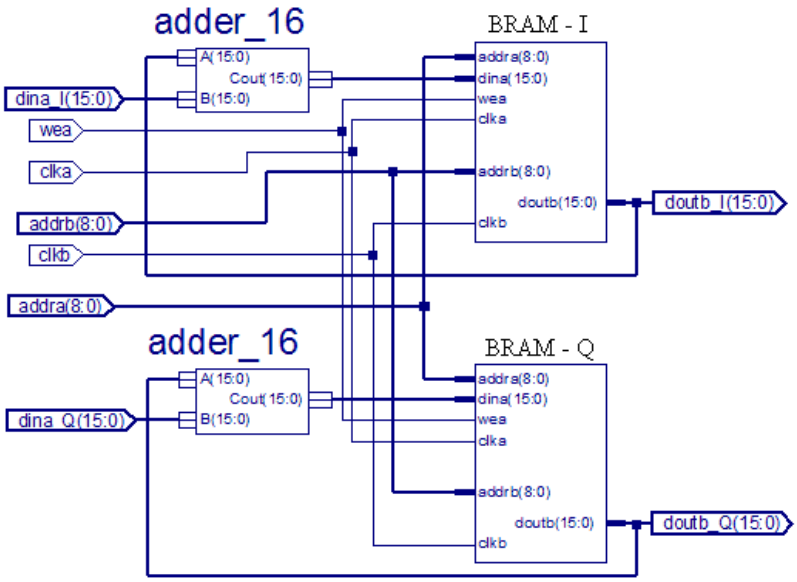

Figure 7.7: Schematic of BRAM storage unit.

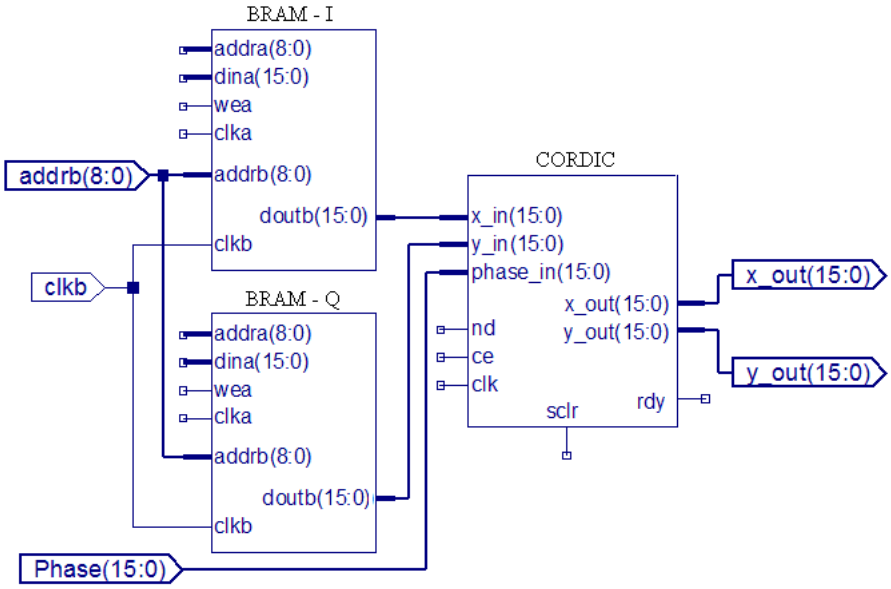

Figure 7.8: Schematic of Beamforming unit.

C. Implementation of Imaging Module

The use of FPGA to perform computationally intensive radar signal processing has been subjected to intensive research [105][106]. In this paper we don't intend to explore the full potential of FPGA in signal processing, but to implement an UWB time-domain beamforming processor to complete the developed STW system for a real-time demonstration. The implemented processor is based on the time-domain sum-and-delay synthetic beamforming method. The time-domain sample of the array signal saved in 16 storage units (see Fig. 12) can be expressed as vectors:

$$s_i(n) = I_i(n) + jQ_i(n)(i = 1,2,...16) \quad \textbf{(7.3)}$$

where $s_i(n)$ is the complex received signal from the array channel "i", $I_i(n)$ is the in-phase signal, and $Q_i(n)$ the quadrature signal. The beamforming is accomplished by mathematically applying the proper phase shifts to the received array signals; the synthetic beam as a function of the time samples is given by:

$$R_j(n) = \sum_{i=1}^{16} s_i(n) e^{j\varphi_{i,j}} (n = 1,2,.....480) \quad \textbf{(7.4)}$$

where $R_j(n)$ is time samples of a beam at the direction θ_j, and $\varphi_{i,j}$ is a phase shift factor based on the beam direction θ_j and the array channels.

The FPGA implementation of an algorithm represented by Eq.(4) is straight-forward. One advantageous feature of FPGA is to allow a fast implementation is the CORDIC (Coordinate Rotation Digital Computer) function, which can be directly invoked from Xilinx ISE Design Environment [107]. Each of the 16 BRAM storage units is followed by a CORDIC element (see Figure 7.8). I and Q samples in BRAMs are read out from Port B as the input to the CORDIC element. The CORDIC rotates the complex input number, x_in + j*y_in by the phase shift represented by phase_in (15:0), and generates the output x_out + j*y_out. The phase rotation occurs in parallel on 16 channels of array data, and the results are summed to generate a single beam represented by Eq.(4). The beams focused at different directions can be formed by varying the value of phase_in(15:0). All valid beam output is stored and will be displayed on an external monitor through one simplified VGA driver, which converts the image data to the color pixel on VGA monitor.

7.4. Real-time Experiment

The whole STW system is shown in Figure 7.9. Clear pictures of each subsystem are plotted in Figure 7.10. Experiments were conducted to evaluate the data acquisition module first. The pulse waveforms measured by a Tektronix TDS7704B real-time oscilloscope and acquired through the developed data acquisition module are compared in Figure 7.11. The oscilloscope is set for 50ps real-time resolution while the acquisition module is configured to have 208ps equivalent-time resolution. The result demonstrates good performance of the module at the least design cost and complexity. One advantage of this FPGA-based approach is that it allows optimizing operating parameters, such as pulse repletion frequency (PRF) and averaging factor, and extending for other related practical system, through FPGA-VHDL software modification.

Therefore the FPGA data acquisition module is configured respectively to have 208ps/sample and 104ps/sample resolutions. The acquired Gaussian pulse waveforms are demonstrated in Figure 7.12. The results show that the custom module successfully catches the pulse shape and the ringing effect. The twisted-pair lines secure a reliable digital link between the ADCs and the FPGA board at a 100MSample/s rate. Higher resolution such as 52ps is achievable through improving the interface connecting the FPGA to the ADC boards.

A full-scale STW experiment is conducted to test the developed real-time system including the microwave front-end and the FPGA imaging module. The experiment is carried in the hallway of an office building. Figure 7.13 shows the whole STW system where a drywall panel is placed in front of the Vivaldi array to simulate the ‘wall’ and one person wanders around. One of the 16 Vivaldi sub-arrays is used as the transmitting antenna; the rest of 15 form a linear receiving array. The trace of the moving person is displayed on the monitor in real time. Figure 7.13(c), the screen shot of the monitor, shows the image of a ‘clean’ experimental scene without the target, which displays the environmental response within a 15 meter distance range and a -30/30 degree azimuth-scanning range at 1 degree angular resolution and 208ps sampling resolution. The strongest response spot at the middle bottom of the image is a result of the direct reflection of the dry wall. Figure 7.14 demonstrates the radar images while the person is moving at a maximum speed of 1.5m/s. Previously in Section V, it is stated that the system’s data acquisition speed is 0.768ms/frame for a 208ps resolution, which should sustain the tracking of targets at a speed much higher than 1.5m/s. However, the 0.768ms/frame acquisition speed is only the signal recording speed. Although the implemented fast sum-and-delay imaging algorithm forms an image within 0.748ms, the refresh rate of a VGA monitor is 60Hz, which only supports updating 60 images per second on the screen and limits the tracking speed. The experiment further reveals that the success of a practical STW system relies on using an efficient image processing.

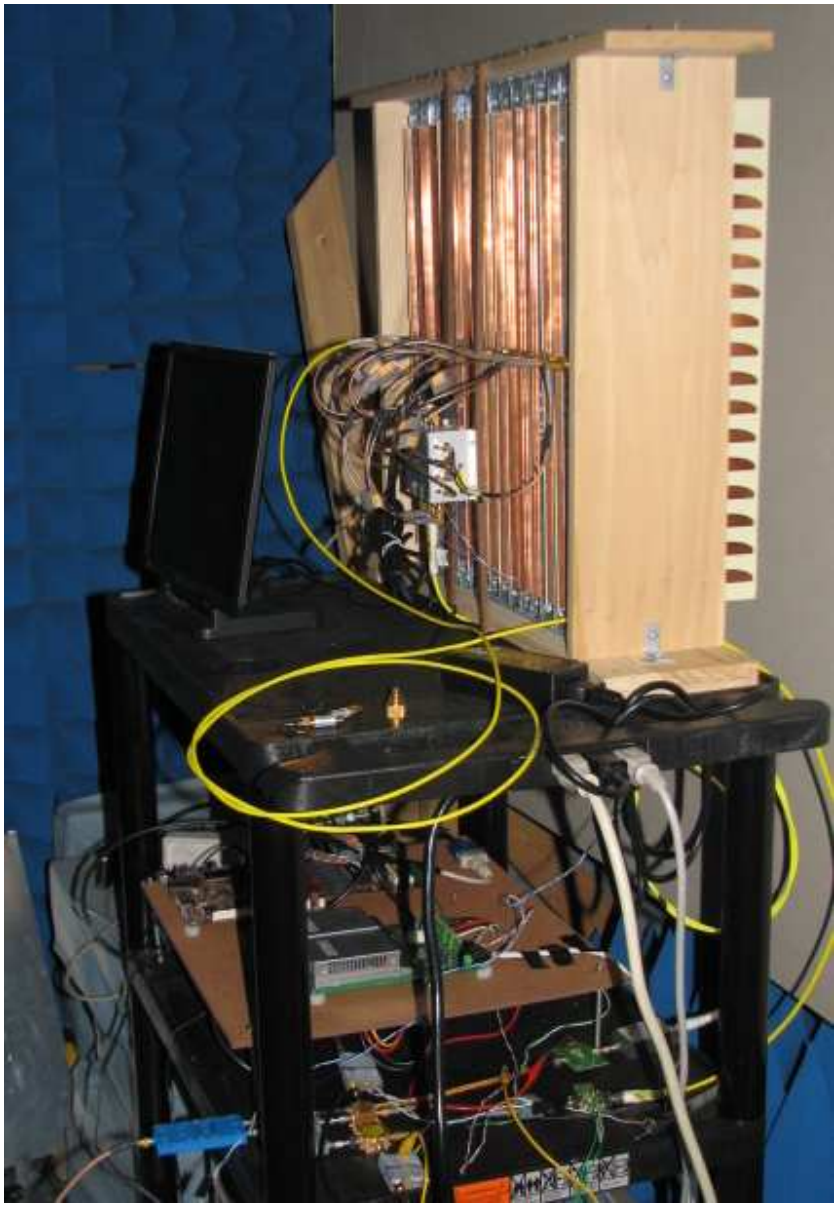

Figure 7.9: Standalone STW System.

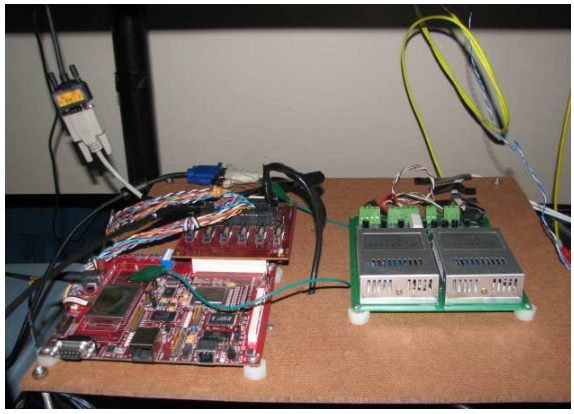

(a) FPGA Board, Avnet Board, and DC Power Supply

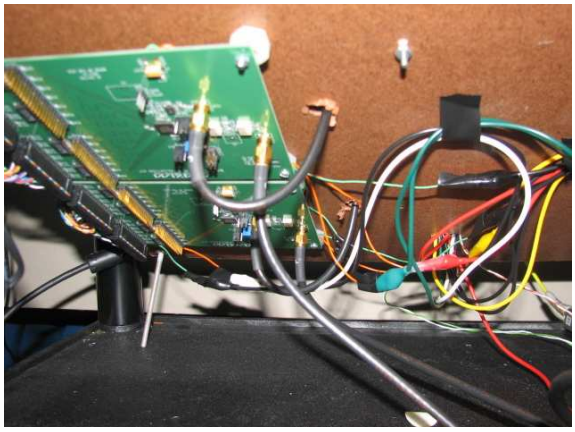

(b) Two Maxim ADC Boards

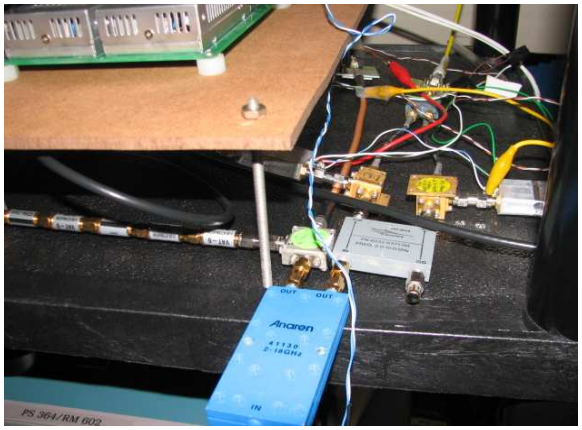

(c) Front-end Transceiver

Figure 7.10: STW Subsystems.

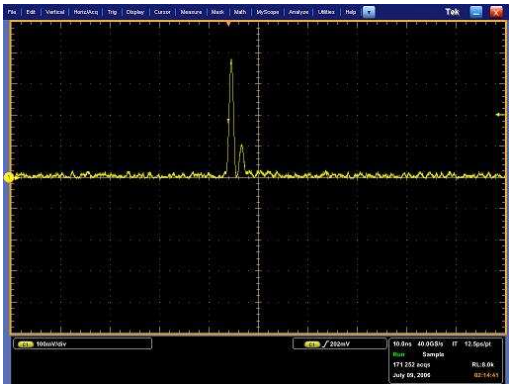

(a) TDS7704B Real-time Oscilloscope Measured Pulse

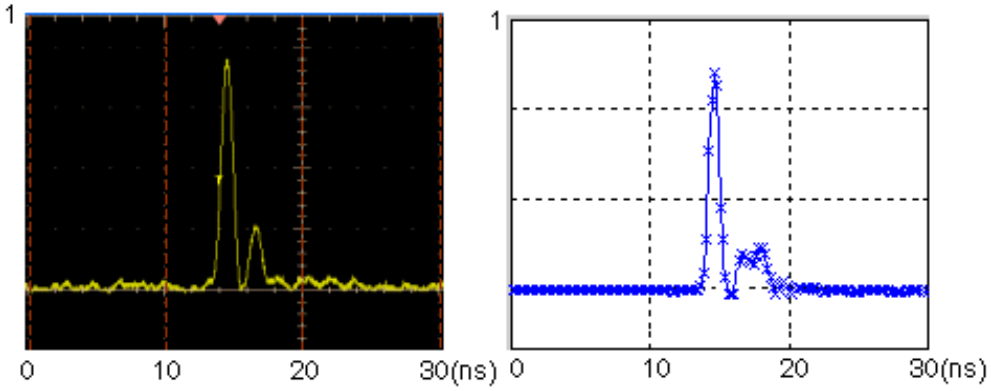

(b) Oscilloscope Result (Zoom In) (c) Data Acquisition Module Result

Figure 7.11: Oscilloscope Measurement Vs. Data Acquistion Module Result.

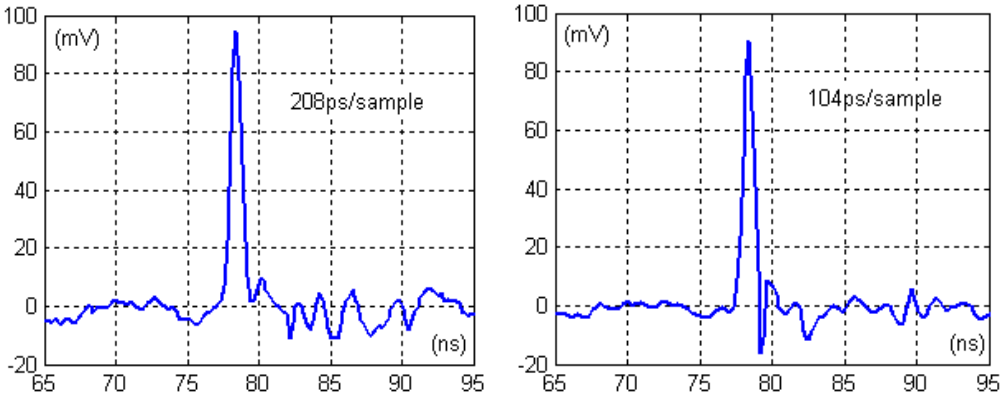

(a) 208ps/sample resolution; (b) 104ps/sample resolution.

Figure 7.12: Comparison of Tested Waveforms.

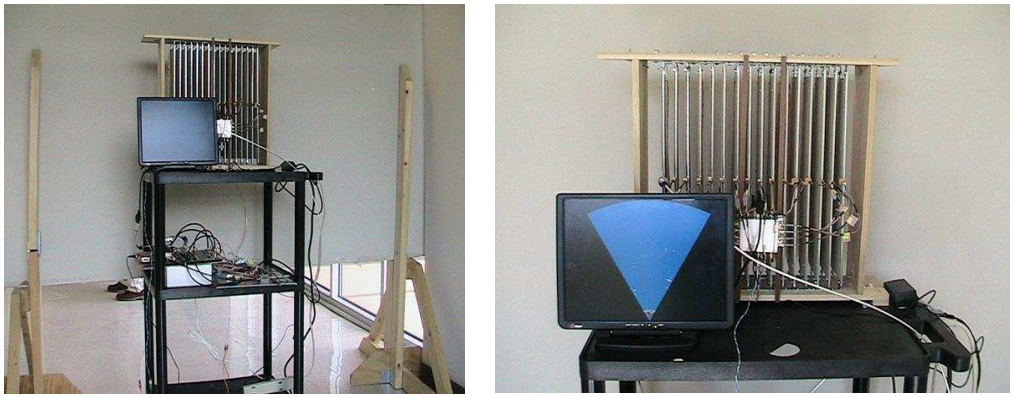

(a) The completed STW system;

(b) Human target;

(c) ‘Clean’ environmental response.

Figure 7.13: Real-time Tracking Experiment.

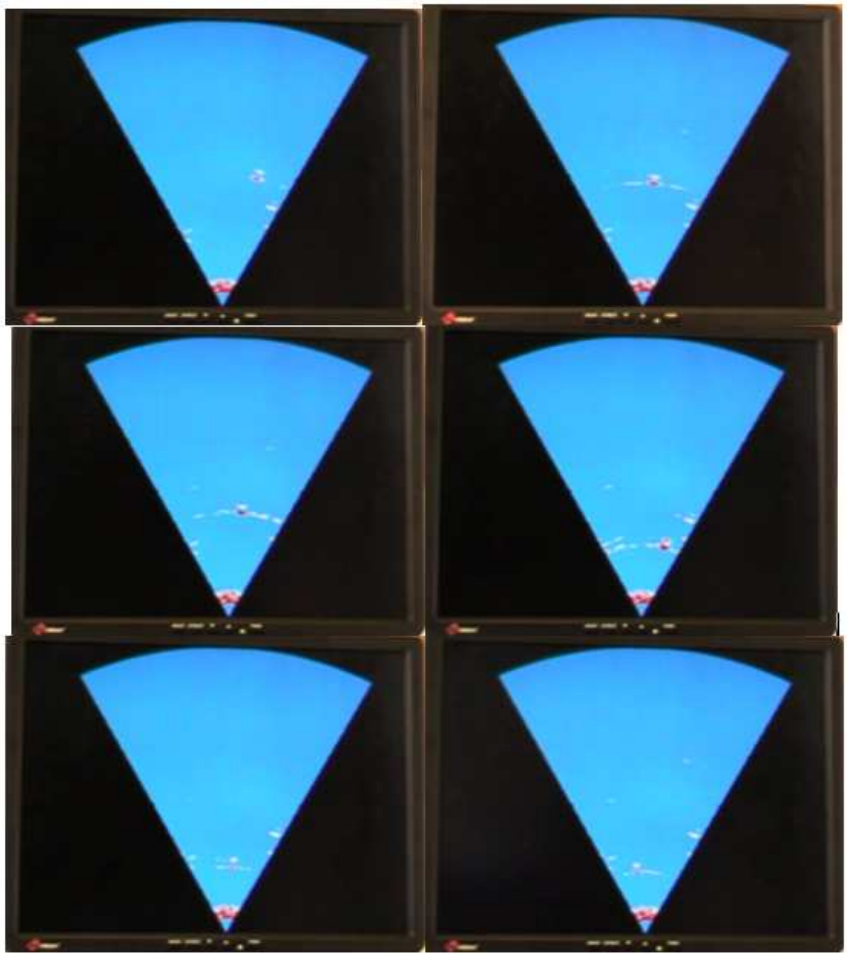

Figure 7.14: Real-time Traces of Moving Target.

For STW studies, it will be more useful to transfer the real-time data from FPGA memory to a PC via the embedded microprocessor for off-line analysis. The experiment was configured to explore such method based on the developed system. In this case, one person stands-still 2m in front of the radar. The received array waveforms are recorded at a 2ms interval during a 4s period. Figure 7.15 compares the 4s recorded signal from one array channel while the person is breathing smoothly (see Figure 7.15 (a)) and holding his breath (see Figure 7.15 (b)). The waveform feature of the 100ns pulse cycle is not visible because of the large time scale, but the overall amplitude of the 4 ns signal clearly reflects the modulation effect of human chest vibrating on the radar signal. The modulation cycle of the recorded signal corresponds to the person's breath rate of 0.5Hz. The mechanism of human breath modulating UWB signal may not be as simple as amplitude modulation; but the phenomenon reveals another approach of STW detection, which is based on the analysis of UWB signal in time/frequency domain instead of generating 2D/3D image. It also shows the potential of the developed system for other real-time UWB applications, such as cardiopulmonary monitoring [108][109].

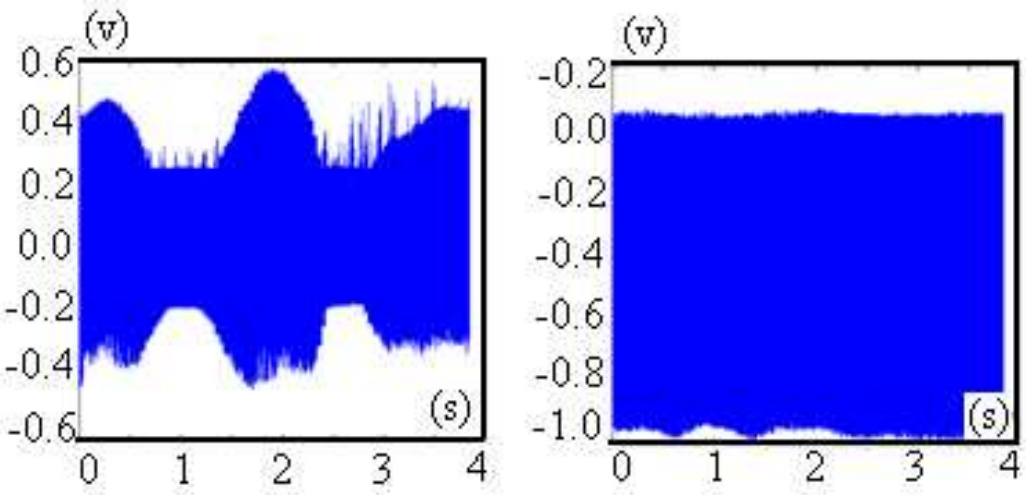

(a) Response of breathing (b) Response of holding breath

Figure 7.15: Comparison of Returned Waveforms from Human.

Chapter 8. SUMMARY AND CONCLUSION

UWB radars are capable of producing high-resolution images by combining the benefits of UWB short pulse technology and those of synthetic arrays. This dissertation reports the development of a real-time standalone STW SAR-based imaging radar system. The development of a standalone STW system could be a challenging task, but the advance of technologies has made it possible to realize one with a reasonable cost and design effort. The design of each subsystem, including the microwave frond-end, the data acquisition module, the system control/process module, and the associated integration issues have been thoroughly studied. For each challenging area which will play a significant role in a final system implementation, such as the STW EM modeling, array design, and wall material characterizations, a solution is put forward and a complete system has been be demonstrated, with the least design effort and difficulty. Off-the-shelf components are used, whenever possible, to shorten the development time and reduce costs associated with a new technology development such as the UWB radar.

The developed system can clearly delineate a number of objects through a wall, and it can also track targets moving behind the walls. Radar images of stationary objects or the room layout have been successfully generated by the developed static or real-time systems. Our current array, for example, displays merely a 2D slice image of the scene in front of the radar, but the system, in principle, could produce a 3D volumetric image with no difficulty by using a scanning antenna array, which will take multiple slices in the other directions.

The current system runs at high center frequency such as 8-10 GHz for higher cross-range resolution which could be for drywalls. But, in a more practical STW environment, concrete walls or brick walls are common building materials. In this case, the system's modular approach and universal automation mechanism should enables easily scaling down the system to the lower center frequency such as 2-4 GHz, which have better RF penetration capability, by replacing a few components in the system. Further more, the system's reconfigurable architecture allows flexible adjustment on various system parameters, such as the pulse repletion rate, the transmitted power, and array deployment and spacing.

A real-time UWB data acquisition network has been proposed and implemented. The data acquisition network is a key subsystem that interfaces between the microwave front-end of UWB system and its post-processing block. It is often the bottle-neck of UWB system design. Digitization of UWB signal normally requires custom design of ADC with intensive wide bandwidth and sampling speed, or using expensive commercial solutions such as real-time oscilloscope. The developed cost-effective data acquisition network uses relatively low-speed ADCs and high performance FGPAs. This design is capable of handling real-time data acquisition process for high-resolution STW imaging or target tracking, and it can be implemented to other UWB applications such as In-door Localization or Medical Imaging/Monitoring.

Extensive EM modeling has been carried out. The modeling study reveals the importance of a design trade-off between the radar parameters/geometry and the achievable resolution. The simulation results are compared and have validated our real data collecting through the developed STW system. The study indicates that a challenging but necessary requirement for STW is the ability to detect and characterize targets through relatively dense and possibly inhomogeneous walls. Critical imaging problems include correcting the defocused images due to dielectric walls between the various targets of interest and eliminating any background clutter caused by complicated room environment. The eventual success of STW technology will depend on the development of effective STW image formation method. The STW community has made some progress in developing advanced STW imaging method. However, the reality of current methods, such as depending on time-consuming iterative algorithm to form image of a simplified/clean STW environment still prevents STW technology from practical field application. The real-time experiment shows that a more practical STW methodology is to distinguish targets behind the wall through their real-time radar signature, rather than to produce an optical-quality image. The developed standalone real-time provides tremendous strength to carry out such study.

In conclusion, progress in this field has been steady and very impressive. However, more work still ahead including developing fast digital processors to handle large data rates, very advanced and fast image processing that can go beyond image recognition to near optical quality ones and to correctly account for the wall presence and blindly estimate its physical parameters. Things are moving fast and we hope in the near future the community at large will be able to deliver real time compact portable systems.

LIST OF REFERENCES

REFERENCES

[1]. "Assessment of ultra-wideband (UWB) technology," Ultra-Wideband Radar Rev. Panel, R-6280, Office of the OSD/DARPA,Washington, DC, July 13, 1990.

[2]. J.D. Taylor, Ultra-wideband Radar Technology, CRC Press LLC, 2001.

[3]. Robert J. Fontana, "A Brief History of UWB Communications," Multispectral Solutions, Inc.

[4]. Dr. Gerald F. Ross, "Early Motivations and History of Ultra Wideband Technology," Anro Engineering, Inc., Lexington, MA.

[5]. Terence W. Barrett, "History of Ultra Wideband (UWB) Radar & Communications: Pioneers and Innovators," UCI, Vienna, VA.

[6]. FCC, "Revision of part 15 of the commission's rules regarding ultra-wideband transmission systems," Notice of inquiry, adopted August 20, 1998, released September 1, 1998.

[7]. FCC, "Revision of part 15 of the commission's rules regarding ultra-wideband transmission systems," Report and order, adopted February 14, 2002, released July 15, 2002.

[8]. Robert J. Fontana, "Recent System Applications of Short-Pulse Ultra-Wideband (UWB) Technology," IEEE Transaction on Microwave Theory and Techniques," Vol. 52, No. 9, September 2004.

[9]. Aitan Ameti, Robert J. Fontana, EJ. Knight & Edward Richley, "Ultra Wideband Technology for Aircraft Wireless Intercommunications Systems (AWICS) Design," IEEE 2004.

[10]. Stanley E. Borek, "An Overview of Through the Wall Surveillance for Homeland Security," IEEE Proceedings of the 34th Applied Imagery and Pattern Recognition Workshop, 2005.

[11]. G. Barrie, "UWB Impulse Radar Characterization and Processing Techniques," Defense R&D Canada - Ottawa, Dec 2004.

[12]. S. Foo, A. Walsh, S. Kashyap, "Ultra-Wideband **(**UWB**)** Remote Sensing and Radar Imaging," Defense R&D Canada - Ottawa, May 2004.

[13]. Gauthier, S.; Hung, E.; Chamma, "Surveillance Through Concrete Walls," Defence R&D Canada - Ottawa, December 2003.

[14]. J. Boutros, G. Barrie, "Ultra-Wideband Synthetic Aperture Radar Imaging. Effect of Off-Track Motion on Resolution," Defense R&D Canada - Ottawa, November 2003.

[15]. G. Barrie, J.K.E. Tunaley, "An Analysis of Through- and In-the-Wall **UWB** Impulse Radar. Systems Design Considerations," Defense R&D Canada - Ottawa, September 2003.

[16]. Comlab Inc., "Ultra-Wideband Radar Through-Wall Measurement," Defense R&D Canada Report, June 2003.

[17]. R. Robinson, “Through the Wall Ultra Wideband Radar. An Investigation into the Feasibility of Building an In-House UWB Radar Hardware Capability,” Defense R&D Canada - Ottawa, March 2003.

[18]. F. AHMAD, M. G. AMIN, S. A. KASSAM, “Synthetic Aperture Beamformer for Imaging Through a Dielectric Wall,” IEEE Transaction on Aerospace and Electronics Systems, Vol. 41, No. 1, January 2005.

[19]. L. Song, C. Yu, Q.H. Liu, “Through-Wall Imaging (TWI) by Radar: 2-D Tomographic Results and Analysis,” IEEE Transaction on Geoscience and Remote Sensing, Vol.43, No.12, December 2005.

[20]. G. Wang and M. G. Amin, “Imaging Through Unknown Walls Using Different Standoff Distances,” IEEE Transaction on Signal Processing, Vol. 54, No. 10, October 2006.

[21]. J. McVay et al., “Through-the-Wall “Imaging and Sensing: An Electromagnetic Perspective,” SAFE 2007 Workshop, IEEE Signal Processing Society.

[22]. F.C. Chen, W.C. Chew, “Time-domain ultra-wideband microwave imaging radar system,” *in Proc. Instrumentation and Measurement Technology Conference*, Vol. 1, May 1998, pp:648 – 650.

[23]. A.Vertiy, *S.* P. Gavrilov, V. N. Stepanyuk, and I.V. Vaynovsky, “Through-Wall Microwave Tomography Imaging,” AP Society International Symposium, 2004, Vol.3, pp:3087-3090.

[24]. Y. Yang, C. Zhang, and A.E. Fathy, “Development and Implementation of Ultra-wideband See-Through-Wall Imaging System Based on Sampling Oscilloscope,” *Antenna and Wireless Propagation letter*, to be published.

[25]. R. Dilsavora, W. Ailesb, P. Rushc, F. Ahmadd, W. Keichela, G. Titie, and M. Amin, “Experiments on Wideband Through the Wall Imaging,” *Proceeding of SPIE*, Vol. 5808, pp. 196-209, May 2005.

[26]. I.I. Immoreeve and D.V. Fedotov, "Ultra wideband radar systems: advantages and disadvantages", in Proc. IEEE Ultra Wideband Systems and Technologies Conf, Baltimore, MD, May 2002, pp.201-205.

[27]. T. Sakamoto, Nonparametric Imaging Algorithms for UWB Pulse Radar, Ph.D. Dissertation

[28]. A. Franchois, and C. Pichot, “Microwave imaging – Complex Permittivity Reconstruction with a Levenberg-Marquardt Method,” IEEE Trans. on Antenna Propogation, Vol.45, No.2, pp. 203-215, 1997.

[29]. A.J. Devaney, “Geophysical Diffraction Tomography,” IEEE Trans. Geosci. Remote Sensing, Vol.22, No.1, pp.3-13, 1984.

[30]. C. Pichot, L.Jofre, G. Peronnet, and J.C. Bolomey, “Active Microwave Imaging of Inhomogeneous Bodies,” IEEE Trans. on Antennas Propagation, Vol.33, No.4, pp.416-425, 1985.

[31]. T.J. Cui, and W.C. Chew, "Diffraction Tomographic Algorithm for the Detection of Three-dimensional Objects Buried in a Lossy Half Space," IEEE Trans. on Antennas Propagation, Vol.52, No.6, pp.1398-1411, 2004.

[32]. K. Sato, T. Manabe, J. Polivka, T. Ihara, Y. Kasashima, K. Yamaki, "Measurement of the Complex Refractive Index of Concrete at 57.5 GHz," IEEE Transaction on Antennas and Propagation, Vol. 44, Issue 1, pp.35 – 40, January 1996.

[33]. G.J. Zhang, Synthetic Aperture Radar Imaging of Embedded Objects in Dielectric Slabs, Ph.D. Thesis, Iowa State University, 1998

[34]. J.E. Mast and E.M. Johansson, "Three-dimensional Ground Penetrating Radar Imaging Using Multi-frequency Diffraction Tomography," in SPIE Proceedings on Advanced Microwave and Millimeter Wave Detectors, vol. 2275, July 1994.

[35]. O. Buyukozturk, "Imaging of Concrete Structure," NDT&E International, vol. 31, no. 4, pp. 233-243, 1998.

[36]. S. Valle, L. Zanzi, and F. Rocca, "Radar Tomography for NDT: Comparison of techniques," Journal of Applied Geophysics, vol.41, pp. 259-269, 1999.

[37]. D.J. Blejer, C.E. Frost, and S.M. Scarborough, "Three-dimensional UHF and L-band SAR Imaging for Building Penetration," (Technical Note, MIT Lincoln Laboratory, Lexington, Massachussets.

[38]. L. Cai and E.K. Walton, "Theoretical and Experimental Studies of Hand-held SAR concept," Technical Report 734545-1, The Ohio State University Electro Science Laboratory, Department of Electrical and Computer Engineering, September 1998.

[39]. Proceedings of SPIE -- Volume 6201 Sensors, and Command, Control, Communications, and Intelligence (C3I) Technologies for Homeland Security and Homeland Defense V, Edward M. Carapezza, Editor, 62010J (May. 10, 2006).

[40]. *Synthetic Aperture Radar Signal Processing with Matlab Algorithm*, Mehrdad Soumekh, Wiley-Interscience Publication, 1999.

[41]. Yan Zhao, Yang Hao, and Clive Parini, "Two Novel FDTD Based UWB Indoor Propagation Models,"

[42]. Traian Dogaru and Calvin Le, "Numeric Simulation for Sensing Through the Wall Radar," U. S. Army Research Laboratory.

[43]. Kaveh Heidary, "Scattering from an Infinite Conducting Cylinder Covered with a Finite Two-Layer Dielectric Coating (Modal Approach)," IEEE Transaction on Electromagnetic Compatibility, Vol. 38, No. 1, February 1996.

[44]. Kaveh Heidary, "Ultra-Wideband (UWB) Incidence on Multiple Dielectric Interfaces," 2004 IEEE.

[45]. Kaveh Heidary, "A Physical Scattering Model for the Ultra-Wideband (UWB) Propagation Channel," 2005 IEEE.

[46]. M. Ghaddar, L. Talbi and T.A. Denidni, “Human Body Modeling for Prediction of Effect of People on Indoor Propagation Channel,” Electronics Letters, Vol. 40, No. 25, December 2004.

[47]. Traian Dogaru and Calvin Le, “Numeric Simulation for Sensing Through the Wall Radar,” U. S. Army Research Laboratory.

[48]. H.-R. Chuang, “Numerical Computation of Fat Layer Effects on Microwave Near-Field Radiation to the Abdomen of a Full-Scale Human Body Model,” IEEE Transaction on Microwave Theory and Techniques, Vol. 45, No. 1, January 1997.

[49]. CFDTD Manuel, http://www.ecl.ee.psu.edu/ecl/computersoftware.html

[50]. *Advanced Engineering Electromagnetics*, Constantine A. Balanis, Published by Wiley, 1989.

[51]. H.K. Chung and H.L. Bertoni, "Indoor Propagation Characteristics at 5.2 GHz in Home and Office Environments," Journal of Communication and Networks; Vol. 4; No. 3; pp. 176-188, 2002.

[52]. N.C. Currie, D.D. Ferris, and al, “New Law Enforcement Application of Millimeter Wave Radar”, SPIE Vol. 3066, pp2-10, 1997.

[53]. Lawrence M. Frazier, “Radar Surveillance through Solid Materials,” SPIE Photonics East Conference, November 1996.

[54]. S. Stavrou and S.R. Saunders, “Review of Constitutive Parameters of Building Materials,” University of Surrey, United Kingdom.

[55]. A. Muqaibel, A. Safaai-Jazi, and etc., “Ultrawideband Through-The-Wall Propagation,” IEE Proc.-Microwave. Antennas Propagation, Vol. 152, No. 6, December 2005.

[56]. K. Y. Yazdandoost and R. Kohno, “Complex Permittivity Determination of Material for Indoor Propagation in Ultra-Wideband Communication Frequency,” International Symposium on Communications and Information Technologies, Sapporo, Jap, October 2004

[57]. A. Muqaibel, A. Safaai-Jazi, A. Bayram, and S. M. Ftiad, “Ultra Wideband Material Characterization for Indoor Propagation,” IEEE 2003.

[58]. J.L.Frolik, “Time-domain Techniques for Reconstructing Lossy Layered Media from One-sided Scattering,” IEEE 1999.

[59]. Yi Huang and David Parsons, “A Time Domain Approach for Measuring the Dielectric Properties and Thickness of Walls of a Building,” University of Liverpool.

[60]. A.Vertly, S. P. Gavrilov, V. N. Stepanyuk, and I.V. Vaynovsky, “Through-Wall Microwave Tomography Imaging,” 2004 IEEE.

[61]. I. CUIÑAS and M. G. SÁNCHEZ, “Permittivity and Conductivity Measurements of Building Materials at 5.8 GHz and 41.5 GHz,” Wireless Personal Communications, © 2002 Kluwer Academic Publishers.

[62]. Ahmad Safaai-Jazi, Sedki M. Riad, Ali Muqaibel, and Ahmet Bayram, "Ultra-wideband Propagation Measurements and Channel Modeling," DARPA NETEX Program Report, November, 2002

[63]. K. Sato, T. Manabe, and etc., "Measurements of Reflection and Transmission Characteristics of Interior Structures of Office Building in the 60-GHz Band," IEEE Transaction on Antenna and Propagation, Vol. 45, No. 12, December 1997.

[64]. R.L. Chufo, "an Electromagnetic Noncontacting Sensor for Thickness Measurement in a Dispersive Media," U.S. Bureau of Mines, Pittsburgh, Pennsylvania

[65]. Jietao Zhang, and etc., "Electromagnetic imaging of layered building materials," Meas. Sci. Technol. 12, pp. 1147-1152, 2001.

[66]. K. Sato, T. Manabe, J. Polivka, T. Ihara, Y. Kasashima, K. Yamaki, "Measurement of the complex refractive index of concrete at 57.5 GHz," IEEE Transaction on Antennas and Propagation, Vol. 44, Issue 1, pp.35 – 40, January 1996.

[67]. Y. Yang, Z. Wang, A.E. Fathy, "Design of Compact Vivaldi Antenna Arrays for UWB See Through Wall Applications," Progress in Electromagnetics Research, PIER 82, 2008, pp: 401-418.

[68]. "Development of an Ultra Wideband Vivaldi Antenna Array", Y. Yang, A. Fathy, IEEE AP-S International Symposium on Antennas and Propagation, Washington DC, July 2005.

[69]. J.A. McVay, K.M. Yemelyanov, A. Hoorfar, N. Engheta, "Through-the-Wall Imaging and Sensing: An Electromagnetic Perspective," IEEE Workshop on Signal Processing Applications for Public Security and Forensics, April 2007, pp:1 – 4.

[70]. P.J. Gibson, "The Vivaldi Aerial", in Proc. 9th Eur. Microwave Conf., June 1979.

[71]. R. Janaswamy and D.H. Schaubert, "Analysis of the Tapered Slot Antenna," IEEE Trans. Antennas Propagat., vol. AP-35, pp. 1058–1064, Sept. 1987.

[72]. B. Stockbroeckx and A.V. Vorst, "Copolar and Cross-polar Radiation of Vivaldi Antenna on Dielectric Substrate," IEEE Trans. Antennas Propagat., vol. 48, pp. 19–25, Jan. 2000.

[73]. M.C. Greenberg, L. Virga, and C.L. Hammond, "Performance Characteristics of the Dual Exponentially Tapered Slot Antenna for Wireless Communication Application", IEEE Trans. on Vehicular Technology, vol. 52, pp. 305–310, Mar. 2003.

[74]. S.G. Kim, and K. Chang, "Ultra Wideband 8 to 40 GHz Beam Scanning Phased Array Using Antipodal Exponentially-tapered Slot Antennas", IEEE MTT-S Digest, pp. 1757-1760, 2004.

[75]. E.Ehud Gazit, "Improved Design of the Vivaldi Antenna," Proc. Inst. Elect. Eng., pt. H, vol. 135, no. 2, pp. 89–92, Apr. 1988.

[76]. D. H. Schaubert and T.-H.Tan-Huat Choi, "Wideband Vivaldi Arrays for Large Aperture Antennas," Perspectives on Radio Astronomy: Technologies for Large Antenna Array, pp. 49–58, 1999.

[77]. J. D. S. Langley, P. S. Hall, and P. Newham, "Balanced Antipodal Vivaldi Antenna for Wide Bandwidth Phased Arrays," in Proc. IEEE Antennas Propagation, vol. 143, Apr. 1996, pp. 97–102.

[78]. Electromagnetic Waves and Antennas, Sophocles J. Orfanidis, Rutgers University.

[79]. HMC347LP3 Data Sheet, www.hittite.com

[80]. R. Dilsavora, W. Ailesb, P. Rushc, F. Ahmadd, W. Keichela, G. Titie, and M. Amind, "Experiments on Wideband Through the Wall Imaging," Proceeding of SPIE, Vol. 5808, pp. 196-209, May 2005.

[81]. Y. Yang and A.E. Fathy, "See-through-wall Imaging Using Ultra Wideband Short-pulse Radar System," Antennas and Propagation Society International Symposium, 2005 IEEE, Volume 3B, pp.334 – 3373, July 2005.

[82]. J. L. Moll et al., "Physical Modeling of the Step Recovery Diode for Pulse and Harmonic Generation Circuits," in Proc. IEEE, vol. 57, pp. 1250–1259, July 1969.

[83]. J.S. Lee and C. Nguyen, "Uniplanar Picosecond Pulse Generator Using Step-Recovery Diode," in Electronics Letters, Vol. 37, Issue 8, Apr 2001, pp. 504 – 506.

[84]. J.W. Han and C. Nguyen, "Ultra-wideband Electronically Tunable Pulse Generators" in IEEE Microwave and Wireless Components Letters, Vol. 14,Issue 3, March 2004, pp. 112 – 114.

[85]. J.W. Han and C. Nguyen, "A New Ultra Wideband, Ultra-short Monocycle Pulse Generator with Reduced Ringing," in IEEE Microwave and Wireless Components Letters, Vol. 12, No. 6, June 2002, pp. 206–208.

[86]. C. Zhang and A.E. Fathy, "Reconfigurable Pico-Pulse Generator for UWB Applications," Microwave Symposium Digest, 2006, June 2006, pp. 407-410.

[87]. Oscilloscope Analysis and Connectivity Made easy, www.tek.com

[88]. www.mathworks.com

[89]. Agilent Advanced Design System, available: http://www.agilent.com

[90]. Ahmad Safaai-Jazi, Sedki M. Riad, Ali Muqaibel, and Ahmet Bayram, "Ultra-wideband Propagation Measurements and Channel Modeling," DARPA NETEX Program Report, November, 2002

[91]. Traian Dogaru and Calvin Le, "Numerical Simulation for Sensing Through the Wall Radar," U. S. Army Research Laboratory.

[92]. 8-bit cPCI Digitizers Datasheet, available: http://acqiris.tm.agilent.com/

[93]. Tektronix CSA7404B Oscilloscope, available: http://www.tek.com/

[94]. Mark Kahrs, "50 Years of RF and Microwave Sampling," IEEE Transaction on Microwave Theory and Techniques, Vol. 51, No. 6, June 2003.

[95]. L. Ting, R. Woods, C. Cowan, "Virtex FPGA Implementation of a Pipelined Adaptive LMS Predictor for Electronic Support Measures Receivers," IEEE Trans. on VLSI Systems, Vol.13, No.1, Jan. 2005.

[96]. D. Nguyen, D. Halupka, P. Aarabi, and A. Sheikholeslami, "Real-Time Face Detection and Lip Feature Extraction Using Field-Programmable Gate Arrays," IEEE Trans. on Systems, Man, and Cybernetics – Part B: Cybernetics, Vol.36, No.4, Aug. 2006.

[97]. P. Dillinger, J.F. Vogelbruch, J. Leinen, S. Suslov, R. Patzak, H. Winkler, and K. Schwan, "FPGA-Based Real-Time Image Segmentation for Medical Systems and Data Processing," IEEE Trans. on Nuclear Science, Vol.53, No.4, Aug. 2006.

[98]. Maxim Max108 ADC datasheet, available: http://www.maxim-ic.com/

[99]. Avnet Vertex-4 Evaluation Board datasheet, Avnet AvBus Breakout Module datasheet, available: http://www.avnet.com/

[100]. CDC5801 Datasheet, available: http://www.avnet.com/

[101]. Reinhard Stolle, "Electromagnetic Coupling of Twisted Pair Cables," IEEE Journal on Selected Areas in Communications, Vol.20, No.5, June 2002.

[102]. J. R. Armstrong, F.G. Gray, M.W. Lin, "VHDL Modeling and Model Testing for DSP Applications," IEEE Trans. on Industrial Electronics, Vol.46, No.1, Feb. 1999.

[103]. M.A. Fischman, A.C. Berkun, W. Chun, E. Im, "An Onboard Processor and Adaptive Scanning Controller for the Second-Generation Precipitation Radar," IEEE Trans. on Geoscience and Remote Sensing, Vol.45, No.4, April 2005.

[104]. D. Morche, F. Hameau, D. Lachartre, G. Masson, C. Mounet, M. Pelissier, D. Helal, L. Smaini, D. Belot, "Digital Radio Front-End for High Data Rate Impulse UWB System," Proceedings, IEEE International Conf. on Electronics, Circuits and System, Dec. 2006, pp: 788 – 791.

[105]. B.G. Tomov and J.A. Jensen, "Compact FPGA-Based Beamformer Using Oversampled 1-bit A/D Converters," IEEE Trans. on Ultrasonics, Ferroelectrics, and Frequency Control, Vol.52, No.5, May 2005.

[106]. M.A. Fischman, C. Le, and P.A. Rosen, "A digital beamforming processor for the joint DoD/NASA space based radar mission," Proceedings, IEEE Radar Conf., April 2004, pp:9-14.

[107]. CORDIC v3.0 Data Sheet, available: http://www.xilinx.com/

[108]. A.D. Droitcour, O. Boric-Lubecke, V.M. Lubecke, J. Lin, and G.T.A. Kovacs, "Range Correlation and I/Q Performance Benefits in Single-Chip Silicon Doppler Radars for Noncontact Cardiopulmonary Monitoring," IEEE Trans. on Microwave Theory and Techniques, Vol.52, No.3, March 2004.

[109]. Y. Xiao, C. Li, J. Lin "A Portable Non-Contact Heartbeat and Respiration Monitoring System Using 5-GHz Radar," IEEE Sensors Journal, Vol.7, No.7, July 2007.

[110]. Magdy F. Iskander, Zhengqing Yun, and R. Quintero-Illera, "Polarization and Human Body Effects on the Microwave Absorption in a Human Head Exposed to Radiation from Handheld Devices," IEEE Transaction on Microwave Theory and Techniques, Vol. 48, No. 1, November 2000.

[111]. Naoyuiki Yamada, "Radar Cross Section for Pedestrian in 76 GHz Band," R&D Review of Toyota CRDL VOL 39. No.4.

[112]. Andrew Fort, "Ultra-Wideband Channel Model for Communication Around the Human Body," IEEE Journal on Selected Areas in Communication, Vol. 24, No. 4, April 2006.

[113]. DEVEND MISRA, AND KUN-MU CHEN, "Responses of Electric-Field Probes Near a Cylindrical Model of the Human Body," IEEE Transaction on Microwave Theory and Techniques, Vol. MTT-33, No. 6, June 1985.

[114]. King Wai Lam, Qin Li, and etc., "On the Analysis of Statistical Distributions of UWB Signal Scattering by Random Rough Surfaces Based on Monte Carlo Simulations of Maxwell Equations," IEEE Transactions on Antennas and Propagation, Vol. 52, No. 12, December 2004.

PUBLICATIONS

1 **Development and Implementation of a Real-Time See-Through-Wall Radar System Based on FPGA**, Y. Yang and A. Fathy, IEEE Transactions on Geoscience and Remote Sensing, 2008, Submitted and under revision.

2. **Development and Implementation of Ultra-wideband See-Through-Wall Imaging System Based on Sampling Oscilloscope**, Y. Yang, C. Zhang, and A.E. Fathy, IEEE Antenna and Wireless Propagation letter, accepted and to be published, 2008.

3. **Design of Compact Vivaldi Antenna Arrays for UWB See Through Wall Applications**, Y. Yang, Z. Wang, A.E. Fathy, Progress in Electromagnetics Research, PIER 82, 2008, pp: 401-418.

4. **Real-time See Thru-wall Imaging System**, Conference Abstract, Y. Yang, S. Liu, and A. Fathy, Conference Abstract, IEEE Signal Processing Society SAFE 2007

5. **Design and Implementation of a Low-Cost Real-Time Ultra-Wide Band See-Through-Wall Imaging Radar System**, Y. Yang, A. Fathy, Proceeding, IEEE MTT-S International Microwave Symposium, Honolulu, Hawaii, June 2007.

6. **FPGA-based Data Acquisition and Beamforming System For UWB See-Through-Wall Imaging Radar**, Y. Yang, J. Wang, S. Liu, M. Mahfouz, A.E. Fathy, Conference Abstract, IEEE AP-S / URSI / AMEREM Symposium, Albuquerque, New Mexico, July, 2006

7. **Development of an Ultra Wideband Vivaldi Antenna Array, Y. Yang, A. Fathy, Proceeding**, IEEE AP-S International Symposium on Antennas and Propagation, Washington DC, July 2005.

8. **See-Through-Wall Imaging Using Ultra Wideband Short-Pulse Radar System**, Y. Yang, A. Fathy, Proceeding, IEEE AP-S International Symposium on Antennas and Propagation, Washington DC, July 2005.

9. **Development of SAR-Based UWB See Through Wall Radar System**, Y. Yang, A. Fathy, See Through Wall Workshop, IEEE MTT-S International Microwave Symposium, Long Beach, CA, June 2005.

10. **See-Through-Wall Imaging using Ultra Wideband Pulse Systems**, M. Mahfouz, A. Fathy, Y. Yang, E. E. Ali, A. Badawi, 34th Applied Image Pattern Recognition Workshop, IEEE Computer Society, Washington DC, October 2005.

11. **A Novel Uniplanar Subharmonic Mixer for Near Baseband UWB Applications**, S. Lin, Y. Yang , A.Fathy, Conference Abstract, 2006 National Radio Science Meeting.

12. **Time-resolved Measurements of Electron Number Density and Collision Frequency for a Fluorescent Lamp Plasma Using Microwave Diagnostics**, M. Howlader, Y. Yang, J.R. Roth, IEEE Transaction on Plasma Science, Vol. 33, Issue: 3, pp: 1093- 1099, June 2005.

APPENDIX

APPENDIX 1: ACCELERATING 3D STW ELECTROMAGNETIC MODELING

As previously discussed in Chapter 3, running an exact electromagnetic model of an entire building or even a single room in the microwave frequency range via a full wave method such as Finite Difference Time Domain method is a very computationally intensive task. One alternative method is to employ an approximate solver, which utilizes the shooting and bouncing ray technique together with physical optics. **Xpatch** is such an approximate solver is capable of obtaining a fast solution with reasonable accuracy. It is developed by Science Applications International Corporation (SAIC) for predicting and analyzing realistic far-field and near-field high-frequency radar signatures for 3D target models. It has been used by U.S. Army Research Laboratory for STW human body signature study and generates fairly accurate result compared to full-wave FDTD method.

The second approach to accelerate STW electromagnetic modeling is to fully utilize FDTD method's parallel processing capability. **XFdtd** is a full wave electromagnetic solver based on FDTD, developed by Remcom Inc. It offers unique capabilities including Fast Meshing Algorithm, a wide variety of complex electric and magnetic materials including nonlinear and frequency-dependent, and many others. It is a domain solver which allows large problems to utilize the full capability of computer clusters. It supports Remcom's XStream® hardware FDTD for extremely fast calculations using the graphics processing units in high speed video cards.

The third approach, but not the last, is using ray-tracing-based tool such as Remcom's **Wireless InSite** package. Wireless InSite is a tool for modeling the effects of buildings and terrain on the propagation of electro-magnetic waves. It predicts how the locations of transmitters and receivers within an urban area affect the signal strength in a single or multi-room with complex environment. Although the pure ray-tracing-based might not provide as accurate result as the previous two methods, one may still obtain fast physics-based path loss predictions which might shed some useful insight on STW development.

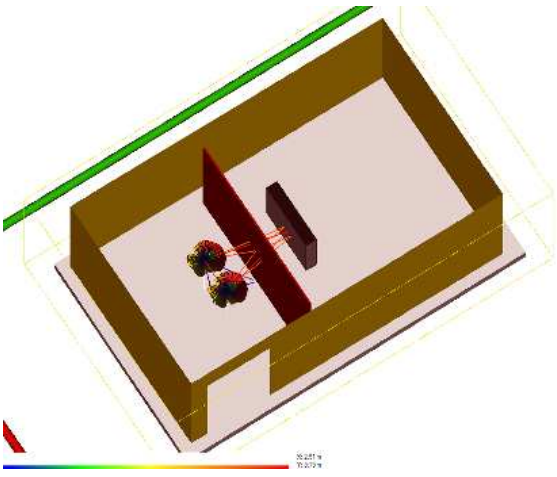

Figure A1: Wireless Inside Model.

APPENDIX 2: DC POWER SUPPLY DESIGN SCHEMATICS

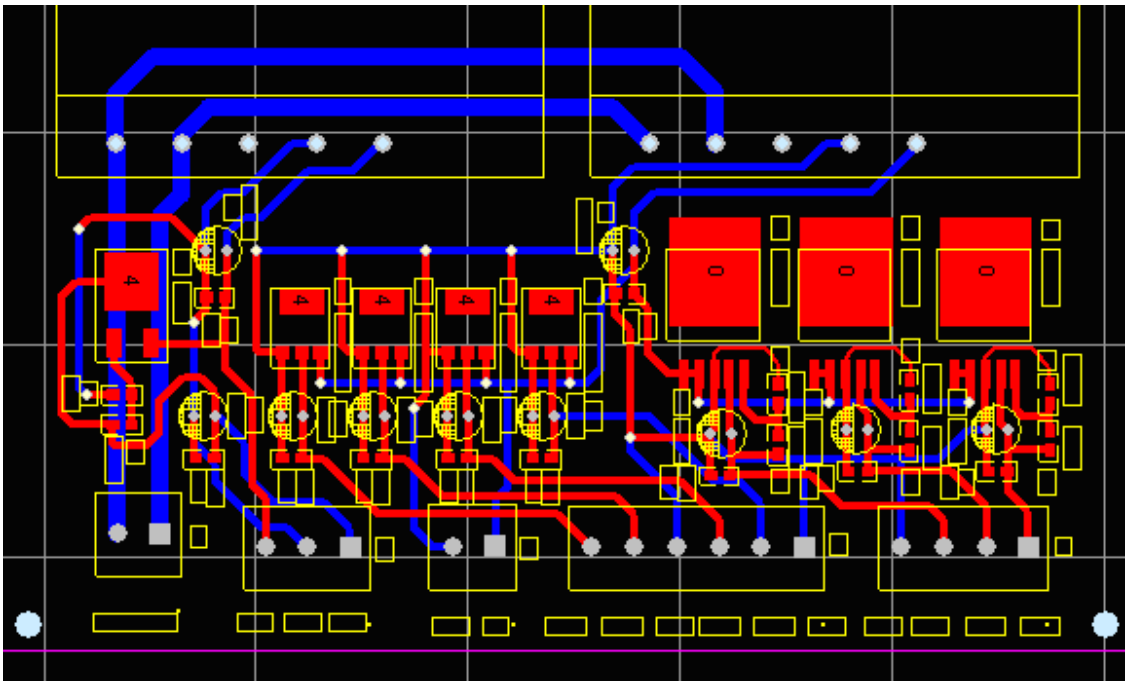

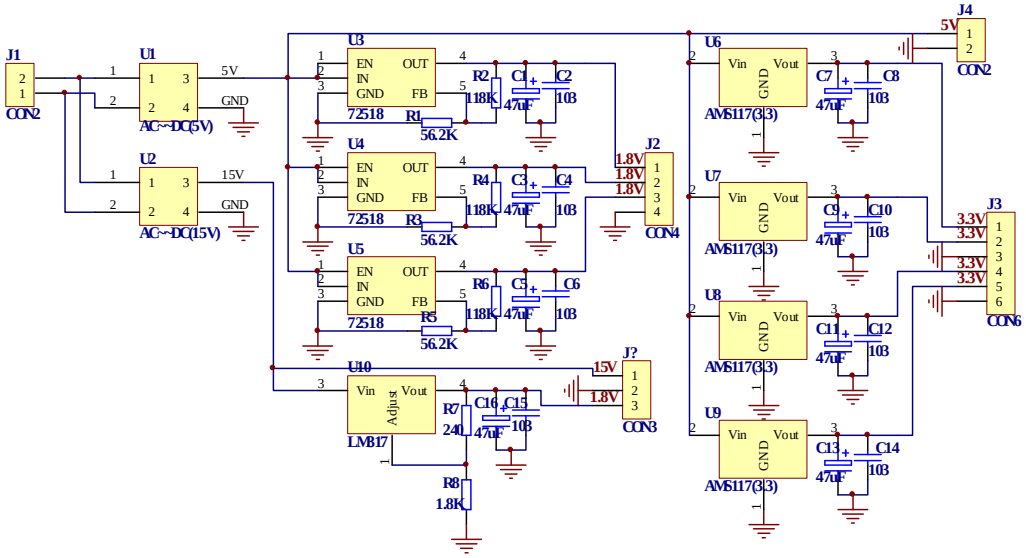

APPENDIX 3: INSTRUMENTS FOR UWB TIME DOMAIN UWB STW EXPERIMENT

	Sampling Oscilloscope	Sampling Oscilloscope	Real Time Oscilloscope	Real Time Oscilloscope	Real Time Oscilloscope	Real Time Oscilloscope	Real Time Oscilloscope
Model	TDS8200+ 80E04 **(Tektronix)**	86100C+ 86112A **(Agilent)**	TDS7704B **(Tektronix)**	TDS6804B **(Tektronix)**	TDS6604B **(Tektronix)**	Infiniium 54854A **(Agilent)**	Infiniium 54855A **(Agilent)**
Input Channel	2	2	4	4	4	4	4
Analog Bandwidth	20 GHz	20 GHz	7.25 GHz	7 GHz	6 GHz	4 GHz	6 GHz
Real Sample Rate	200 kS/s	300 kS/s	20 GS/1-Ch 10 GS/2-Ch 5 GS/4-Ch	20 GS/s All 4 channels	20 GS/s All 4 channels	20 GS/s All 4 channels	20 GS/s All 4 channels
Rise Time	<17.5 ps	17.5 ps	50 ps	62 ps	70 ps	70 ps	70 ps
Record length per channel	4k samples	4086 samples	4M/1-Ch 2M/2-Ch 1M/4-Ch or 200 us	2M samples or 100 us	2M samples or 100 us	262k samples	262k samples
Price	From $32,000	From $27,000	From $50,900	From $59,000	From $59,000	From $33,000	From $48,000

APPENDIX 4: SP16T SWITCH HOUSING PACKAGE DRAWINGS

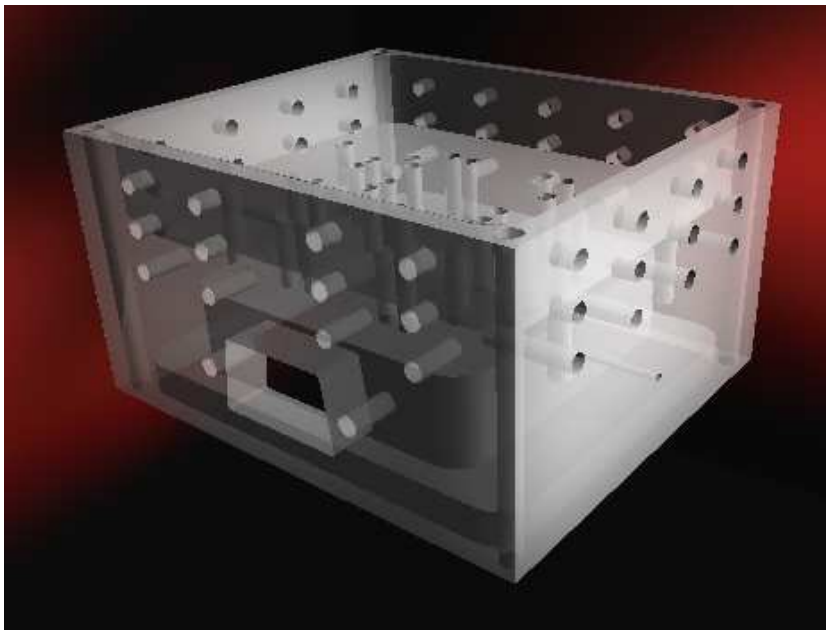

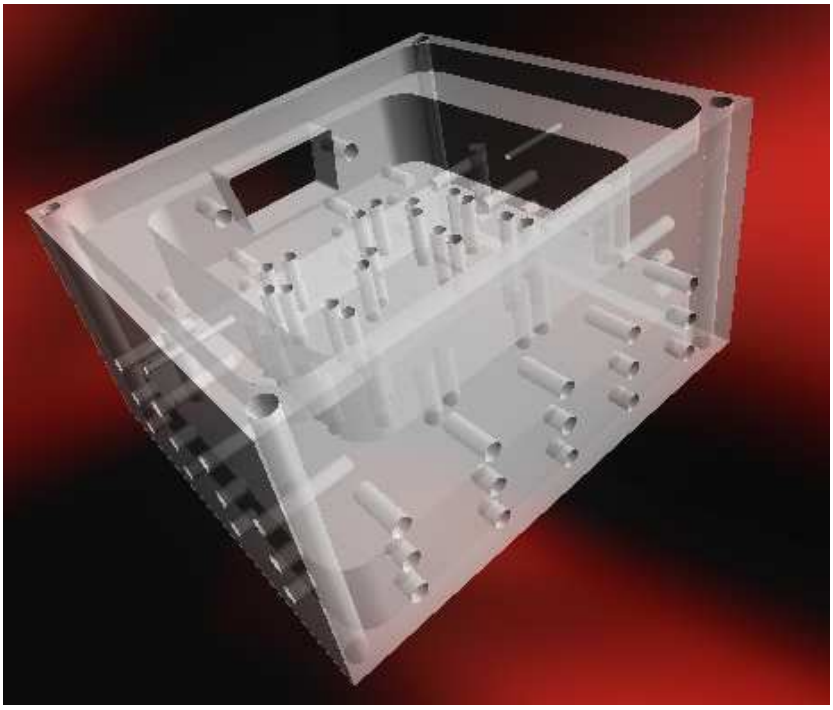

APPENDIX 5: MATLAB SCRIPTS

```
%%%%%%%%%%%% Oscilloscope_System_Automation.m %%%%%%%%%%
% Automation for Conceptual System
clear all;
RecordLength=500;
%pause(3);
% Creat a VISA-GPIB instrument object to virtual GPIB
% Creat a digital I/O parallel port
parport=digitalio('parallel','LPT1');
hwlines=addline(parport,0:3,'out');
putvalue(parport,0);
% Creat Oscilloscope VISA
g=visa('tek','GPIB8::1::INSTR');
set(g,'InputBufferSize',1000);
fopen(g);
% Oscilloscope Config
%     idn=query(g,'*IDN?');%
%     fprintf(g,'HORIZONAL:POSITION 19e-9');
%     fprintf(g,'HORIZONAL:RECORDLENGTH 1000');
%     fprintf(g,'HORIZONAL:SCALE 10e-9');
    fprintf(g,'CH1:SCALE 1.0e-1');
    fprintf(g,'CH2:SCALE 1.0e-1');
%     fprintf(g,'ACQuire:MODE AVERAGE');
    fprintf(g,'ACQUIRE:NUMAVG 30');
%     fprintf(g,'ACQUIRE:STOPAFTER:CONDITION AVGCOMP');
%     fprintf(g,'TRIGGER:SETLEVEL');
    fprintf(g,'TRIGGER:MODE NORMAL');
    fprintf(g,'TRIGGER:SOURCE EXTDIRECT');
for i=1:16
    i
```

```
   % 1 to 16 Switch Control
   data=dec2binvec(i-1,4);
   putvalue(parport,data);
   pause(0.01);
   fprintf(g,'ACQuire:MODE SAMPLE');
   fprintf(g,'ACQuire:MODE AVERAGE');
   pause(1.5);
   % while query(g,'BUSY?','%s','%e') end;
    fprintf(g,['EXPORT CH1,"C:\TDS8000\P' num2str(i) 'C1.txt"']);
   fprintf(g,['EXPORT CH2,"C:\TDS8000\P' num2str(i) 'C2.txt"']);
end
 pause(0.5); fclose(g); stop(parport);

%%%%%%%%%%%%%%%%%%%%%%%%%%%%%%%%%%%%%%%%
%              Binary to Decimal Conversion                    %
%%%%%%%%%%%%%%%%%%%%%%%%%%%%%%%%%%%%%%%%
for n=1:16
   datafile_C1=['P' num2str(n) 'C1.txt'];
   datafile_C2=['P' num2str(n) 'C2.txt'];
   fid_C1=fopen(datafile_C1);
   fid_C2=fopen(datafile_C2);
   C1=fscanf(fid_C1,'%g,',inf);
   C2=fscanf(fid_C2,'%g,',inf);
   RS_C1=reshape(C1,1,500);
   RS_C2=reshape(C2,1,500);
   I_data(n,:)=RS_C1(1,:);
   Q_data(n,:)=RS_C2(1,:);
   fclose(fid_C1);
   fclose(fid_C2);
```

```
end
I_file_raw=I_data';
% I_file_raw=I_file_raw(1:400,:);
Q_file_raw=Q_data';
% Q_file_raw=Q_file_raw(1:400,:);

% Rearrange of Data Sequence
tempI=I_file_raw;
tempQ=Q_file_raw;
I_file_raw(:,1:2)=tempI(:,[6 3]);
Q_file_raw(:,1:2)=tempQ(:,[6 3]);
I_file_raw(:,3:4)=tempI(:,[4 5]);
Q_file_raw(:,3:4)=tempQ(:,[4 5]);
I_file_raw(:,5:6)=tempI(:,[7 8]);
Q_file_raw(:,5:6)=tempQ(:,[7 8]);
I_file_raw(:,7:10)=tempI(:,[2 1 16 15]);
Q_file_raw(:,7:10)=tempQ(:,[2 1 16 15]);
I_file_raw(:,11:12)=tempI(:,[9 10]);
Q_file_raw(:,11:12)=tempQ(:,[9 10]);
I_file_raw(:,13:16)=tempI(:,[12 13 14 11]);
Q_file_raw(:,13:16)=tempQ(:,[12 13 14 11]);
 xx_raw=I_file_raw(1:400,:);
yy_raw=Q_file_raw(1:400,:);
z_raw=xx_raw+1j*yy_raw; % the complex received signal
%             % !!! Never Ever mess with 1j
```

APPENDIX 6: FPGA SCHEMATICS AND VHDL SOURCE CODE.

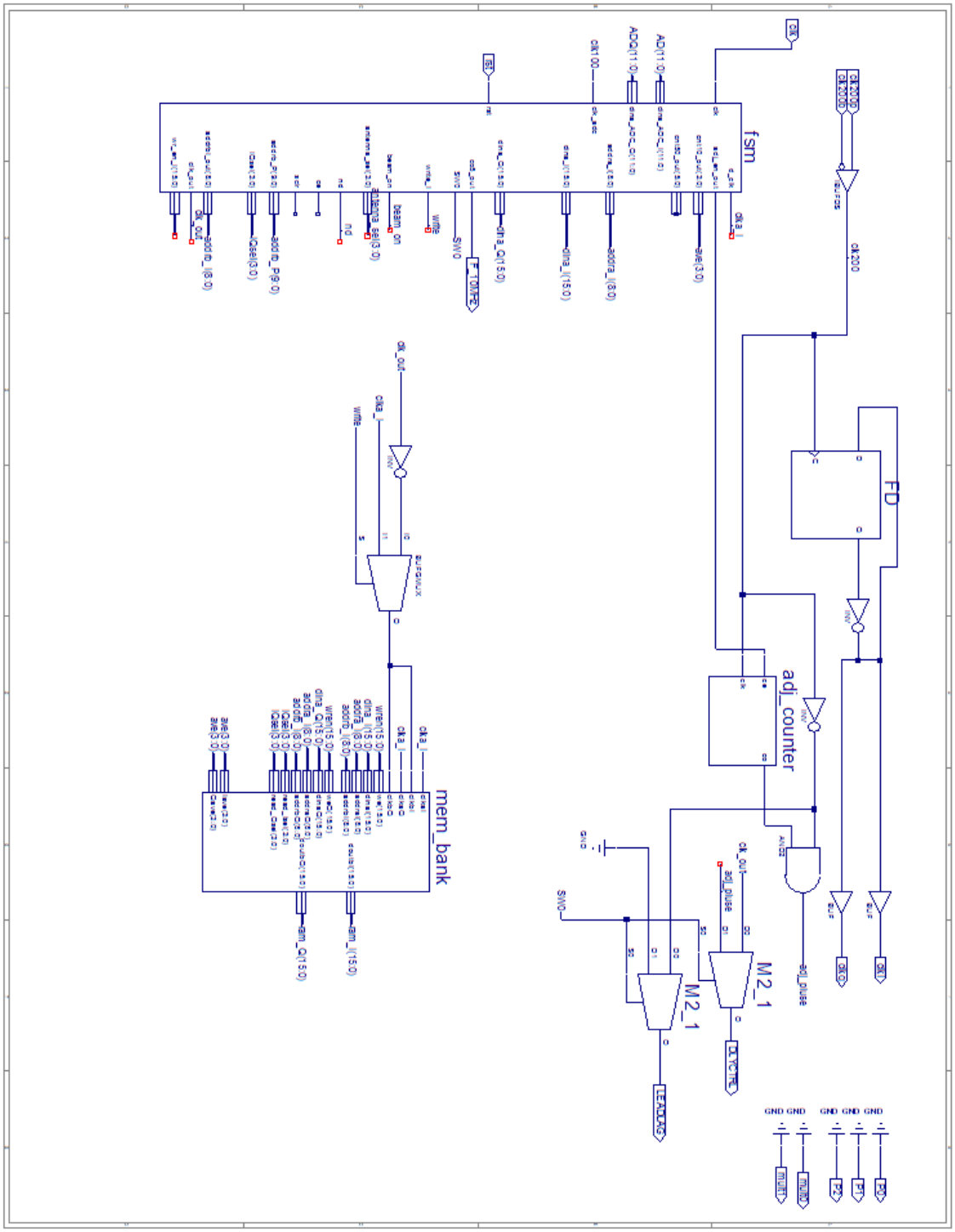

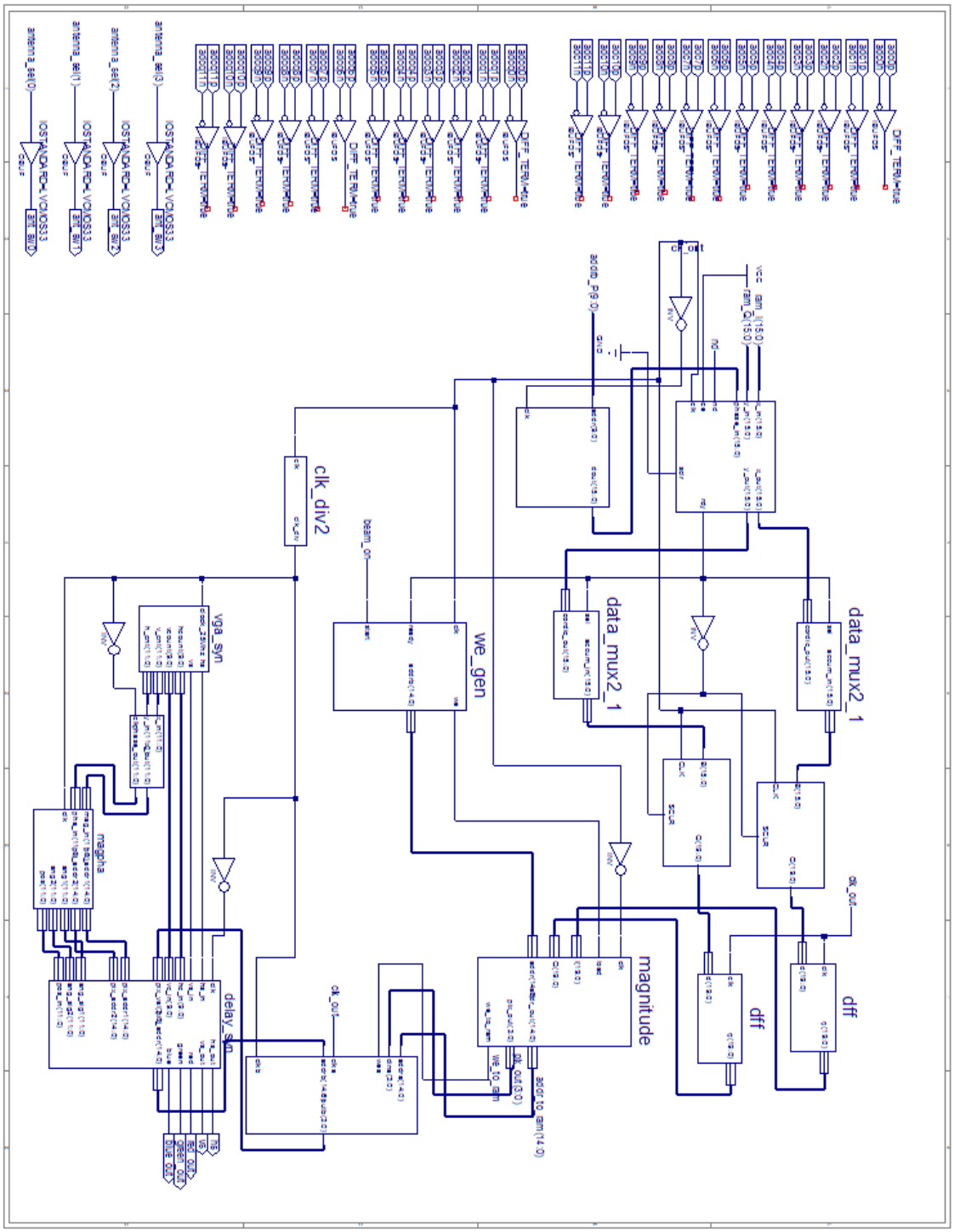
clk_div2
vga_syn
we_gen
data_mux2_1
data_mux2_1
magnitude
dff
dff
delay_syn
magpha
beam_on
clk_out
addr_to_ram(14:0)
we_to_ram
clk_out(0:0)
ram_clk(15:0)
addr_p(0)
GND
VCC
clk_out
antenna_sel(0)
antenna_sel(1)
antenna_sel(2)
antenna_sel(3)
IOSTANDARD=LVCMOS33
DIFF_TERM=true

```
----------------------------------------------------------------------------------
-- Company: University of Tennessee, Knoxville
-- Engineer: Yunqiang Yang
--
-- Create Date:    20:51:57 12/27/0
-- Design Name:
-- Module Name:    time_base - Behavioral
-- Project Name:
-- Target Device:
-- Tool versions:
-- Description:
--
-- Dependencies:
--
-- Revision:
-- Revision 0.01 - File Created
-- Additional Comments:
--
----------------------------------------------------------------------------------
library IEEE;
use IEEE.STD_LOGIC_1164.ALL;
use IEEE.STD_LOGIC_ARITH.ALL;
use IEEE.STD_LOGIC_UNSIGNED.ALL;

---- Uncomment the following library declaration if instantiating
---- any Xilinx primitives in this code.
--library UNISIM;
--use UNISIM.VComponents.all;

entity FSM is
    Port (  clk             :  in std_logic;
            clk_adc         :  in std_logic;
            dina_ADC_I      :  in std_logic_vector(11 downto 0);
            dina_ADC_Q      :  in std_logic_vector(11 downto 0);
            d_clk           :  out std_logic;
            SW0             :  out std_logic;
            adj_en_out      :  out std_logic;
            cnt10_out       :  out std_logic_vector(3 downto 0);
            cnt50_out       :  out std_logic_vector(5 downto 0);
            addra_I         :  out std_logic_vector(8 downto 0);
            addrbI_out      :  out std_logic_vector(8 downto 0);
            wr_en_I         :  out std_logic_vector(15 downto 0);
            dina_I          :  out std_logic_vector(15 downto 0);
            --addra_Q          :  out std_logic_vector(8 downto 0);
            --addrbQ_out       :  out std_logic_vector(8 downto 0);
            --wr_en_Q          :  out std_logic;
            dina_Q          :  out std_logic_vector(15 downto 0);
            co5_out         :  out std_logic;
            clk_out         :  out std_logic;

```

```
50
51              ---- Swith Signal
52              rst                 :  in    std_logic;
53              write_I             :  out   std_logic;
54              antenna_sel         :  out   std_logic_vector(3 downto 0);
55              beam_on             :  out   std_logic;
56
57              ---- Beamformer Signal
58              --addrb_Ibf :  out   std_logic_vector(8 downto 0);
59              --I_sel     :  out   std_logic_vector(3 downto 0);
60              --addrb_Qbf :  out   std_logic_vector(8 downto 0);
61              addrb_P  :  out   std_logic_vector(9 downto 0);
62              nd       :  out   std_logic;
63              ce       :  out   std_logic;
64              sclr     :  out   std_logic;
65
66              ---- Supp Func Signal
67              IQsel    :  out   std_logic_vector(3 downto 0):="0000"
68
69            );
70  end FSM;
71
72  architecture Behavioral of FSM is
73
74        signal co5:std_logic;
75        signal co10:std_logic;
76        signal co3:std_logic;
77        signal co50:std_logic;
78        signal trig_10mhz:std_logic;
79        signal co50_sig:std_logic;
80        signal SW0_sig: std_logic;
81        signal co64_I:std_logic;
82        --signal co64_Q:std_logic;
83        signal adj_en_cnt1: std_logic;
84        signal adj_en_cnt1_cnt1: std_logic;
85        signal adj_en:std_logic;
86        signal cnt5_q :  std_logic_vector(2 downto 0);
87        signal cnt10_q :  std_logic_vector(3 downto 0);
88        signal cnt3_q :  std_logic_vector(1 downto 0);
89        signal cnt50_q :  std_logic_vector(5 downto 0);
90        signal cnt64_q_I :  std_logic_vector(5 downto 0);
91        --signal cnt64_q_Q :  std_logic_vector(5 downto 0);
92        signal addra_I_sig: std_logic_vector(9 downto 0);
93        signal addrb_I_sig: std_logic_vector(9 downto 0);
94        signal addrab_base: std_logic_vector(9 downto 0);
95        signal wr_en_I_sig:std_logic;
96        signal wren_sig:std_logic_vector(15 downto 0):="0000000000000001";
97        signal wren:std_logic_vector(15 downto 0):="0000000000000001";
98
99        --signal addra_Q_sig: std_logic_vector(9 downto 0);
100       --signal addrb_Q_sig: std_logic_vector(9 downto 0);
```

```
101       --signal wr_en_Q_sig:std_logic;
102
103       signal d_clk_I:std_logic;
104
105
106
107     ---- Switch Signal ----
108     signal write_I_sig      :  std_logic:= '0';
109     signal antenna_sel_sig  :  std_logic_vector(7 downto 0):=(others=>'0');
110     signal frame_cnt        :  std_logic_vector(15 downto 0):=(others=>'0');
111     signal state_sw         :  std_logic_vector(3 downto 0):="0000";
112
113     ---- Beam Former Signal ----
114     signal addrb_BF_sig : std_logic_vector(8 downto 0);
115     signal addrb_P_sig : std_logic_vector(9 downto 0);
116     signal I_selbf_sig    : std_logic_vector(4 downto 0);
117     signal nd_sig     :  std_logic:='0';
118     signal ce_sig     :  std_logic:='0';
119     signal sclr_sig   :  std_logic:='1';
120     signal cnt_16     :  std_logic_vector(4 downto 0);   -- every addrss 16 times
121     signal cnt_512    :  std_logic_vector(10 downto 0);  -- every beam 512 times
122     signal cnt_32     :  std_logic_vector(5 downto 0);   -- 32 beams
123     signal cnt_10     :  std_logic_vector(5 downto 0);   -- 10 points
124     signal state_bf       : std_logic_vector(3 downto 0):=(others => '0');
125
126     ---- Supp Funcs Signal ----
127     signal addr_flag   : std_logic_vector(1 downto 0):="00";
128
129 begin
130       process(clk)
131       begin
132          if clk'event and clk='1' then
133             if cnt5_q<=3 then
134                cnt5_q<=cnt5_q+1;
135                co5<='0';
136             else
137                cnt5_q<="000";co5<='1';
138             end if;
139          end if;
140       end process;
141
142       process(clk)          ---- key lines to adjust pulse delay
143       begin
144          if clk'event and clk='1' then
145             if cnt5_q=2 then
146                trig_10mhz<='1';
147             else
148                trig_10mhz<='0';
149             end if;
150          end if;
```

```
151         end process;
152
153         process(co5)
154         begin
155
156            if co5'event and co5='1' then
157               if cnt3_q<=2 then
158                  cnt3_q<=cnt3_q+1;
159                  co3<='0';
160               else
161                  cnt3_q<="00";co3<='1';
162               end if;
163            end if;
164         end process;
165
166         process(co5)
167         begin
168               if co5'event and co5='1' then
169               if cnt3_q=2 then
170                  adj_en<='1';
171                  --co16_out<='1';
172               else
173                  adj_en<='0';
174                  --co16_out<='0';
175               end if;
176               end if;
177         end process;
178
179         process(co3)        ---- key lines to avoid last accumulation error  777, run s
180         begin
181
182            if co3'event and co3='1' then
183               if cnt10_q<=7 then
184                  cnt10_q<=cnt10_q+1;
185                  co10<='0';
186               else
187                  cnt10_q<="0000";co10<='1';
188               end if;
189            end if;
190         end process;
191
192         process(co3)      ---- key lines to avoid last accumulation error  777
193         begin
194
195            if co3'event and co3='1' then
196               if cnt10_q=7 then
197                  adj_en_cnt1<='1';
198               else
199                  adj_en_cnt1<='0';
200               end if;
```

```
200             end if;
201          end if;
202       end process;
203
204 ---- Add synchronization switch signal here----------
205       process(co10)
206       begin
207
208             if co10'event and co10='1' then
209                   if cnt50_q<=49 then
210                      cnt50_q<=cnt50_q+1;
211                      --co50<='0';
212                      --SW0_sig <= '1';
213                   else
214                      cnt50_q<="000000"; --co50<='1'; SW0_sig <= '0';
215                   end if;
216             end if;
217       end process;
218
219       process(clk)--cnt50_q)          ------- key lines to solve shifting
220       begin
221             if clk'event and clk='1' then
222             if cnt50_q<=50 and cnt50_q>=3 then
223                co50<='0'; SW0 <= '1';
224             elsif cnt50_q<=2 and cnt50_q>=1 then
225                co50<='1'; SW0 <= '1';
226             else
227                co50<='1'; SW0 <= '0';
228             end if;
229             end if;
230       end process;
231
232 ------ bk -----
233 ------------------------------------------------
234 -- Generate controlling signals for channal I:
235 ------------------------------------------------
236       process(d_clk_I)
237       begin
238          if co3='1' then
239             cnt64_q_I<="000000";
240          elsif d_clk_I'event and d_clk_I='1'then
241             if cnt64_q_I<=28 then
242                cnt64_q_I<=cnt64_q_I+1;
243                co64_I<='0';
244             --else
245             -- cnt64_q_I<="000000";co64_I<='1';
246             end if;
247          |     end if;
248       end process;
249
250       process(d_clk_I)
```

```
251       begin
252             if d_clk_I'event and d_clk_I='0' then
253                if cnt64_q_I <= 2 then
254                   addrab_base <= ('0'&(cnt50_q-1)&"000") + ("000"&(cnt50_q-1)&'0');
255                end if;
256             end if;
257       end process;
258
259 -- Address for reading
260  process (d_clk_I)
261       begin
262          if co50 = '0' then
263             if d_clk_I'event and d_clk_I='1' then
264
265                if ((cnt64_q_I>=13) and (cnt64_q_I<=21)) and cnt10_q<=7 then  -- 12 20
266                   addrb_I_sig <= addrb_I_sig + 1;
267                else
268                   --addrb_I_sig <= (cnt50_q-1) * "1010";
269                   addrb_I_sig <= addrab_base;
270                end if;
271
272             end if;
273          else
274                   addrb_I_sig <= "0000000000";
275          end if;
276   end process;
277
278 -- Generate port A write enable signal
279       process(d_clk_I)
280       begin
281          if co50 = '0' then
282             if d_clk_I'event and d_clk_I='0' then
283                if ((cnt64_q_I>=13) and (cnt64_q_I<=22)) and cnt10_q<=7 then  -- 12 21
284                   wr_en_I_sig <='1';
285                else
286                   wr_en_I_sig <= '0';
287                end if;
288             end if;
289          else
290             wr_en_I_sig <= '0';
291          end if;
292       end process;
293
294 --Generate Address for Writing in PortA
295       process(d_clk_I)
296       begin
297          if co50 = '0' then
298             if d_clk_I'event and d_clk_I='0' then
299                if wr_en_I_sig = '1' then
300                   addra_I_sig <= addra_I_sig + 1;
```

```
301                 else
302                    --addra_I_sig <= (cnt50_q-1) * "1010";
303                    addra_I_sig <= addrab_base;
304                 end if;
305              end if;
306           else
307
308              addra_I_sig <= "0000000000";
309
310           end if;
311
312        end process;
313
314  ----------------------------
315          co5_out<=trig_10mhz;
316          --SW0 <= SW0_sig;
317          cnt10_out<=cnt10_q;
318          cnt50_out<=cnt50_q;
319          adj_en_out<=adj_en AND adj_en_cnt1;
320          addra_I <= addra_I_sig(8 downto 0);
321  --       wr_en_I(0) <= wr_en_I_sig and write_I_sig and wren(0); -- AND wr_en_sig;
322  --       wr_en_I(1) <= wr_en_I_sig and write_I_sig and wren(1);
323  --       wr_en_I(2) <= wr_en_I_sig and write_I_sig and wren(2);
324  --       wr_en_I(3) <= wr_en_I_sig and write_I_sig and wren(3);
325  --       wr_en_I(4) <= wr_en_I_sig and write_I_sig and wren(4);
326  --       wr_en_I(5) <= wr_en_I_sig and write_I_sig and wren(5);
327  --       wr_en_I(6) <= wr_en_I_sig and write_I_sig and wren(6);
328  --       wr_en_I(7) <= wr_en_I_sig and write_I_sig and wren(7);
329  --       wr_en_I(8) <= wr_en_I_sig and write_I_sig and wren(8);
330  --       wr_en_I(9) <= wr_en_I_sig and write_I_sig and wren(9);
331  --       wr_en_I(10) <= wr_en_I_sig and write_I_sig and wren(10);
332  --       wr_en_I(11) <= wr_en_I_sig and write_I_sig and wren(11);
333  --       wr_en_I(12) <= wr_en_I_sig and write_I_sig and wren(12);
334  --       wr_en_I(13) <= wr_en_I_sig and write_I_sig and wren(13);
335  --       wr_en_I(14) <= wr_en_I_sig and write_I_sig and wren(14);
336  --       wr_en_I(15) <= wr_en_I_sig and write_I_sig and wren(15);
337
338          wr_en_I <= wren when (wr_en_I_sig='1' and write_I_sig='1') else (others=>'0');
339
340  --------------------------------
341  -- Data signal from ADC
342
343        process(d_clk_I)
344        begin
345           if d_clk_I'event and d_clk_I='0' then
346              if dina_ADC_I(11) = '0' then
347                  dina_I <="0000" & dina_ADC_I;
348              else
349                  dina_I <="1111" & dina_ADC_I;
350              end if;
```

```
351          end if;
352       end process;
353
354
355       process(d_clk_I)
356       begin
357          if d_clk_I'event and d_clk_I='0' then
358             if dina_ADC_Q(11) = '0' then
359               dina_Q <="0000" & dina_ADC_Q;
360             else
361                dina_Q <="1111" & dina_ADC_Q;
362             end if;
363          end if;
364       end process;
365
366
367 --- Switch Design -----------
368
369
370    process(co50)
371    begin
372
373       if co50'event and co50='1'then
374
375          if rst = '1' then
376             write_I_sig <= '0';  -- can't write sampling signals to BRAM_I
377             antenna_sel_sig <= (others=>'0');
378             frame_cnt <= (others=>'0');
379             state_sw <= "0000";
380
381          else
382             case state_sw is
383
384                when "0000" =>
385                      state_sw <= "0001";
386                      antenna_sel_sig <= (others=>'0');
387                      antenna_sel <= (others=>'0');
388                      write_I_sig <= '1';
389                      wren_sig <= "0000000000000001";
390                      wren <= "0000000000000001";
391
392                when "0001" =>
393
394                      if antenna_sel_sig <= 15 then
395                            antenna_sel    <= antenna_sel_sig(3 downto 0);
396                            antenna_sel_sig <= antenna_sel_sig + 1;
397                            write_I_sig <= '1';
398                            wren <= wren_sig;
399                            wren_sig <= wren_sig + wren_sig;
400                      else
```

```
401                             write_I_sig <= '0';
402                             state_sw <= "0101";
403                             antenna_sel_sig <= (others=>'0');
404                             antenna_sel <= (others=>'0');
405
406                         end if;
407
408                   when "0101" =>
409                         if frame_cnt <= 300 then
410                            frame_cnt <= frame_cnt+1;
411                         else
412                            state_sw <= "0000";
413                            frame_cnt <= (others=>'0');
414                         end if;
415
416                   when others =>
417                         state_sw <= "0000";
418                   end case;
419
420               end if;
421            end if;
422       end process;
423
424   ----- Beamformer Process -----
425
426   addrb_P <= addrb_P_sig(9 downto 0);
427   nd    <= nd_sig;
428   ce    <= ce_sig;
429   sclr  <= sclr_sig;
430
431   process(clk) --,write_I_sig)
432   begin
433   if clk'event and clk='1' then
434     if write_I_sig='1' then
435      state_bf<="0000";
436      addrb_P_sig <= (others=>'0');
437      addrb_BF_sig <= (others=>'0');
438      I_selbf_sig <= (others=>'0');
439      beam_on <= '0';
440      nd_sig    <= '0';
441      ce_sig    <= '0';
442      sclr_sig  <= '1';
443      cnt_16 <= (others=>'0');
444      cnt_512<= (others=>'0');
445      cnt_32 <= (others=>'0');
446      cnt_10 <= (others=>'0');
447
448   --  elsif clk'event and clk = '1' then
449    else
450         case state_bf is
```

```
451           when "0000" =>   --state 0
452              if cnt_32<=60 then
453                 cnt_32 <= cnt_32 + 1;
454 --              ce_sig <= '1';  -- cordic enable
455 --              sclr_sig<= '0';    -- deassert the cordic
456 --              nd_sig <='1';  -- new data is available
457                 beam_on <= '1';
458                 state_bf <= "1000";
459                 addrb_P_sig <=cnt_32 & "0000";
460                 addrb_BF_sig <= (others=>'0');
461              else
462                 state_bf <= "1111";
463                 nd_sig <= '0';
464                 beam_on <= '0';
465                 --cnt_32<= (others=>'0');    ----???????
466              end if;
467
468           when "1000" =>   -- state 8
469                 if cnt_10 <= 9 then
470                       ce_sig <= '1';  -- cordic enable
471                       sclr_sig<= '0';    -- deassert the cordic
472                       nd_sig <='1';  -- new data is available
473                       state_bf <= "0001";
474                       cnt_10 <= cnt_10 + 1;
475                 else
476                       state_bf <= "0000";
477                       cnt_10 <= (others=>'0');
478                 end if;
479
480           when "0001" =>  -- state 1
481                 if cnt_16 <= 14 then
482                       I_selbf_sig <= I_selbf_sig + 1;
483                       --Q_sel_sig <= Q_sel_sig + 1;
484                       addrb_P_sig <= addrb_P_sig + 1;
485                       cnt_16 <= cnt_16 + 1;
486                       state_bf <= "0001";
487                 else
488                       I_selbf_sig <= (others=>'0');
489                       --Q_sel_sig <= (others=>'0');
490                       addrb_BF_sig <= addrb_BF_sig + 10;
491                       addrb_P_sig <=(cnt_32-1) & "0000";
492                       cnt_16 <= (others=>'0');
493
494                       state_bf <= "0010";
495                       nd_sig <= '0';
496                 end if;
497
498           when "0010" =>    -- state 2
499
500                 if cnt_512 <= 46 then      --46
```

```
501                     cnt_512 <= cnt_512 + 1;
502                     state_bf <= "0001";
503                     nd_sig <= '1';
504                 else
505                     cnt_512 <= (others=>'0');
506                     addrb_BF_sig <= "000" & cnt_10;
507                     state_bf<="1000";
508                     nd_sig <= '0';
509                  end if;
510           when "1111" =>
511                 null;
512
513           when others =>
514                 state_bf <= "1111";
515
516           end case;
517     end if;
518      end if;
519   end process;
520
521   process(clk)
522   begin
523      if clk'event and clk='1' then
524         write_I <= write_I_sig;
525      end if;
526   end process;
527
528
529   ---- Supporting Funcs ----
530
531   IQsel <= I_selbf_sig(3 downto 0);
532   addrbI_out <= addrb_I_sig(8 downto 0) when(write_I_sig = '1') else addrb_BF_sig;
533   d_clk_I <= clk_adc AND write_I_sig;
534   d_clk <= not clk_adc;
535   clk_out <= clk;
```

VITA

Yunqiang Yang was born in Fujian, China in 1978. He grew up in a small, quiet town in Southern China, with his parents and little brother. In 1997, Yang graduated from high school and attended Zhejiang University at Hangzhou, China. Four years later, he happily graduated from Zhejiang University, receiving the B.S. degree in Information Science and Electronic Engineering (Electrical Engineering). He started his graduate study, as a M.S. student, at the University of Tennessee, Knoxville in the Fall of 2001. He was a graduate research assistant with Plasma Sciences Laboratory, the Department of Electrical Engineering and Computer Science. In 2003, he received the M.S. degree in EE, and joined the Antennas and Microwave Systems Group to continue his Ph.D. study. His research was focused on Ultra-Wideband system development. In July 2007, Yang joined Agilent Technologies, Inc. as an R&D staff.